2015

A Search for New Physics with a Three Photon Final State Using the CMS Detector

Brendan F. Diamond

FLORIDA STATE UNIVERSITY

COLLEGE OF ARTS AND SCIENCES

A SEARCH FOR NEW PHYSICS WITH A THREE PHOTON FINAL STATE USING THE CMS DETECTOR

By

BRENDAN F. DIAMOND

A Dissertation submitted to the
Department of Physics
in partial fulfillment of the
requirements for the degree of
Doctor of Philosophy

2015

Brendan F. Diamond defended this dissertation on July 15, 2015.
The members of the supervisory committee were:

Todd Adams

Professor Directing Dissertation

Michael Bishop

University Representative

David Collins

Committee Member

Takemichi Okui

Committee Member

Harrison Prosper

Committee Member

The Graduate School has verified and approved the above-named committee members, and certifies that the dissertation has been approved in accordance with university requirements.

Dedicated to my parents, Monica and Lorenzo Diamond.

ACKNOWLEDGMENTS

I must thank foremost my wife, Tiara, who has been my strength through every challenge in life. My son, Éamon, who always reminds me of what is most important in life. My advisor, Dr. Todd Adams, who has been my model of a good teacher for many years. His positive outlook and problem solving abilities have saved me many times throughout my graduate career. I must also thank both my parents and my in-laws, who have supported me through this journey, and all my siblings and extended family who have kept me feeling connected despite thousands of miles of distance.

I am truly grateful for my professors and staff in the Physics Department of CSU, Chico who were the foundation of my physics training and inspiration. I will be eternally grateful to Kris Koenig and Anita Ingrao who magnified and crystalized my passion for science through years of watching the stars together at the Chico Observatory.

I am very grateful for the assistance of Dr. Prerit Jaiswal for making the Madgraph model files from FeynRules, and for Dr. Takemichi Okui for invaluable discussion on the theory. Thanks to my fellow graduate students in HEP and physics, especially Venkatesh Veeraraghavan, who were excellent colleagues and friends. I have also been grateful for the experienced and friendly staff of the Physics Department at FSU who make everything run smoother allowing research to flourish.

Thanks also to my colleagues at CERN and the CMS experiment who provided the opportunity for so many students, including me, to examine the deepest questions humanity has ever asked. Thanks also to financial support from FSU, the US Department of Energy, and Tallahassee Community College.

TABLE OF CONTENTS

LIST OF TABLES

LIST OF FIGURES

LIST OF SYMBOLS

b	b quark
BR	branching ratio
e	electron
E_{SC}	total energy of the super cluster
E_T	transverse energy
$\not{E}_T$	missing transverse energy
$E_{3\times3}$	energy in the nine crystals encompassing and including the seed crystal
$E_{5\times5}$	energy in the 25 crystals encompassing and including the seed crystal
EA	effective area
f_{rev}	revolution frequency
$f_{\tilde{\pi}}$	hyperpion decay constant
F	geometric luminosity reduction factor
g	gluon
H	Higgs boson
H/E	calorimetric energy deposition ratio
L	luminosity
$\mathcal{L}$	integrated luminosity
m, M	mass
N_b	number of particles per bunch
n_b	number of bunches per beam
$N_{pp\to X}$	number of collisions
p	proton
p	momentum
$\vec{p}_i$	momentum of the ith particle in an event
P_T^γ	transverse momentum of the candidate
R	radius
R_9	ECAL energy distribution
$\sqrt{s}$	center-of-mass energy
$W^\pm$	W boson
X_0	radiation lengths
Z	Z boson
β^*	beta function at the collision point
ϵ_n	normalized transverse beam emittance
ε	acceptance efficiency

ϕ	azimuthal angle, measured in the $x - y$ plane
γ_r	relativistic gamma factor
$\gamma\gamma$	diphoton
η	pseudorapidity
$\tilde{\pi}^{\pm}$	hyperpion particle
$\tilde{\pi}_D$	hyperpion weak doublet state
$\tilde{\pi}_T$	hyperpion weak triplet state
$\tilde{\pi}_S$	hyperpion singlet state
$\tilde{\rho}^{\pm}$	hyperrho particle
σ^*	transverse RMS beam size
θ_c	crossing angle at the interaction point
σ	cross section
σ	XXX (in reference to uncertainty)
$\sigma_{i\eta i\eta}$	energy weighted η-width
$\sigma_{pp\to X}$	cross section
σ_z	RMS bunch length
θ	polar angle, measured from the z axis along the counterclockwise-beam direction
ω_0	optimizable constant for CMS

LIST OF ABBREVIATIONS

ALICE	A Large Ion Collider Experiment
AOD	Analysis Object Data
APD	avalanche photodiodes
ATLAS	A Toroidal LHC Apparatus
BSM	beyond the standard model theory of physics
CMS	Compact Muon Solenoid
CMSSW	CMS Software
DAQ	data acquisition system
di-CHAMP	pair produced collider stable charged massive particles
ECAL	electromagnetic calorimeter
FED	Front End Electronics
Gsf	Gaussian-sum-filter
HCAL	hadron calorimeter
HLT	High-Level Trigger
IP	interaction point
JSON	JavaScript Object Notation
LEP	Large Electron-Positron Collider
LHC	Large Hadron Collider
L1	Level-1 trigger
MC	Monte Carlo simulation
PF	Particle Flow
PIXEL	CMS pixel detector
POG	Physics Object Groups
PS	Proton Synchrotron
PSB	Proton Synchrotron booster
P5	the CMS Experiment site
QCD	quantum chromodynamics
QED	quantum electrodynamics
RMS	root mean square
SM	Standard Model
SPS	Super Proton Synchrotron
TEC±	CMS tracker endcaps
TIB	CMS tracker inner barrel
TID	CMS tracker inner disks
TOB	CMS tracker outer barrel
VPT	vacuum phototriodes

ABSTRACT

A search for new physics with a three photon final state has been performed using data from the Compact Muon Solenoid detector at the Large Hadron Collider. The integrated luminosity was 12.3 fb^{-1} recorded in 2012 at center-of-mass energy of 8 TeV. No significant narrow resonance in the diphoton spectrum is observed in the mass range of $220 - 600$ GeV. The 95% confidence level limits on the cross section times branching ratio are presented.

CHAPTER 1

INTRODUCTION

Data from the 2012 run of the Large Hadron Collider (LHC) have been used to search for a new, narrow resonance in the diphoton mass spectrum from events with at least three photons. A motivating theory for the analysis, called "vectorlike confinement", introduces new fermions interacting via a new gauge force that produces a spectrum of new particles detectable at the energy scale of the LHC [1]. The model studied in this analysis produces a final state of three photons and a W boson through a decay chain starting with a new $M = 1$ TeV particle, the hyperrho ($\tilde{\rho}$). Figure 1.1 shows the relevant Feynman diagram [1]. Details of the model are discussed in Chapter 3.

1.1 The standard model

Our current theory of fundamental particle interactions, known as the standard model (SM), describes mathematically how three of the four known fundamental forces can produce almost all experimental results in particle physics. The familiar electromagnetic force has been integrated into the SM with the strong and weak nuclear forces, responsible for binding nucleons together and for nuclear decay, respectively. The fourth fundamental force, gravity, has yet to be included in the SM. The small energies of the colliding particles compared to the Planck mass and the large impact parameter compared to the Planck length make the omission of gravity negligible in comparison to the three dominant forces at the LHC.

The mathematical framework of the SM is quantum field theory (QFT), that has been in development since Dirac in the 1920's leading to the construction of quantum electrodynamics (QED) [2, 3]. The roots of the modern SM began with Glashow, Salam, and Weinberg, who are credited with modeling the unification of electromagnetic and weak forces at the 100 GeV energy scale in the 1960's [4, 5, 6]. Zweig and Gell-Mann independently developed models of quarks in 1964, which inspired the basic components of today's SM [7, 8, 9]. Gell-Mann coined the term

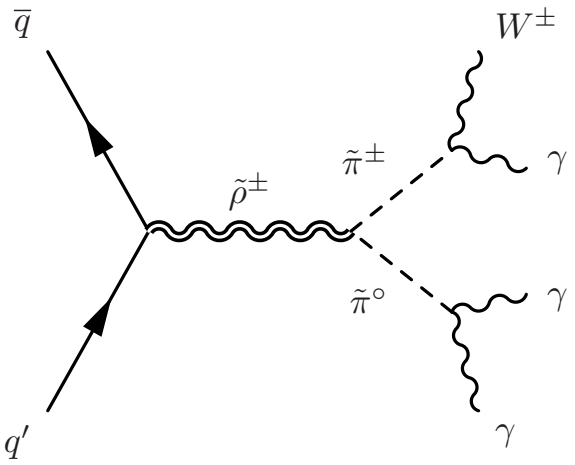

Figure 1.1: The Feynman diagram for the three photon final state process. The hypothesized process under investigation consists of a quark and antiquark annihilation that creates a new resonant particle, the charged hyperrho ($\tilde{\rho}^{\pm}$). The $\tilde{\rho}^{\pm}$ subsequently decays to two hyperpions ($\tilde{\pi}^{0}$ and $\tilde{\pi}^{\pm}$). The $\tilde{\pi}$ decay to a final state of three photons and a $W^{\pm}$. Details of the model are discussed in Ch. 3.

quarks, partly inspired by James Joyce. Accelerator experiments in the 1970's had confirmed the existence of the proton's constituents.

The SM is a Lagrangian that describes the SU(3) (strong) and SU(2)×U(1) (electroweak) interactions of fundamental particles. While the standard model is well documented in standard graduate physics textbooks for quick reference the basics are presented [10, 11, 12].

The particle content of the SM may be divided according to the spin quantum number into fermions (spin $\frac{1}{2}$), bosons (spin 1), and the Higgs boson (spin 0). The fermions consist of the quarks (up, down, charm, strange, top, bottom) and leptons (electron, muon, tau, electron neutrino, muon neutrino, tau neutrino). The fermions, gauge bosons (gluon, photon, Z boson, and W boson), Higgs boson, and associated antiparticles constitute the standard model particle content. The particle properties can be seen in Fig. 1.2.

In 2012, the CMS (Compact Muon Solenoid) Collaboration published the discovery of a new particle using multiple decay modes. The particle has a mass of 125 GeV and is consistent with the Higgs boson [13].

Despite the phenomenal success of the SM, there are many reasons why it is viewed as incomplete. One of the problems with the Standard Model, the "hierarchy problem", concerns the discrepancy in energy regimes where the electroweak and quantum gravitational interactions dom-

inate. This can also be restated as a problem arising in the quantum corrections to the Higgs mass parameter requiring either a surprisingly high mass Higgs boson or delicate cancellations of quantum corrections. Another problem is that the SM requires 19 free parameters (e.g. particle masses, couplings, etc.) to describe the observed universe. Also, the SM does not include gravitational interactions or a mechanism to explain the imbalance in the number of particles and antiparticles seen in nature. The standard model would require an extension to allow for the experimental evidence of neutrino masses. It also does not explain the nature of dark matter or inflation in the early Universe. Finally, the values characterizing the strength of fundamental interactions, called "gauge couplings", do not unify at any energy scale in the SM, whereas in many extensions to the SM (such as supersymmetry (SUSY)) these values converge to a single unifying value [14].

None of the concerns with the SM undermine the utility or precision of the SM, however when viewed all together, they suggest an incomplete understanding of the fundamental structure of the Universe. Hence it is necessary to continue exploring alternative hypotheses in theoretical high energy physics and investigate data thoroughly in experimental particle physics.

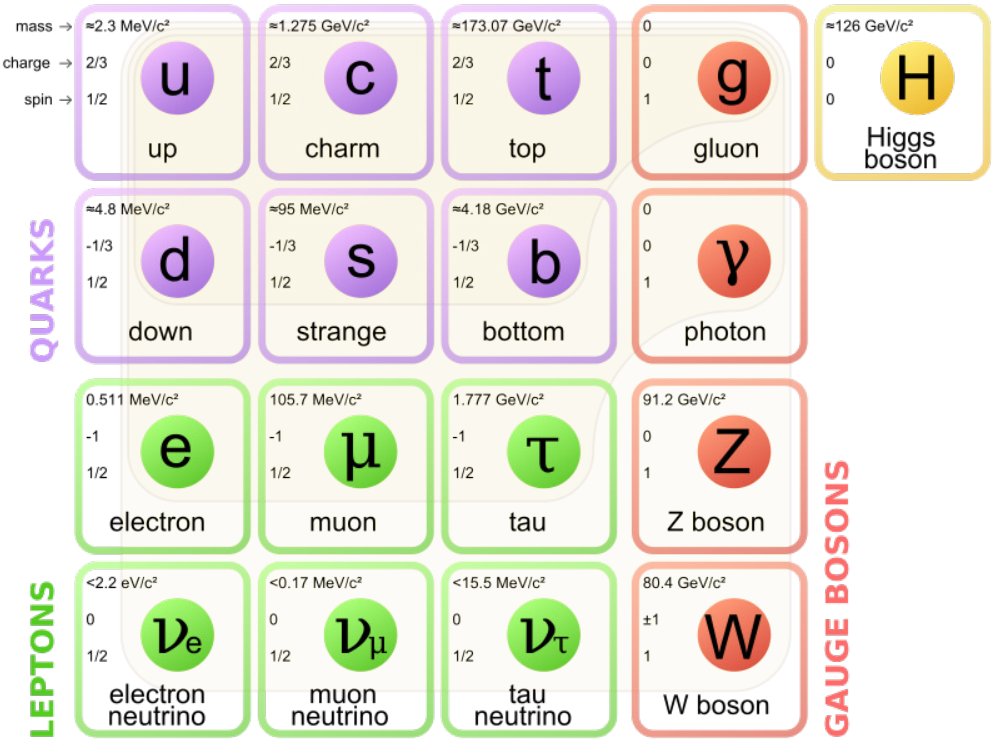

Figure 1.2: A table of the standard model particles [15].

1.1.1 Related searches

The CMS Collaboration has performed numerous searches for a narrow resonance in diphotons ($\gamma\gamma$) as part of the search (and measurement) of the Higgs boson [13, 16, 17, 18, 19]. These searches used a technique similar to that used here: fitting a continuous, smooth background plus narrow signal to the diphoton invariant mass distribution M($\gamma\gamma$). However, the Higgs searches were generally limited to M($\gamma\gamma$) $< 200\,\text{GeV}$ because the $H \to \gamma\gamma$ branching fraction drops to less than 0.001 above 200 GeV [20]. Above 135 GeV, the $H \to W^+W^-$ decay channel becomes dominant and searches use the WW and ZZ decay modes [21]. Because the $\gamma\gamma$ channel was considered one of the golden channels for Higgs discovery, photon identification and energy resolution were key considerations in the design of the CMS experiment [22]. Similar analyses have been performed by the ATLAS Collaboration [19, 23].

CMS has used diphoton events to search for other new physics. The M($\gamma\gamma$) $\approx 125\,\text{GeV}$ region was used in conjunction with two b-jets to search for predicted SUSY particle production such as the top squark and higgsino [24]. The search for extra dimensions used the diphoton mass spectrum in varying regions above 60 GeV [25, 26]. Events with diphotons and missing transverse energy were used in a search for supersymmetry [27]. In addition, the two photon sample has been used to measure the diphoton production cross section [28].

Because the theoretical basis of vectorlike confinement (see Section 3.1) creates a range of testable models, other searches can have an impact on the theory. One possible outcome creating two charged massive particles, known as the di-CHAMP model, has two long-lived $\tilde{\pi}^{\pm}$ per event. This model starts with pair production of a hypothesized charged hyperrho ($\tilde{\rho}^{\pm}$) followed by the decay $\tilde{\rho}^{\pm} \to \tilde{\pi}^{-}\tilde{\pi}^{+}$. The $\tilde{\pi}^{\pm}$ is sufficiently long-lived to traverse the detector prior to decaying, leaving a distinctive signature of large dE/dx and long time-of-flight to the muon system. The CMS collaboration found no significant excess compared to the standard model expectation [29, 30]. Limits were set on the existence of a massive, long-lived, charged particle depending on the magnitude of the charge [29, 30, 31]. While resonant searches for Z', W', and g' have similarities to this analysis, the vectorlike confinement model differs since the hyperrho requires an intermediary beyond the SM particle before decay to SM particles. Past resonant searches typically allow for direct decay to SM particles [32, 33].

CHAPTER 2

EXPERIMENTAL APPARATUS

2.1 The Large Hadron Collider

The LHC is located northwest of Geneva, Switzerland, occupying the tunnel created for the Large Electron-Positron Collider (LEP) below parts of France and Switzerland. The 27 km tunnel varies in depth from 45 m to 170 m with a diameter of 3.7 m. The Large Hadron Collider consists of two counter-rotating particle beams to provide collision data for proton-proton (p-p), proton-lead, and lead-lead interactions. The work presented here will focus on the p-p process. The dimensions of the tunnel and the strength of the superconducting magnets strongly influenced the proton-proton design center-of-mass energy $\sqrt{s} = 14\,\text{TeV}$. The LHC recorded physics data at $\sqrt{s} = 7\,\text{TeV}$ in 2010-2011, $\sqrt{s} = 8\,\text{TeV}$ in 2012, and restarted in May 2015 at $\sqrt{s} = 13\,\text{TeV}$. A thorough description of the LHC can be found in Ref. [34].

The LHC is a storage ring in a multi-stage accelerator complex at CERN (Fig. 2.1). The proton source for the LHC is ionized hydrogen gas. The ionized protons pass through a linear accelerator reaching 0.05 GeV (LINAC2). The LINAC2 beam is injected into the proton synchrotron booster (PSB) accelerating the protons to 1.4 GeV before injecting into the Proton Synchrotron (PS), which accelerates the beam to 25 GeV. The PS injects the protons into the Super Proton Synchrotron (SPS), which accelerates the protons to 450 GeV before final injection to the two counter-rotating beams of the LHC, where the protons are further accelerated to their final energy.

The accelerator complex includes several other experiments at CERN that share some stages with the LHC. The Compact Muon Solenoid (CMS) experiment is a general purpose detector located on the north side of the LHC and is one of four collision points for the circulating beams. A thorough description can be found elsewhere [36]. A Toroidal LHC Apparatus (ATLAS) is the other general purpose detector at the LHC and is located opposite CMS. The remaining two collision points are used by the LHCb experiment to study bottom quark processes and A Large Ion Collider Experiment (ALICE) for heavy ion collisions.

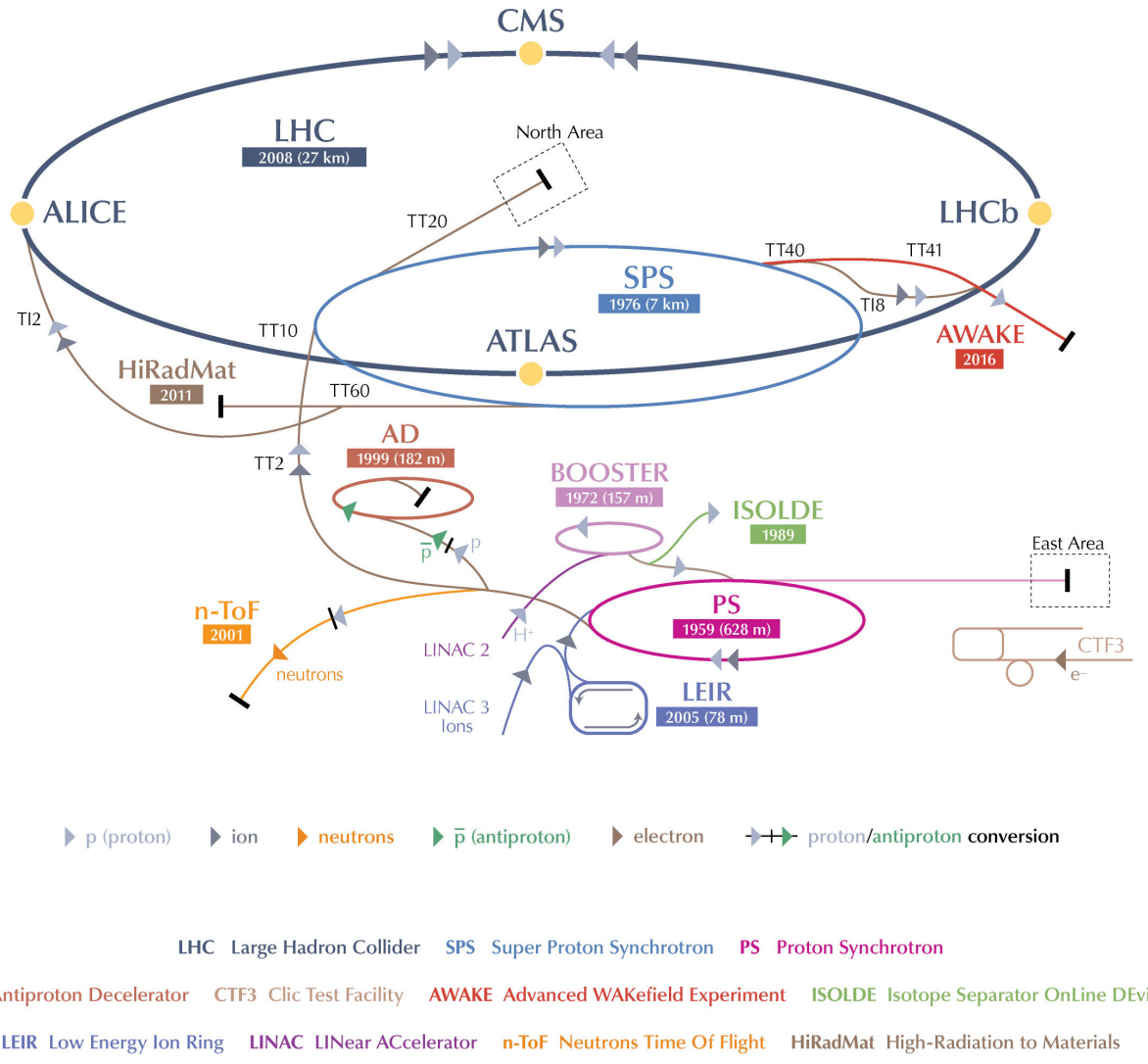

Figure 2.1: The LHC is one in a series of linked accelerators at CERN. The path of particles in the beam is shown to illustrate connections but is not to scale [35].

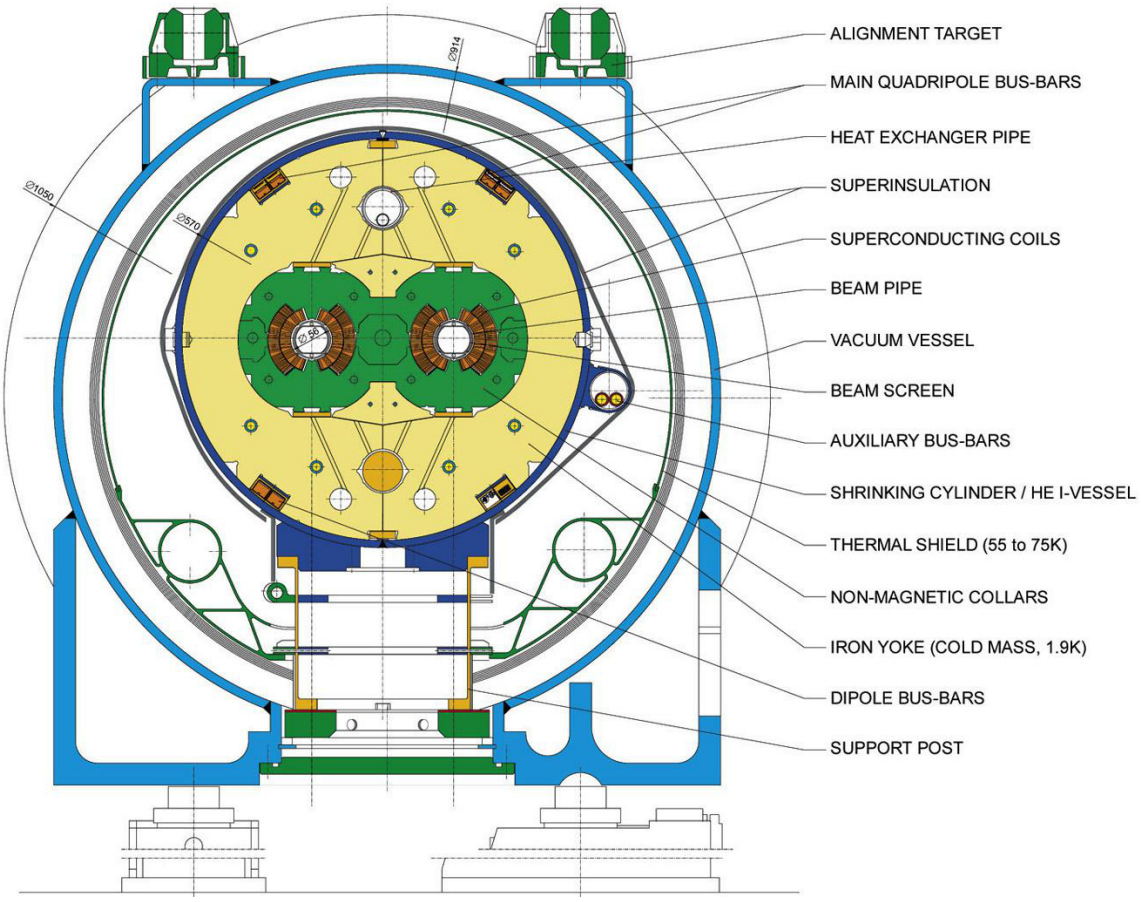

Figure 2.2: The LHC cross section featuring twin bore magnets containing the two proton beams in the tunnel [38].

The proton beams are bunched to provide appropriate timing for accelerator cavities and the duration of electronic readout from detectors. The protons are nominally bunched with 25 ns spacing with additional gaps to accommodate the injection and beam dump requirements. During peak luminosity running in 2012 the bunch spacing was 50 ns with 1.6×10^{11} protons per bunch and 1380 bunches per beam [37].

Owing to the lack of space in the tunnel, the LHC utilizes twin bore magnets with two beam channels within a single cryostat and mechanical housing (Fig. 2.2). The mechanical housing also supports three vacuum systems: the insulation vacuum for cryomagnets, the insulation vacuum for helium distribution, and the beam vacuum.

2.1.1 LHC performance

The goal of the LHC is to deliver high intensity beams of protons to collide at the detectors located around the ring. The number of collisions ($N_{pp\to X}$) is directly proportional to the luminosity (L) and the cross section of the process of interest ($\sigma_{pp\to X}$)

$$\frac{dN_{pp\to X}}{dt} = L\sigma_{pp\to X}, \tag{2.1}$$

where the machine instantaneous luminosity depends only on the beam parameters. For a Gaussian beam, L is given by

$$L = \frac{N_b^2 n_b f_{rev}\gamma_r}{4\pi\varepsilon_n\beta^*}F \tag{2.2}$$

where N_b is the number of particles per bunch, n_b is the number of bunches per beam, f_{rev} is the revolution frequency, γ_r is the relativistic gamma factor, ε_n is the normalized transverse beam emittance, β^* relates to the transverse size of the proton beam at the collision point, and F is given by the geometric luminosity reduction factor due to the crossing angle at the interaction point (IP). F is given by

$$F = \left(1 + \left(\frac{\theta_c\sigma_z}{2\sigma^*}\right)^2\right)^{-1/2} \tag{2.3}$$

where θ_c is the full crossing angle at the IP, σ_z is the root mean square (RMS) bunch length, and σ^* is the transverse RMS beam size at the IP. The LHC achieved a peak proton-proton luminosity of $7.7 \times 10^{33}\,\mathrm{cm}^{-2}\,\mathrm{s}^{-1}$ during the 2012 run (Fig. 2.3).

Since analyses are often concerned with the total number of events detected by an experiment, Eq. 2.1 can be integrated over time:

$$N_{\text{event}} = \mathcal{L}\,\sigma_{\text{event}} \tag{2.4}$$

where $\mathcal{L} = \int L\,dt$ is the integrated luminosity [39]. The total integrated luminosity delivered to CMS by the LHC in 2012 is $23.3\,\mathrm{fb}^{-1}$ (Fig. 2.4).

2.2 CMS detector

CMS is cylindrical in shape with the beam line along the central axis and consists of five concentric parts: the tracker, two types of calorimeters, the magnet, and the muon system (Fig. 2.5). The central feature of the CMS apparatus is a superconducting solenoid of 6 m internal diameter providing a magnetic field of 3.8 T. Within the superconducting solenoid volume are silicon pixel and

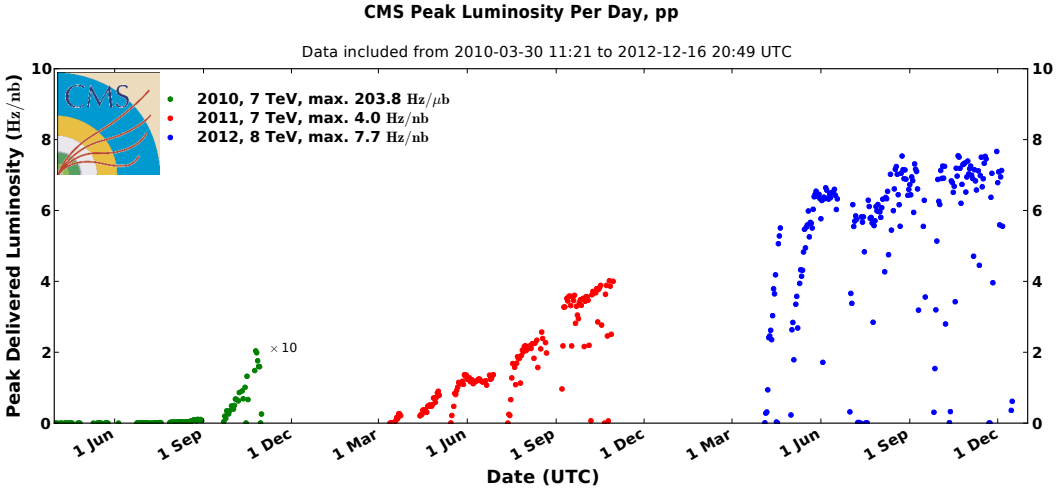

Figure 2.3: The daily peak luminosity delivered to CMS by the LHC during the first three years of operation. This is shown for 2010, 2011 and 2012 data-taking. The 2010 luminosity is multiplied by a factor of 10 for visibility.

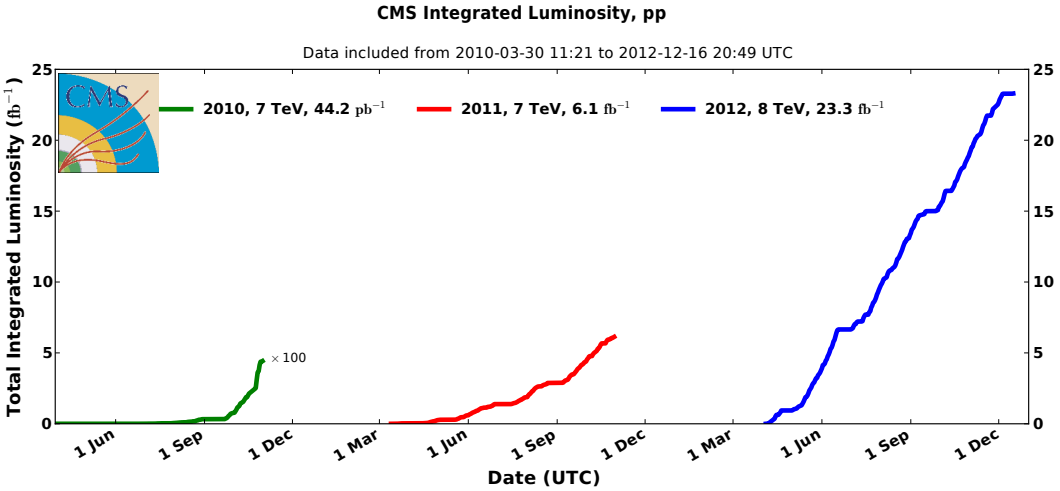

Figure 2.4: The integrated luminosity delivered to CMS by the LHC. Shown for 2010, 2011 and 2012 data-taking. The 2010 luminosity is multiplied by a factor of 100 for visibility.

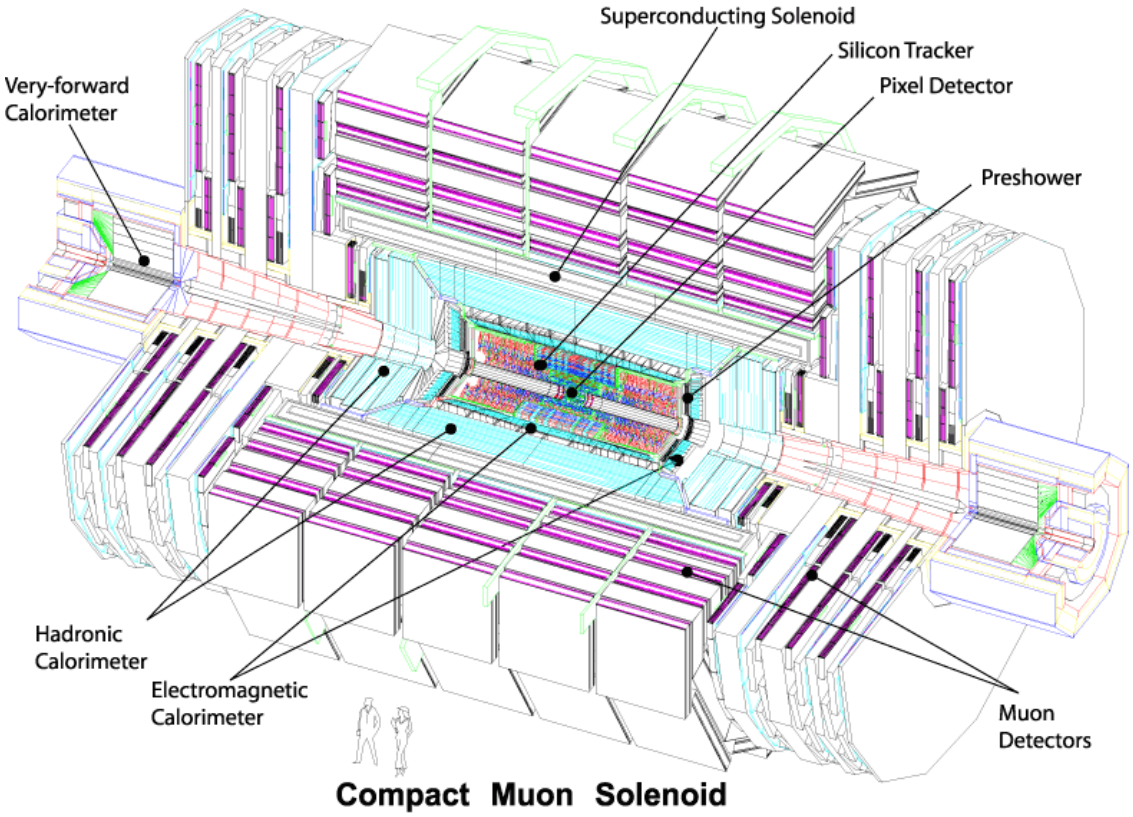

Figure 2.5: The CMS detector is composed of multiple concentric subdetectors. This cutaway view shows the internal structure with the beam line pointed along the cylindrical axis. Reprinted from [36].

strip trackers, a lead tungstate crystal electromagnetic calorimeter (ECAL), and a brass/scintillator hadron calorimeter (HCAL), each composed of a barrel and two endcap sections. Extensive forward calorimetry complements the coverage provided by the barrel and endcap detectors [40]. Muons are measured in gas-ionization detectors embedded in the iron flux-return yoke outside the solenoid.

The CMS experiment uses a right-handed coordinate system, with the origin at the nominal interaction point, the x axis pointing toward the center of the LHC, the y axis pointing upward (perpendicular to the LHC plane), and the z axis along the counterclockwise-beam direction. The polar angle θ is measured from the positive z axis and the azimuthal angle ϕ is measured in the x-y plane. The pseudorapidity (η) is defined as:

$$\eta = -\ln\left(\tan\left(\frac{\theta}{2}\right)\right). \tag{2.5}$$

Pseudorapidity is convenient due to the fact that differences in η are Lorentz invariant with respect to boosts along the beam axis. The ECAL barrel is located at $|\eta| < 1.48$ while the endcaps are from $1.48 < |\eta| < 3.0$.

By considering how a particle interacts with the subdetectors, the particle may be identified. An "event" refers to a crossing of two proton bunches at the interaction point. Some experimental challenges arise from the high number of proton-proton interactions per bunch crossing. During the 2012 data collection period there were on average 21 interactions per bunch crossing.

Missing transverse energy ($\not\!\!E_T$) is defined as the imbalance of transverse energy. $\not\!\!E_T$ can be calculated since the protons are colliding head-on and there is no initial momentum in the transverse direction, so from conservation of momentum the sum of final transverse energy should be zero. Representing the momentum of the ith particle in an event with N particles as $\vec{p}_i = (p_x, p_y, p_z)$ the missing transverse energy is defined as

$$\not\!\!E_T = \left| -\sum_{i}^{N} \vec{p}_i \right| . \tag{2.6}$$

Therefore ideally any excess of transverse energy is a signature of particles passing undetected through the systems. Studies of missing transverse energy can be found in Ref. [41].

2.2.1 Solenoid

The solenoid of CMS is designed to provide muon momentum resolution of $\Delta p/p \approx 10\%$ at $p = 1\,\text{TeV}$. Studies using 2010 data at $\sqrt{s} = 7\,\text{TeV}$ have shown this was achieved [42]. The large diameter bore allows the tracker, ECAL, and HCAL subsystems to be situated inside the solenoid. The winding is in 4 layers of reinforced conductor to withstand the hoop stress. The operating temperature for the magnet is 4.6 K. The flux is returned by a 10 000 ton iron yoke layered within the muon system. Basic characteristics of the CMS superconducting solenoid are listed in Table 2.1. The magnet also serves as the primary support structure for the detectors.

2.2.2 Tracker

Charged particles passing through the tracker cause ionization currents that are amplified by readout chips. The energy deposition in the tracker differentiate charged and neutral particles and provide a first estimate of the trajectory for charged particles.

Table 2.1: Characteristics of the CMS superconducting solenoid [36].

Field	3.8 T
Inner bore	5.9 m
Length	12.9 m
Number of turns	2168 m
Current	19.5 kA
Stored energy	2.7 GJ
Hoop stress	64 atm

The tracker is composed of three layers of silicon pixels ($100 \times 150\,\mu$m transverse pixel size), four layers of silicon microstrips ($10\,\text{cm} \times 180\,\mu$m transverse microstrip size), and six layers of wider silicon microstrips ($25\,\text{cm} \times 180\,\mu$m transverse microstrip size) [43]. These correspond to three different regions of particle flux at radii up to 11 cm, 55 cm, and 110 cm, respectively, from the interaction vertex. These layers of silicon can record the transverse impact parameter of a particle to within $10\,\mu$m, dominated by the resolution of the first pixel hit. In total there are 66 million silicon pixels and 9.6 million silicon strips with associated readout electronics (see Fig. 2.6). The design of the tracker provides high resolution with low individual occupancy (on the order of 1%). The material in the tracker represents 0.4 radiation lengths (X_0) at $\eta = 0$, $1.0\,X_0$ at $\eta \approx 1.6$, and $\approx 0.6\,X_0$ at $\eta = 2.5$ [44].

2.2.3 ECAL

To meet the physics goals of the LHC program, CMS requires a high-quality electromagnetic detection system [45]. The ECAL is used to identify photons and electrons, measure the energy of jets, and assist in measuring missing transverse energy. The search for the Higgs boson required good diphoton mass resolution ($\approx 1\%$ at 100 GeV) to increase the discovery potential in the $H \to \gamma\gamma$ channel. Fast readout and radiation hardness are necessary to accommodate nominally 20 interactions every 25 ns.

To satisfy these requirements, the ECAL consists of arrays of lead tungstate ($PbWO_4$) crystals. The high density crystals have a short radiation length (0.89 cm), a reasonable interaction length (22.4 cm), a small Moliére radius (2.19 cm), and rapid scintillation (60% light decay in 15 ns). The scintillation is proportional to the energy deposited by an interacting particle and is read out by

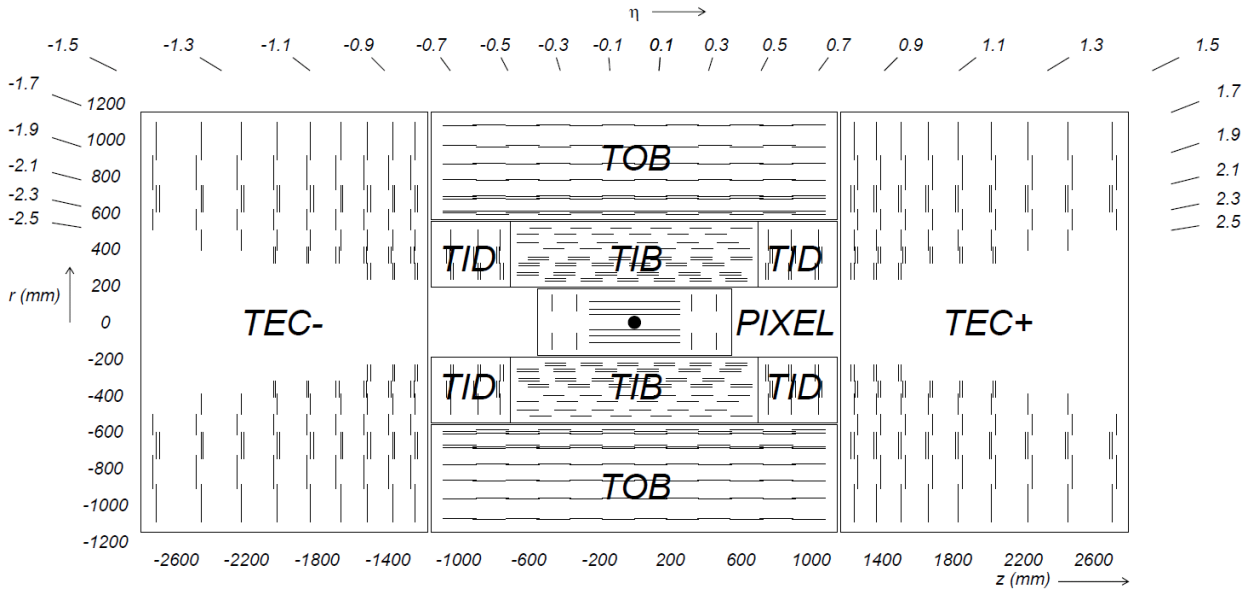

Figure 2.6: The CMS tracker schematic side view. The pixel detector (PIXEL) is the innermost piece. The tracker inner barrel (TIB) and tracker outer barrel (TOB) surround the pixel detector with cylinders of strip detectors. The forward region is covered by the tracker inner disks (TID) and the tracker endcaps (TEC±). The silicon pixels and strips are grouped into modules shown as line segments in this schematic of the CMS tracker. Reprinted from [36].

photodetectors mounted on the outer radius of the ECAL crystals. The ECAL also has a preshower detector to prevent misidentification of two low energy photons as one high energy photon [46].

The $PbWO_4$ crystals do pose some challenges. The crystal response is sensitive to temperature, so the temperature across all the crystals is kept at $18 \pm 0.05^\circ$ C to maximize light yield. The crystal transparency decreases when exposed to ionizing radiation but partially recovers naturally over time when the source is removed. A laser monitoring system tracks the ECAL transparency and appropriate corrections are applied to the crystal output.

There are two types of photodetectors mounted on the crystals: avalanche photodiodes (APDs), for the ECAL barrel, and vacuum phototriodes (VPTs) on the endcaps. VPTs were necessary on the endcaps due to their greater radiation hardness. In 2010 the APDs were a suspected source of anomalous high energy deposits recorded in the ECAL barrel (called "spikes"). By leveraging the unique shape and timing of the spikes, a filtering algorithm was designed to remove this spurious signal from data [47].

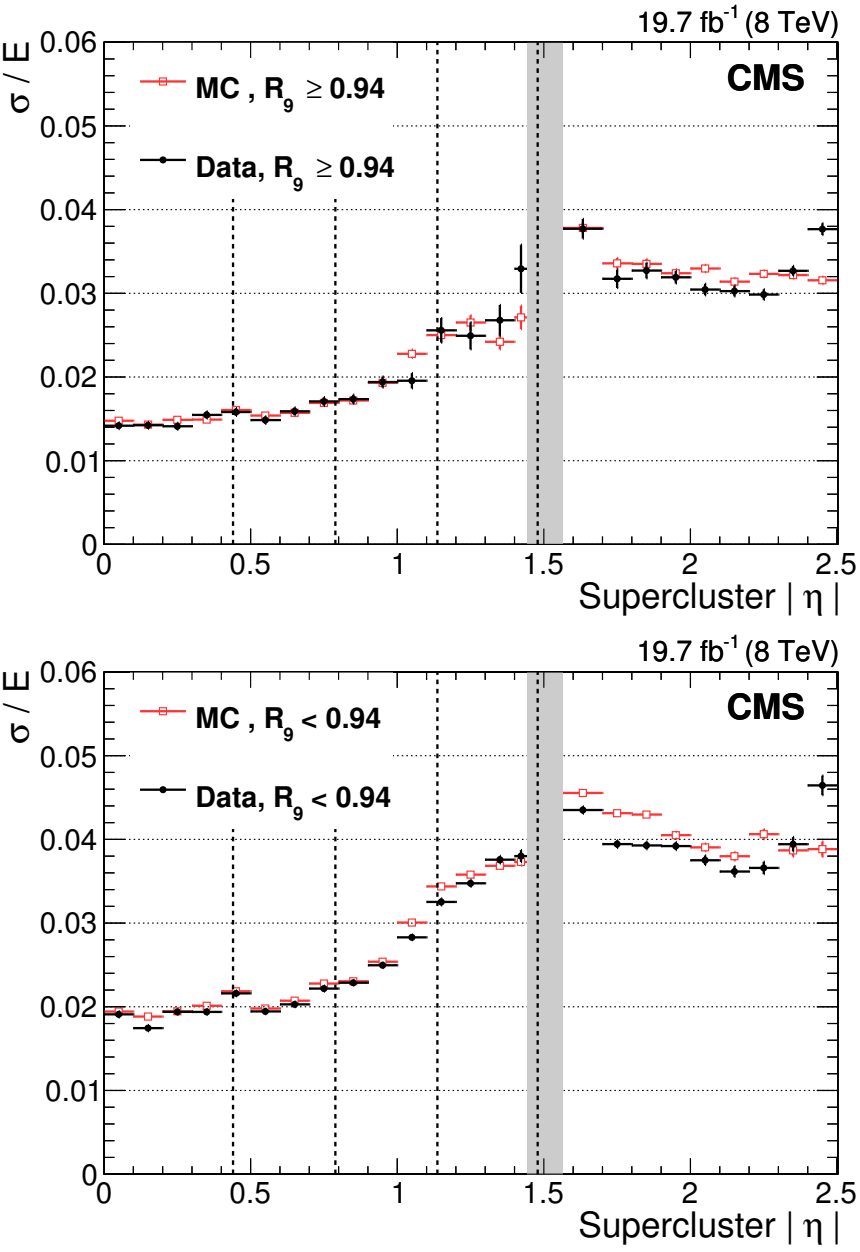

Figure 2.7: The ECAL electron energy resolution. Using electrons from $Z \to e^+e^-$ the relative energy resolution of the ECAL is compared with Monte Carlo events for 2012. The resolution is shown for barrel and endcap separated by the vertical gray band. The two plots differentiate high and low values of the variable $R9$ (unconverted photons have high $R9$ values, see 4.4). Reprinted from [48].

Analysis of the ECAL performance with 2012 data shows slightly lower resolution in data than Monte Carlo (MC) simulation for $Z \to ee$ events (Fig. 2.7). A small smearing term is extracted and applied to the electron and photon energy in MC to correctly model the detector response and account for the discrepancy. Possible sources of the difference include the modeling of the tracker material, geometric description of the tracker and ECAL, and imperfect calibration between the crystals. The corrected resolution for $E_T \approx 45\,\text{GeV}$ electrons from Z-boson decays is better $\approx$0.7 (1)% to 1 (2)% in the barrel for high (low) R_9 and from 1.6 to 2.0% in the endcaps. The uncertainties in these numbers are about 0.05–0.1% depending on the category [48]. This makes the CMS detector very useful for discovering particles beyond those of the SM that decay to multiple photons.

2.2.4 HCAL

The HCAL is a sampling calorimeter of alternating brass or steel plates with plastic scintillator [49]. An important role of the HCAL is to absorb the energy of most of the remaining particles (e.g. hadrons) to provide an accurate measurement for the missing transverse energy ($\not\!\!E_T$) from the event. This led to a design with hermetic coverage out to $|\eta| < 5.0$. To maximize the containment inside the magnet, brass is used as the absorber due to the facts that it has a short interaction length (16.42 cm), is non-magnetic, and is easy to machine. Plastic scintillator tiles (with a width and length of 3.7 cm) are bolted between the brass layers. The scintillation light from the active material is channeled through clear fibers to the readout system.

The CMS barrel is segmented into sections in η and ϕ from $-1.4 < \eta < 1.4$ with additional sections in the endcap out to $|\eta| < 3.0$. The sections are referred to as towers. The forward calorimeter has 900 towers covering $3.0 < |\eta| < 5.0$ with quartz fibers and steel absorber chosen for the harsher radiation inherent to the forward region. The sampling calorimetry inside the solenoid is complemented by scintillator on the outside of the magnet that effectively increases the interaction length of the HCAL. The outer hadronic calorimeter samples any remaining energy leakage.

2.2.5 Muon system

The muon system is the outermost layer of the detector since high momenta muons produced at the interaction point are likely to be the only standard model particles that pass through the inner subdetectors and solenoid without being stopped. Iron layers interspersed within the muon system

serve a dual purpose of a return yoke for the magnetic field to the solenoid and an absorber for the muon system. The muon system includes three detector types: drift tubes, cathode strip chambers, and resistive plate chambers. The drift tubes are located in 12 layers through the barrel and give position data. The cathode strip chambers serve the same purpose in the endcap. The resistive plate chambers operate in parallel with the drift tubes and cathode strip chambers but provide a much faster readout ($\approx$ 1 ns). The resistive plate chambers have lower spatial resolution but provide the trigger system information rapidly to enable a low level, realtime, hardware decision on whether to store an event [50].

2.2.6 Trigger system

The quantity of interactions occurring in the CMS detector with every bunch crossing requires a strong filter to reduce the rate and size of the information recorded, this is the purpose of the trigger and data acquisition (DAQ) system. The CMS trigger and DAQ system is limited to recording $\approx 10^2$ interactions/sec onto archive media out of the $\approx 10^9$ interactions/sec at design luminosity. The process of selecting which events to archive is done in two steps, the Level-1 (L1) trigger and the High-Level Trigger (HLT). The archived data size is $\approx$ 1 MB for each bunch crossing.

The Level-1 trigger logic is composed of custom hardware housed in a service cavern adjacent to the CMS detector. The signals from the front-end electronics are analyzed by the L1 logic based on "trigger primitive" physics objects. An event of interest is read out to the HLT based on the transverse energy and momentum thresholds of simplified photons, electrons, muons and jets from the event. The output rate limit of the L1 trigger is 100 kHz determined by the average time for full detector information to transfer through the readout system.

The High-Level Trigger processor farm is located above ground and utilizes commercial hardware to execute more sophisticated decision algorithms. Purchasing commodity computer processors for the HLT as late as possible leveraged the evolution of technology to provide the best quality event reconstruction to reduce the 100 kHz input to 100 Hz for offline analysis. The accepted events and a sample of rejected events are sent to the online monitoring system to ensure proper running during data taking. Further details may be found elsewhere [51].

CHAPTER 3

THEORY

Despite the success of the SM compared to virtually all experimental results about which it makes predictions, scientists must pursue all avenues in the search for an observed disagreement. There are also several problems with the SM that lead physicists to suspect that a more fundamental theory exists. The SM has no mechanism for gravity, the accelerated expansion of the universe, or a mechanism to explain the imbalance in the number of particles and antiparticles seen in nature.

There is a clear need for a beyond the SM theory of physics (BSM). From the dearth of evidence for any BSM, either the new physics is beyond the energy reach of the LHC or the new physics is present in a manner that eludes simple detection. The discovery of a Higgs-like particle at the LHC favors more elusive BSM models [52]. Whenever possible, it is worthwhile to search for evidence of classes of BSM models. One such class of models proposed by Kilic, Okui, and Sundrum is called "vectorlike confinement" [1].

3.1 Vectorlike confinement

The phenomenology of interest arises from the introduction of new fermions ("hyperquarks") in vectorlike representations of the SM gauge groups. The new fermions may interact strongly with a new gauge force (called "hypercolor") that confines at the TeV scale. These two characteristics combine to generate an interesting class of models that predict phenomena that may have escaped previous search efforts. Since the model involves vectorlike fermions, there are no constraints from precision electroweak observables and the model can coexist with the Higgs sector that breaks electroweak symmetry. The nomenclature for the hypothetical particles is indicative of the analogy with QCD as it relates to QED at the GeV scale. Just as an e^+e^- sub-GeV collider produces bound state mesons from color-confined quarks, so too would the LHC produce "hypermesons" that may decay to SM particles.

A signature feature of vectorlike confinement is the resonant production of hyperrho mesons ($\tilde{\rho}$) and the decay of $\tilde{\rho}$ to a pair of hyperpions ($\tilde{\pi}$) as in Fig. 3.1. Although similar in some aspects

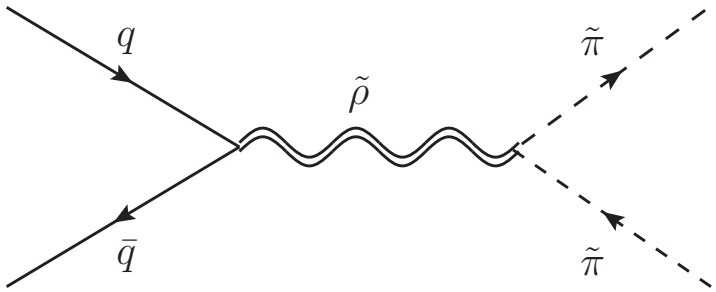

Figure 3.1: The Feynman diagram for the $\tilde{\rho} \to \tilde{\pi}\tilde{\pi}$ process. Reproduced from [53].

to resonant searches for Z', W' and g' [32, 33], the $\tilde{\rho}$ does not decay directly to SM particles [53]. These earlier resonance searches were dominated by dijet and dilepton channels. The $\tilde{\rho} \to \tilde{\pi}\tilde{\pi}$ is a general feature of vectorlike confinement but a wide variety of final states are possible depending on how the $\tilde{\pi}$ decays. There are three kinds of $\tilde{\pi}$, a weak doublet ($\tilde{\pi}_{\mathrm{D}}$), a weak triplet ($\tilde{\pi}_{\mathrm{T}}$), and a singlet ($\tilde{\pi}_{\mathrm{S}}$). The weak triplet state is the only one with significant discovery potential at the LHC and the branching fraction for $\tilde{\pi}^0_{\mathrm{T}}$ can be seen in Fig. 3.2 and for $\tilde{\pi}^{\pm}_{\mathrm{T}}$ in Fig. 3.3.

In Ref. [53] a benchmark model with characteristic phenomenology including pair produced collider stable charged massive particles (di-CHAMP) and multiphoton final states is studied. The di-CHAMP model has been explored by a study from the CMS Collaboration in Ref. [29]. The three-photon final state process from the vectorlike confinement hypothesis is investigated in the work presented here.

3.2 Signal simulation

The parameters in Table 3.1 were used in conjunction with the Standard Model to generate signal Monte Carlo simulated events (MC). For this model, the QED-QCD analogy is exploited to extract appropriate values and reduce the number of required parameters. For example, $f_{\tilde{\pi}}$ is a scaled up analogue to the QED-QCD pion decay constant f_π, so $f_{\tilde{\pi}} \approx f_\pi \, m_{\tilde{\rho}}/m_\rho$.

Signal MC simulation events are generated using FeynRules 1.6.11 [54] and MadGraph 1.5.10 [55]. The software Pythia simulates the hadronization of the tree-level generated particles [56]. Simulated events are processed through the CMS software (CMSSW) 5.3.2 software for detector simulation, digitization, pileup simulation, and reconstruction [57].

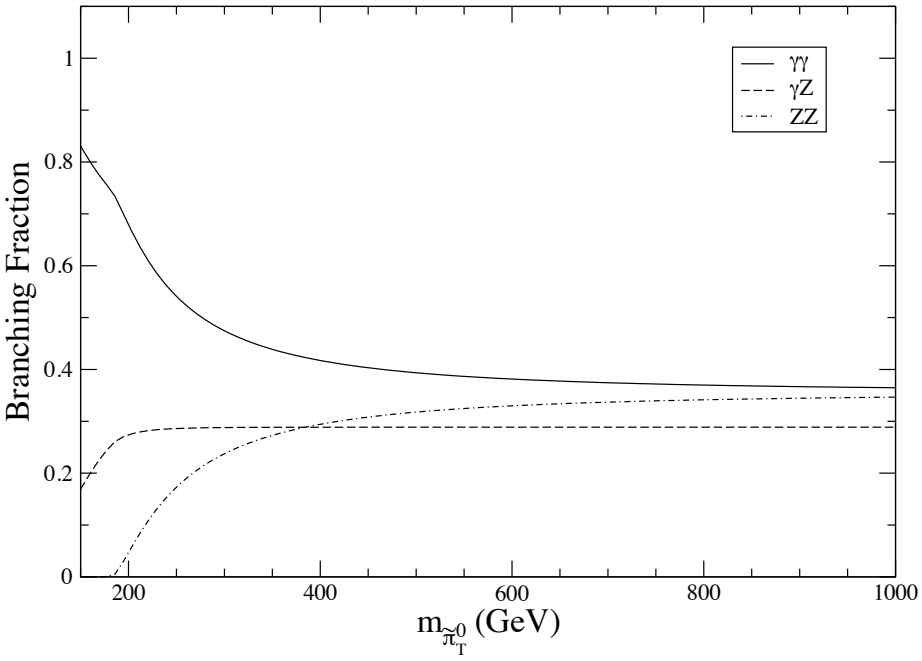

Figure 3.2: The branching fractions of $\tilde{\pi}_{\mathrm{T}}^{0}$. Reproduced from [53].

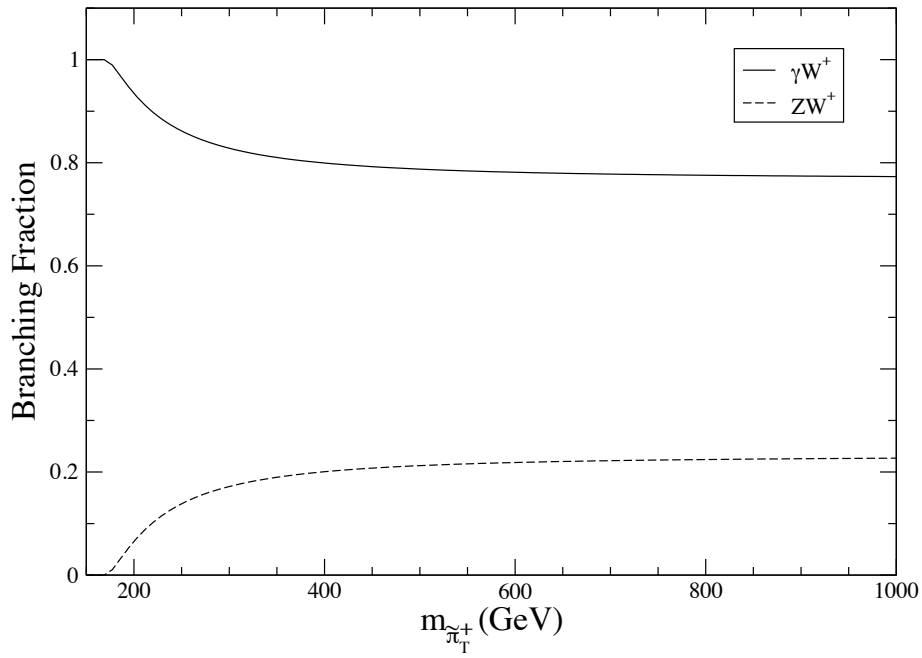

Figure 3.3: The branching fractions of $\tilde{\pi}_{\mathrm{T}}^{+}$, which are the same for the charge conjugate process ($\tilde{\pi}_{\mathrm{T}}^{-}$). Reproduced from [53].

Table 3.1: The vectorlike confinement parameters for the benchmark model [53].

Symbol	Description	Value
δ	Coupling of $\tilde{\rho}$ to Standard Model fermions.	0.2
$g_{\tilde{\rho}}$	hyper-rho meson coupling to hyperpions.	6.0
$m_{\tilde{\rho}}$	Neutral and charged hyper-rho meson mass.	1.00 TeV
$f_{\tilde{\pi}}$	$\tilde{\pi}$ to Standard Model gauge boson coupling	200 GeV

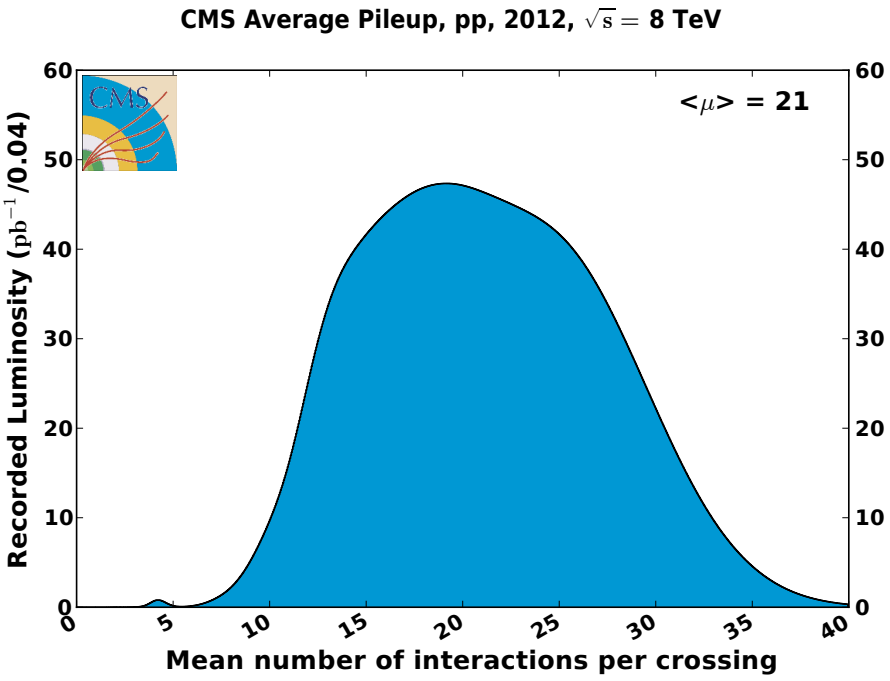

Figure 3.4: Distribution of average pileup in 2012 CMS data.

Pileup refers to any hard scattering interactions that leave energy in the detector which is not from the main scattering that passed the trigger criteria. Simulated events are given an initial estimated pileup distribution however that is later adjusted through pileup reweighting. Pileup reweighting gives a new weight to each generated event by scaling the simulated events' pileup distribution to match the distribution of pileup in the selected data. The average distribution of pileup in 2012 data is shown in Fig. 3.4. The MC simulated events uses the same reconstruction algorithms as data.

The phenomenology of "vector-like confinement" has been previously explored for different conditions [53]. Figures 3.5-3.8 show important photon-related distributions for the model used

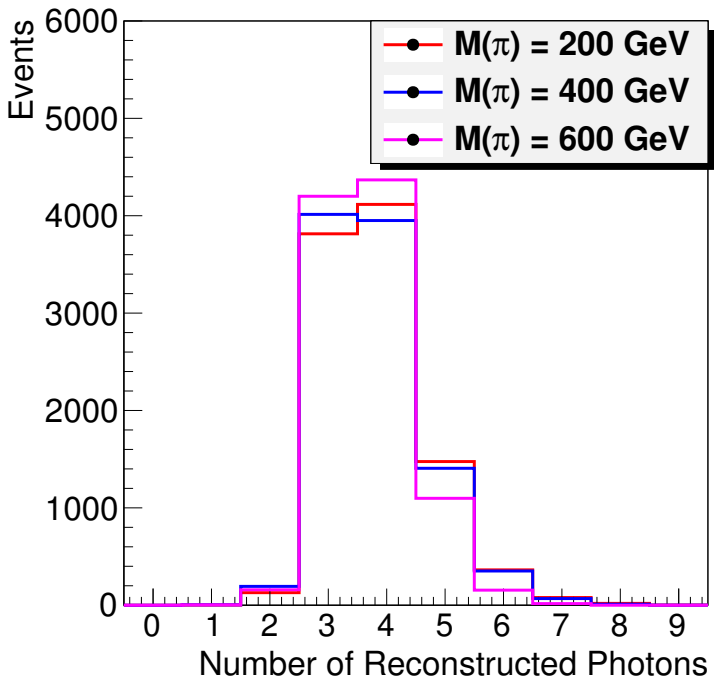

Figure 3.5: The number of reconstructed photons per event for signal samples with $\tilde{\pi}$ masses of 200 (red), 400 (blue), and 600 GeV (magenta). All samples are normalized to 10,000 generated events.

here with three different $\tilde{\pi}$ masses (200, 400, 600 GeV). Reconstructed photons are used in all plots. While the signal has three photons from the $\tilde{\pi}$ decays, Fig. 3.5 shows that for more than half the events additional photons are observed. However, Fig. 3.6 indicates that the additional photons tend to be lower energy.

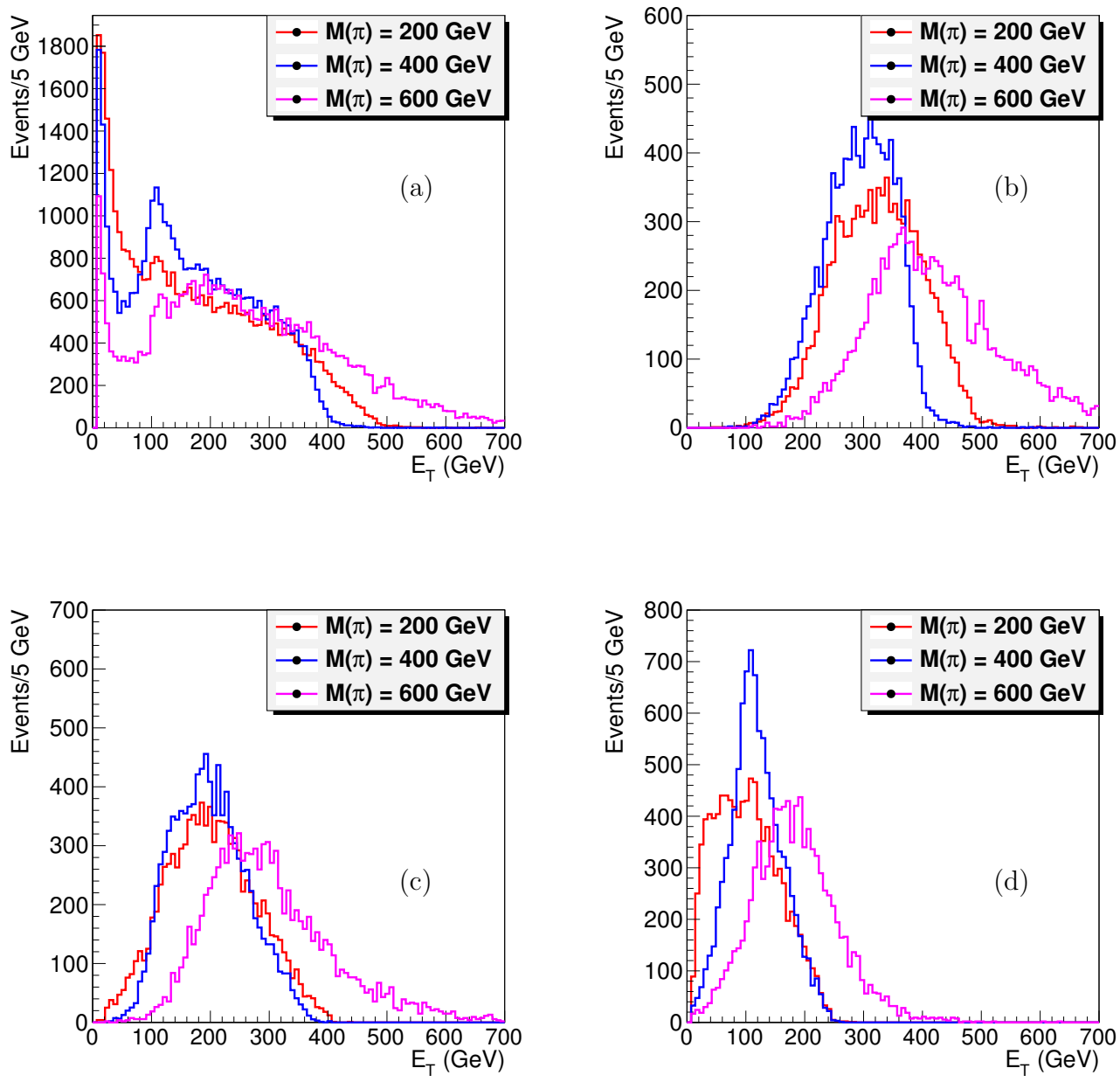

Figure 3.6: Distributions of transverse energy of reconstructed photons for signal samples with $\tilde{\pi}$ masses of 200 (red), 400 (blue), and 600 GeV (magenta). The distributions are (a) the E_{T} of all photons, (b) the E_{T} of the leading (highest energy) photon, (c) the E_{T} of the second leading photon, and (d) the E_{T} of the third leading photon. All samples are normalized to 10,000 generated events.

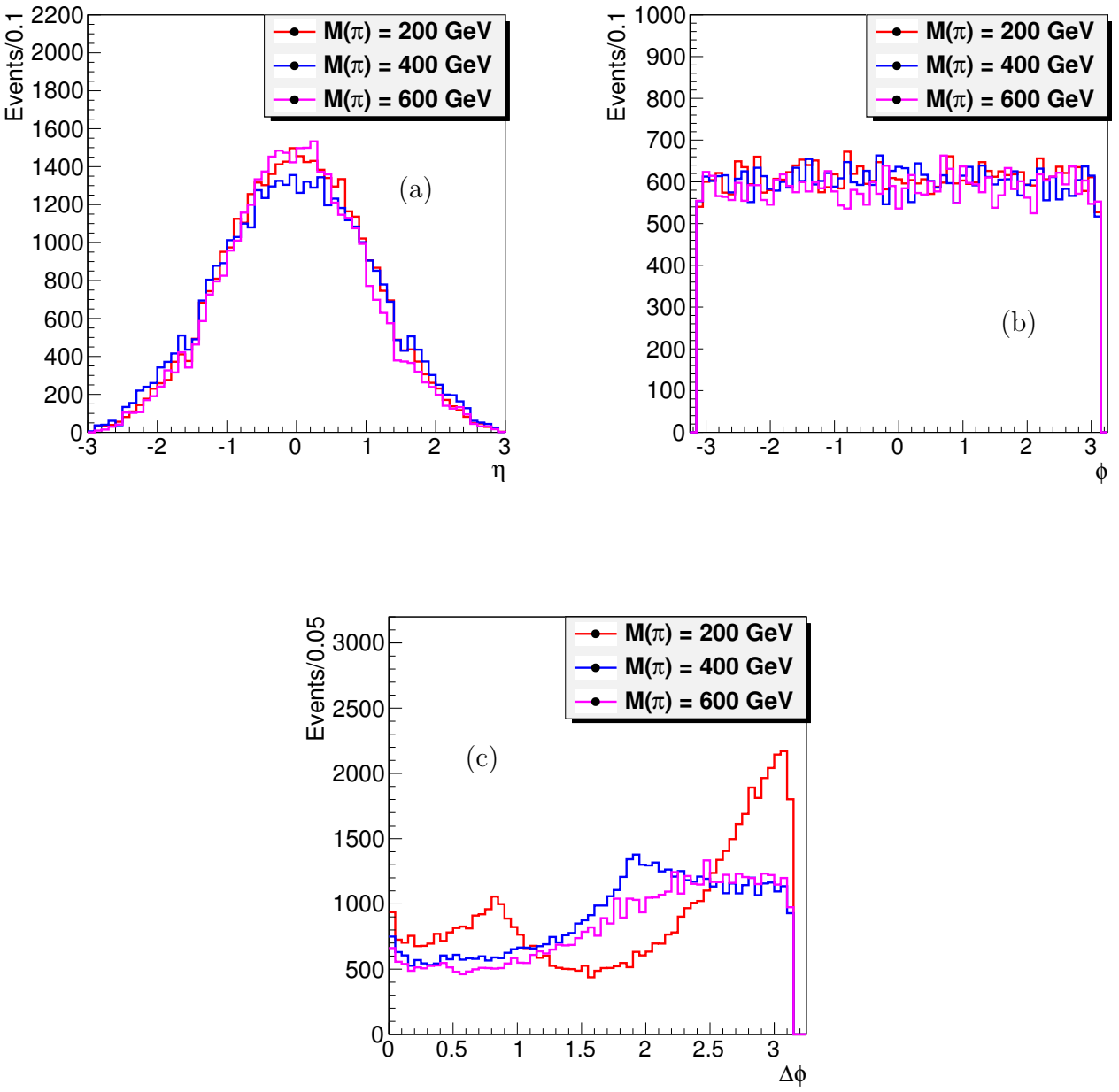

Figure 3.7: Distributions of angular variables of reconstructed photons for signal samples with $\tilde{\pi}$ masses of 200 (red), 400 (blue), and 600 GeV (magenta). The distributions are (a) the η of all photons, (b) the ϕ of all photons, and (c) the $|\Delta\phi|$ between all pairs of photons. All samples are normalized to 10,000 generated events.

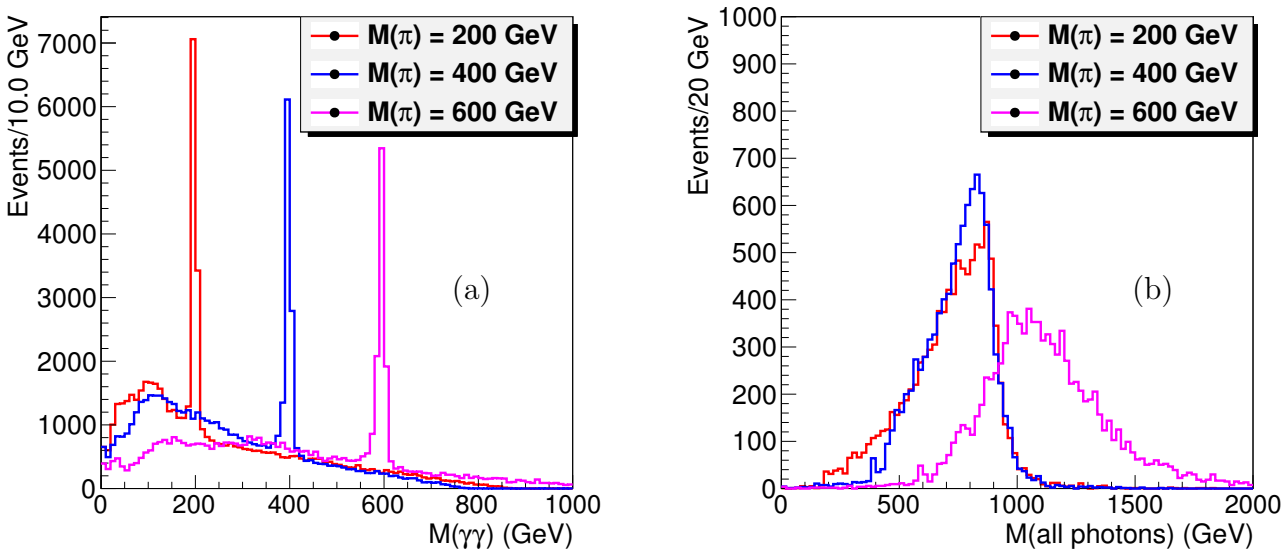

Figure 3.8: Distributions of invariant mass of reconstructed photons for signal samples with $\tilde{\pi}$ masses of 200 (red), 400 (blue), and 600 GeV (magenta). The distributions are (a) the invariant mass of all photon pairs and (b) the invariant mass of the sum of all photons in an event. All samples are normalized to 10,000 generated events.

CHAPTER 4

THE DATA

4.1 Integrated luminosity

The data used in this analysis were recorded from March 4 to October 20 of 2012, yielding a total integrated luminosity of 13.7 fb^{-1} delivered and 12.3 fb^{-1} recorded. The integrated luminosity (see Eq. 2.2) recorded by the CMS detector is lower than the integrated luminosity delivered by the LHC due to times when the CMS detector is not on because of technical problems, safety concerns, or time required for reconfiguring the detector. Hence the CMS detector may not record data even though the LHC may be providing collisions. As seen in Fig. 4.1, the total difference in 2012 amounts to approximately 6.5% of collisions reported by the LHC but not recorded by CMS.

4.2 Data quality

The data gathered by the CMS detector go through two stages of quality checks to ensure the components of the detector are functioning correctly. Basic functionality of the detector is monitored during data taking, called "online" monitoring, and analysis of the recorded data "offline" is done before the recorded data is certified as good for use in physics analyses by the collaboration.

4.2.1 Online monitoring

During data recording each subsystem is monitored by trained CMS collaboration members, working in shifts. This includes information such as the average occupation for the Front End Electronics (FEDs) as well as safety conditions such as the operating temperature. Possible problems with subsystems discovered online may be rectified during data taking by experts on call or flagged for offline follow-up. Part of my service work as a CMS member included online shifts at the CMS experiment site (P5) as the ECAL contact during data recording. An example monitoring screen from when I worked as the ECAL shift leader is shown in Fig. 4.2. I also served as the Expert on Call for the ECAL subsystem ensuring any problems that occurred during data taking were resolved quickly. One of my duties was to give certification results for the data recorded by the

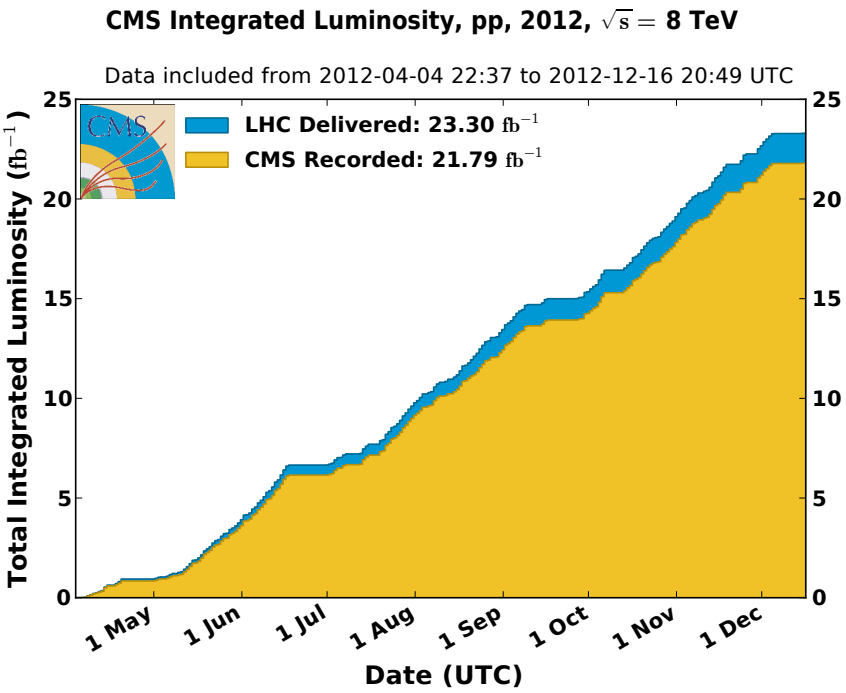

Figure 4.1: Cumulative luminosity delivered and recorded by the CMS detector.

ECAL subsystem each week and present weekly to the ECAL Prompt Feedback Group. The certification results from each subsystem were used as the basis for data certification which ultimately resulted in a list of periods when the detector was in a good condition for physics analysis.

4.2.2 Data certification

Each week of CMS data recording, the run sections are certified good or bad by the subdetector and Physics Object Groups (POG). A JavaScript Object Notation (JSON) file is published internally listing the ranges of good sections called "certified data". An early step in filtering events used for this analysis was to exclude any bad runs using a JSON file. The JSON file used for this analysis is Cert_190456-205618_8TeV_PromptReco_Collisions12_JSON.txt from the CMS Collaboration directories.

4.3 Datasets

The CMS Collaboration sorts the recorded data into datasets based on the triggers and run periods. Table 4.1 lists the datasets used in this analysis. As the instantaneous luminosity increased,

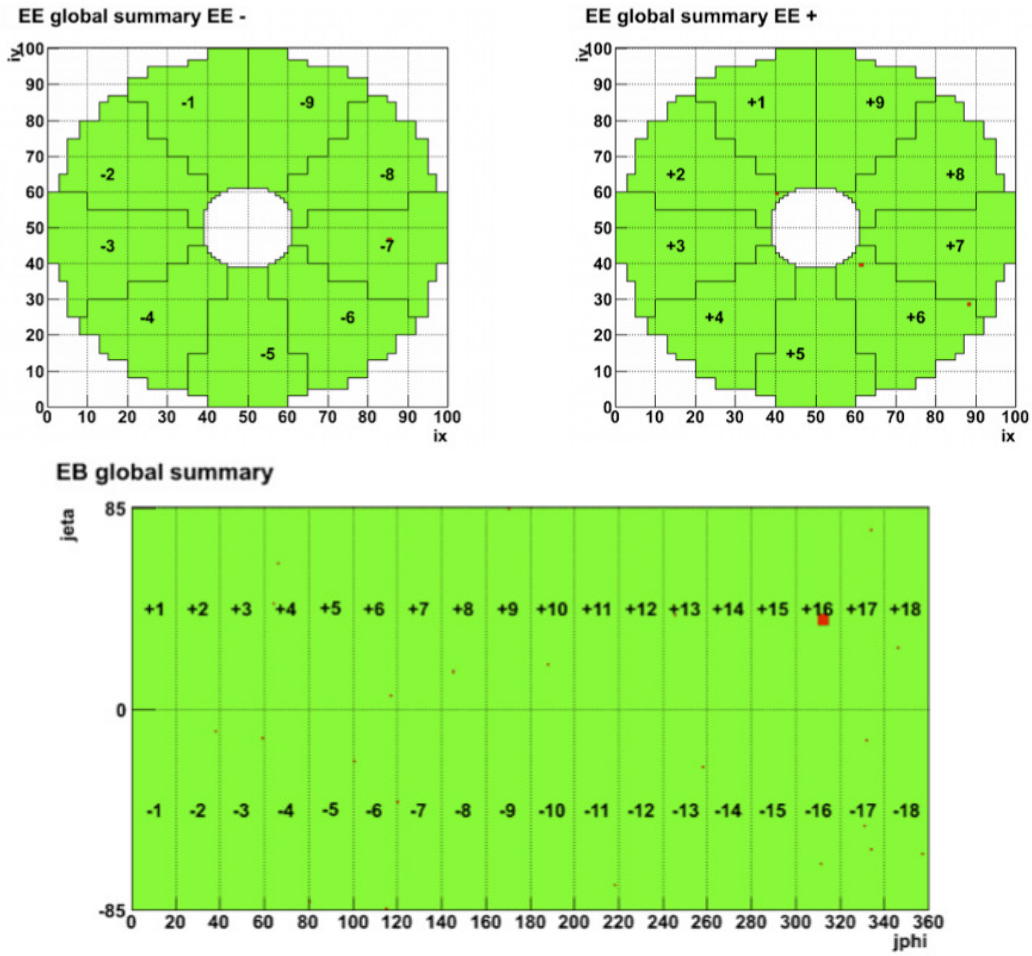

Figure 4.2: Screen capture from ECAL online monitoring. Reproduced from my ECAL prompt feedback group shift report in 2010. Green areas show no problems, while red areas indicate a possible issue that needs to be investigated. In this example you can see one large red rectangle in the ECAL barrel in super module +16. This Trigger Tower represented a 5x5 group of crystals controlled by a single FED with a software problem. Other minor red dots were individual crystals with varying degrees of operation. Later analysis by experts would determine if hits in these areas of the detector could be recovered with software modification or if they must be ignored.

the Photon dataset was split into single and double photon primary datasets to limit the trigger rate. The Analysis Object Data (AOD) format includes reconstructed physics objects intended for analyses [58]. Analyzed events are reduced from the "RecoPhoton" collection as categorized by the reconstruction algorithm, referred to subsequently in this analysis as the reco-photon collection. The HLT triggers used in the analysis are listed in Table 4.2 and Table 4.3.

Table 4.1: Datasets used in this analysis.

Dates	Dataset	Run range
2012-04-05 to 2012-05-08	/Photon/Run2012A-PromptReco-v1/AOD	190456-193621
2012-05-10 to 2012-06-18	/DoublePhoton/Run2012B-PromptReco-v1/AOD	193833-196531
2012-07-13 to 2012-09-27	/DoublePhoton/Run2012C-PromptReco-v2/AOD	198934-203746
2012-09-27 to 2012-12-06	/DoublePhoton/Run2012D-PromptReco-v1/AOD	203768-208686

Table 4.2: DoublePhoton triggers used in this analysis.

DoublePhoton HLT Trigger (seeded by L1_DoubleEG_13_7)
HLT_Photon26_CaloId10_Iso50_Photon18_CaloId10_Iso50_Mass60
HLT_Photon26_CaloId10_Iso50_Photon18_R9Id85_Mass60
HLT_Photon26_Photon18
HLT_Photon26_R9Id85_OR_CaloId10_Iso50_Photon18
HLT_Photon26_R9Id85_OR_CaloId10_Iso50_Photon18_R9Id85_OR_CaloId10_Iso50_Mass60
HLT_Photon26_R9Id85_OR_CaloId10_Iso50_Photon18_R9Id85_OR_CaloId10_Iso50_Mass70
HLT_Photon26_R9Id85_Photon18_CaloId10_Iso50_Mass60
HLT_Photon26_R9Id85_Photon18_R9Id85_Mass60
DoublePhoton HLT Trigger (seeded by L1_SingleEG22)
HLT_Photon36_CaloId10_Iso50_Photon22_CaloId10_Iso50
HLT_Photon36_CaloId10_Iso50_Photon22_R9Id85
HLT_Photon36_Photon22
HLT_Photon36_R9Id85_OR_CaloId10_Iso50_Photon10_R9Id85_OR_CaloId10_Iso50_Mass80
HLT_Photon36_R9Id85_OR_CaloId10_Iso50_Photon22
HLT_Photon36_R9Id85_OR_CaloId10_Iso50_Photon22_R9Id85_OR_CaloId10_Iso50
HLT_Photon36_R9Id85_Photon22_CaloId10_Iso50
HLT_Photon36_R9Id85_Photon22_R9Id85

4.4 Photon identification

Photons that interact with the ECAL detector will produce a cascade of lower energy particles, referred to as an electromagnetic shower. This shower will likely spread across multiple crystals in

Table 4.3: Photon triggers used in this analysis.

HLT Trigger	L1 seed
HLT_DoubleEle33_CaloIdL	L1_SingleEG22
HLT_DoubleEle33_CaloIdL_GsfTrkIdVL	L1_SingleEG22
HLT_DoubleEle33_CaloIdT	L1_SingleEG22
HLT_DoublePhoton40_CaloIdL_Rsq0p035	L1_SingleEG24
HLT_DoublePhoton40_CaloIdL_Rsq0p06	L1_SingleEG24
HLT_DoublePhoton43_HEVT	L1_SingleEG22
HLT_DoublePhoton48_HEVT	L1_SingleEG22
HLT_DoublePhoton5_IsoVL_CEP	L1_DoubleEG3_FwdVeto
HLT_DoublePhoton70	L1_SingleEG30
HLT_DoublePhoton80	L1_SingleEG30
HLT_Photon135	L1_SingleEG30
HLT_Photon150	L1_SingleEG30
HLT_Photon160	L1_SingleEG30
HLT_Photon20_CaloIdVL	L1_SingleEG12
HLT_Photon20_CaloIdVL_IsoL	L1_SingleEG12
HLT_Photon250_NoHE	L1_SingleEG30
HLT_Photon30_CaloIdVL	L1_SingleEG20 OR L1_SingleEG22
HLT_Photon30_CaloIdVL_IsoL	L1_SingleEG20 OR L1_SingleEG22
HLT_Photon300_NoHE	L1_SingleEG30
HLT_Photon50_CaloIdVL	L1_SingleEG20 OR L1_SingleEG22
HLT_Photon50_CaloIdVL_IsoL	L1_SingleEG20 OR L1_SingleEG22
HLT_Photon75_CaloIdVL	L1_SingleEG20 OR L1_SingleEG22
HLT_Photon75_CaloIdVL_IsoL	L1_SingleEG20 OR L1_SingleEG22
HLT_Photon90_CaloIdVL	L1_SingleEG20 OR L1_SingleEG22
HLT_Photon90_CaloIdVL_IsoL	L1_SingleEG20 OR L1_SingleEG22

the calorimeter. Photons are reconstructed by forming clusters of crystals in the ECAL. A simplified description of a photon is an ECAL cluster with no or minimal energy behind it in the HCAL and no track associated with the cluster. The HCAL energy requirement rejects hadrons while the track requirement rejects electrons. A more advanced description of the photon reconstruction algorithm is available in Ref. [48].

Since there are many particles that deposit energy into the ECAL, CMS has created criteria to identify photons (Table 4.4). There are three components used in photon identification by the CMS Collaboration: shower shape variables, isolation variables, and an electron veto. These criteria include information obtained from the energy deposition in the ECAL and the affiliated local energy maximum above a defined threshold known as the ECAL seed crystal. In the case of

a photon that has undergone positron-electron pair production through interaction in the tracker, the supercluster may be composed of multiple sub-clusters spread in ϕ by the magnetic field. Care is taken to not discard these events when removing electrons created at the primary vertex or from other proton proton interactions which were coincident with the primary interaction in the bunch crossing (the underlying event). Additionally, the candidate photon's transverse energy is required to be greater than 20 GeV for all photons.

Three sets of photon identification criteria are optimized to give peak background rejection at three target signal efficiencies: loose (90%), medium (80%), and tight (70%). Figure 4.3 shows the optimized background rejection versus signal efficiency achieved for each selection point from Table 4.4.

Table 4.4: The photon identification criteria recommended for CMS data analyses. The variables are discussed in Section 4.4.1. P_T^γ is the transverse momentum of the candidate.

Barrel Photons	loose	medium	tight
Electron Veto			
conversion safe electron veto	*yes*	*yes*	*yes*
Shower Shape Variables			
R_9	> 0.0	> 0.0	> 0.0
single tower H/E	< 0.05	< 0.05	< 0.05
$\sigma^2_{i\eta i\eta}$	< 0.012	< 0.011	< 0.011
Isolation Variables			
PF charged hadron isolation (GeV)	< 2.6	< 1.5	< 0.7
PF neutral hadron isolation (GeV)	$< 3.5 + 0.04 \cdot P_T^\gamma$	$< 1.0 + 0.04 \cdot P_T^\gamma$	$< 0.4 + 0.04 \cdot P_T^\gamma$
PF photon isolation (GeV)	$< 1.3 + 0.005 \cdot P_T^\gamma$	$< 0.7 + 0.005 \cdot P_T^\gamma$	$< 0.5 + 0.005 \cdot P_T^\gamma$
Efficiency	90%	80%	70%

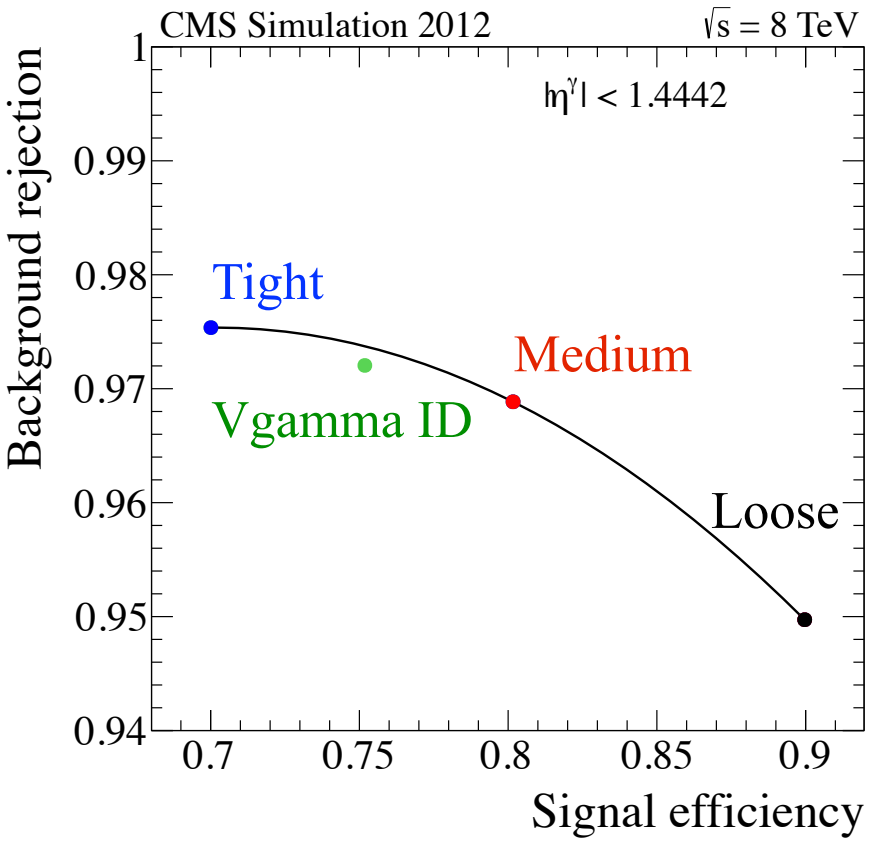

Figure 4.3: Background rejection versus signal efficiency for the 2012 recommended photon identification cuts. The green point shows the previous standard created by the Vgamma working group.

4.4.1 Shower shape variables

ECAL energy distribution (R_9). The variable R_9 is defined as a ratio of the sum of energy in the nine crystals encompassing and including the seed crystal ($E_{3\times3}$) and the total energy of the supercluster (E_{SC}),

$$R_9 = \frac{E_{3\times3}}{E_{SC}}. \tag{4.1}$$

This quantifies the lateral spread of energy from an electromagnetic shower. Figure 4.4 shows the R_9 distribution of the data sample before applying photon identification requirements. Photons that convert earlier are more likely to have a lower R_9 value than photons that make it all the way to the ECAL. A photon candidate with an R_9 close to 1 would suggest an unconverted photon.

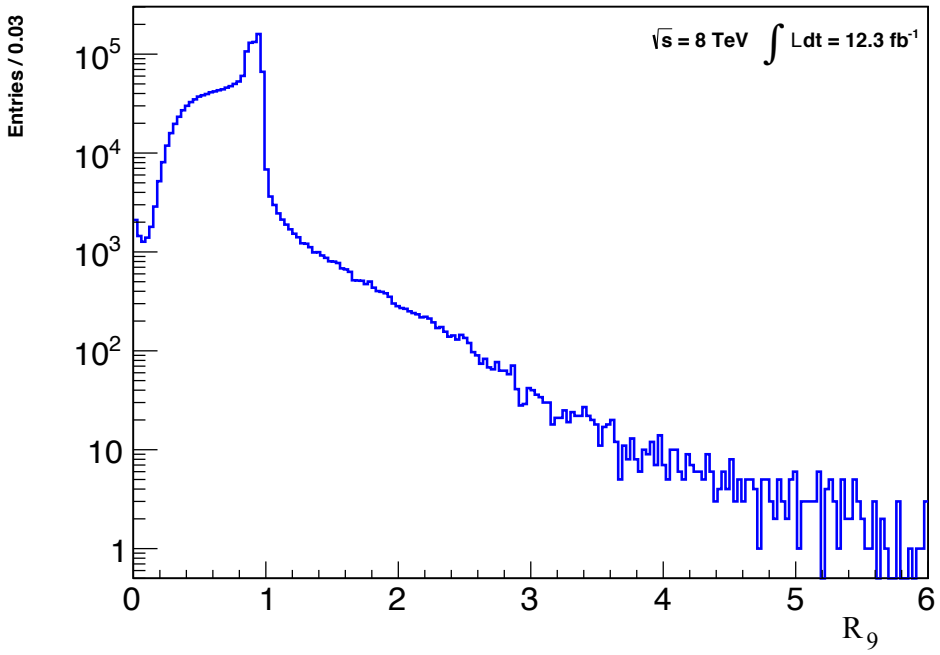

Figure 4.4: The R_9 distribution of the data sample before applying photon identification requirements.

Candidate photons are required to have $R_9 > 0$. The requirement of $R_9 > 0$ eliminates some nonphysical signals generated from malfunctioning electronics.

Calorimetric energy deposition ratio (H/E). The variable H/E is defined as the ratio of the energy of the single HCAL tower located behind the ECAL supercluster seed crystal to the total supercluster energy. This quantifies the radial distribution of energy deposited from the interaction point. While it is effective at removing neutral hadrons from the data sample, the selection criteria is also useful in discriminating between charged hadrons and photons since the bulk of the energy from a photon will be deposited in the ECAL. Figure 4.5 shows the H/E distribution of the data sample before applying photon identification requirements.

Energy weighted η-width ($\sigma_{i\eta i\eta}$). The transverse η spread of the shower shape is described by $\sigma_{i\eta i\eta}$, effectively the weighted variance in η of the crystals surrounding the supercluster seed

$$\sigma^2_{i\eta i\eta} = \frac{\sum\limits_{5\times5} w_i(\bar{\eta} - \eta_i)^2}{\sum\limits_{5\times5} w_i} \qquad w_i = \max\left(0, w_0 + ln\left(\frac{E_i}{E_{5\times5}}\right)\right), \tag{4.2}$$

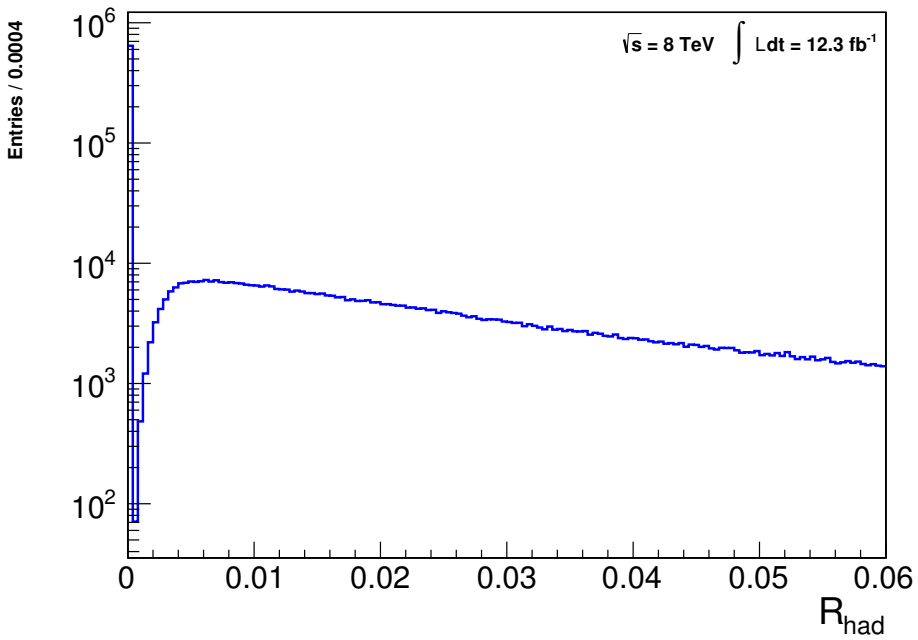

Figure 4.5: Distribution of $R_{\text{had}} = H/E$ for the data sample before applying photon identification requirements.

where $\bar{\eta}$ is the energy weighted mean of eta of the central 25 crystals and E_i and η_i are the energy and relative η position of the ith crystal respectively. $E_{5\times5}$ is the total energy in a region of the same 25 crystals (five rows by five columns). The optimizable constant w_0 for CMS is 4.2 [59]. The $\sigma_{i\eta i\eta}$ variable is useful in discriminating between prompt photons and photon-like jets. These jets can have hadronic decays that result in electromagnetic components mimicking that of a photon from the interaction point. The longitudinal width of the jets has a wider distribution in $\sigma_{i\eta i\eta}$ than the narrower distribution from prompt photons so the cut on this variable reduces jet contributions as shown through Monte Carlo simulation software. The distribution of $\sigma_{i\eta i\eta}$ before applying photon identification requirements is shown in Fig. 4.6.

4.4.2 Isolation variables

The CMS Particle Flow (PF) algorithm attempts to identify and reconstruct particles using a combination of the information from all the subdetectors [60, 61, 62] . The three PF isolation variables in Table 4.4 are calculated by summing the p_T of all PF candidates of the particular type (charged hadrons, neutral hadrons, photon) within a cone of radius $R = 0.3$ where $R =$

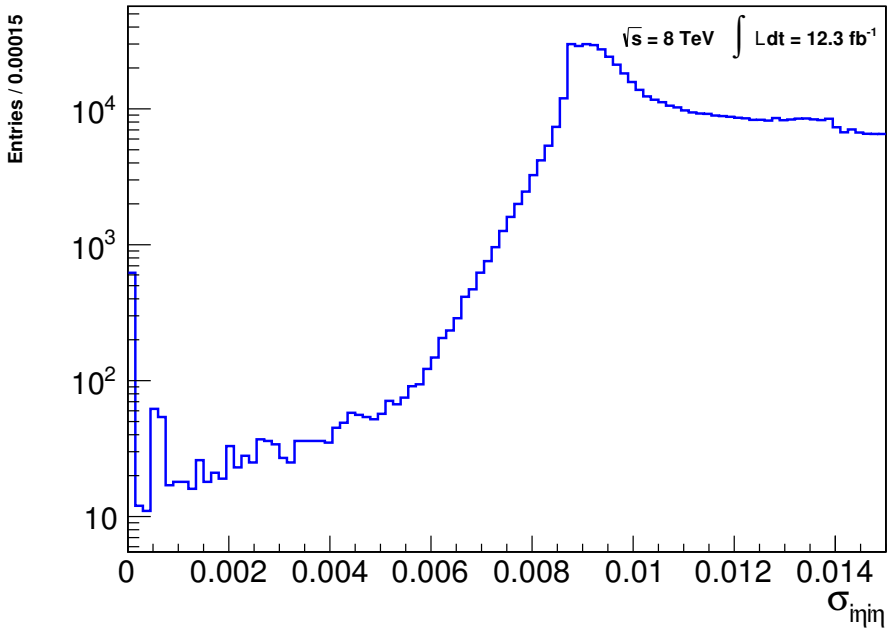

Figure 4.6: The $\sigma_{i\eta i\eta}$ distribution of the data sample before applying photon identification requirements.

$\sqrt{\Delta\eta^2 + \Delta\phi^2}$. This sum excludes the momentum of the candidate by either subtraction of an identified matching PF particle or by geometric vetoes where a match is not found in the PF collection.

The sum p_T calculated by the PF isolation cones is corrected for their contamination by energy deposits from the underlying event. To characterize the underlying event, the CMS software (CMSSW) uses an average event energy density (ρ). CMSSW calculates ρ on an event-by-event basis as the median of the distribution of transverse momentum of jets per area (P_t/A) [63]. This pileup correction is done by subtracting the product of ρ times an effective area (EA) based on η as shown in Table 4.5. Figure 4.7 shows the ρ of the data sample before applying photon identification requirements.

$$\text{CorrectedPFIso} = \text{PFIso} - \rho \cdot \text{EA} \tag{4.3}$$

EA is found using Monte Carlo simulated events with photons and jets while averaging the pileup effect by η bin and particle type.

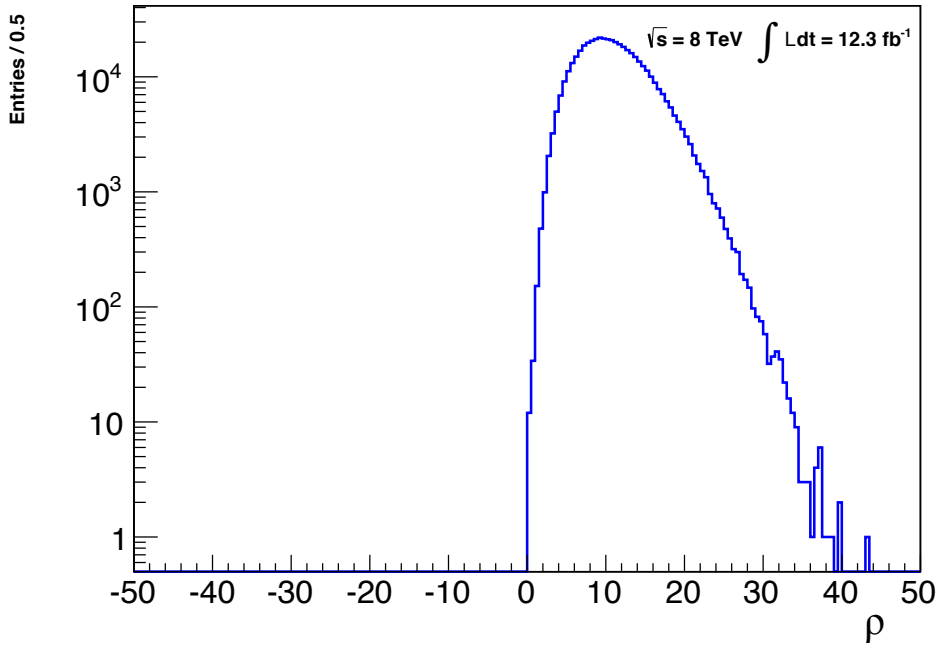

Figure 4.7: The ρ distribution of the data sample before applying photon identification requirements.

Table 4.5: Effective Area used in the isolation calculation for different regions within the CMS barrel.

Bin	EA charged hadrons	EA neutral hadrons	EA photon
$\lvert\eta\rvert < 1$	0.012	0.030	0.148
$1 < \lvert\eta\rvert < 1.479$	0.010	0.057	0.130

The ρ corrected distributions of charged, neutral, and photon isolations before applying photon identification requirements are shown in Figs. 4.8a, 4.8b, and 4.8c, respectively.

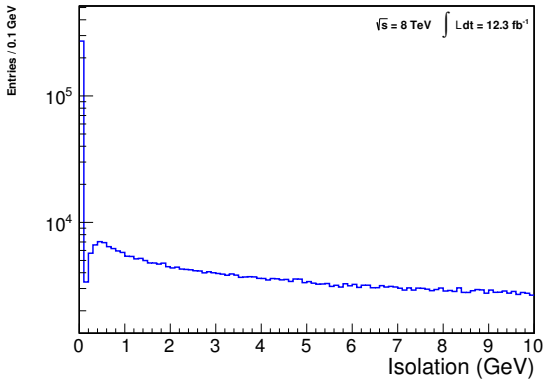

(a) Charged hadron isolation.

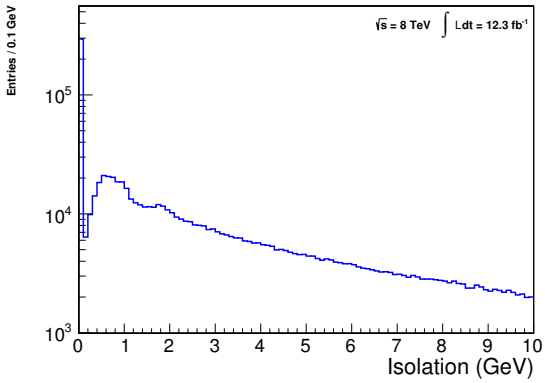

(b) Neutral hadron isolation.

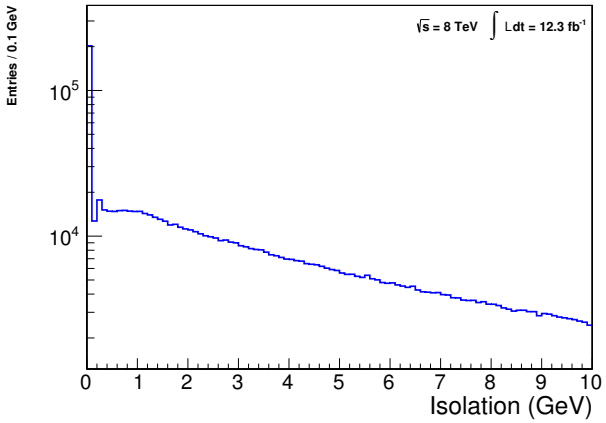

(c) photon isolation.

Figure 4.8: The separation of each photon from other particles. The ρ corrected charged hadron isolation, neutral hadron isolation, and photon isolation of the data sample are shown before applying the photon identification requirements.

4.4.3 Conversion safe electron veto

Since electrons and photons can behave very similarly in the ECAL, additional information is used from the tracker to determine if the source of the supercluster was a charged particle. A check is also performed to see if the track hits were caused by a converted photon to ensure these photons are included in the PF photon collection. If a converted photon is suspected, a further check is

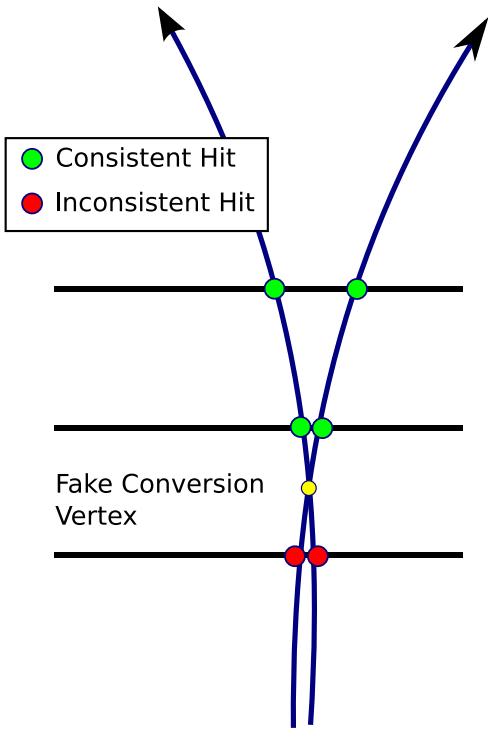

Figure 4.9: Schematic of how a random pairing of electrons could lead to a misidentified Bremsstrahlung conversion. The green dots are signals in the tracker that are consistent with a photon that converted at the location of the yellow dot. The red dots are tracker signals inconsistent with a converted photon.

done to see if there were tracker hits before the supposed conversion vertex. This is to eliminate incorrect pairings of e^+e^- which coincidentally appear as a converted photon as in Fig. 4.9.

The electron reconstruction models the effect of bremsstrahlung energy loss on track parameters using a Gaussian-sum-filter (Gsf) [64]. The Gsf algorithm models the bremsstrahlung energy loss distribution by a Gaussian mixture rather than by a single Gaussian. Therefore a supercluster is rejected if it matches a Gsf electron with no missing hits in the inner layer of the tracker and also fails to match a reconstructed photon conversion.

4.5 Preselection

This analysis made very simple cuts on the datasets listed in Table 4.1 to remove unrelated events before applying photon identification requirements.

Each event was required to have at least three objects in the reco-photon collection as categorized by the reconstruction algorithm, referred to as the reco-photon collection subsequently in this analysis. Many of the objects in the reco-photon collection are not photons but are other objects, to minimize real photons being rejected. Electrons and jets with a large electromagnetic component will be included and must be filtered by cutting on appropriate discriminating variables.

Prior to selection the data are reduced in size by only keeping partial information for each event. This reduces each event size from $\approx 1\,\mathrm{MB}$ to a more manageable few kB.

CHAPTER 5

ANALYSIS

The central parameter of interest for this analysis is the diphoton invariant mass where the signal will appear as a narrow peak. Except for this narrow peak, the data are expected to be slowly varying over the region of interest (200-600 GeV). Therefore, the data are analyzed by fitting to a smooth background function plus a narrow resonance.

5.1 Selection

5.1.1 Three photon candidate events

Candidate events are those that have three photons in the final state. The minimum requirement is that the photons are reconstructed as part of the reco-photon collection. However, these candidate photons also include electrons and some photon-like jets. Additional requirements are applied to reduce contamination while maintaining a high acceptance and efficiency for real photons.

All photon candidates are required to pass the "conversion safe electron veto" which removes candidates with reconstructed tracks or tracker hits that are not consistent with $\gamma \to ee$ conversions. The photon p_{T} must be greater than 20 GeV. The requirements of Section 4.4 and Table 4.4 are applied to create the loose/medium/tight photon collections. Photons must lie within the barrel ($|\eta| < 1.44$, where η is measured with respect to the detector center rather than the reconstructed vertex) except in the case of reco-photons.

Different combinations of reco, loose, medium, and tight photons were considered for the final selection. Table 5.1 lists the numbers of signal events passing various combinations for three different $\tilde{\pi}$ masses.

The final selection is chosen to accept events that have either three loose photons or two loose photons plus an additional reco-photon. This maintains a greater than 80% efficiency for signal events (Table 5.2). The table does not account for the branching fractions from the signal model. It also retains a sufficient sample size to accommodate a narrow resonance search with a smooth background in the data (Table 5.3).

Table 5.1: Number of events passing various photon criteria for selected signal MC. The criteria for selection are described in Section 5.1.1

Category	$M(\tilde{\pi}) = 200$ GeV	$M(\tilde{\pi}) = 400$ GeV	$M(\tilde{\pi}) = 600$ GeV
events generated	9997	9500	5355
3 reco	9412	9145	5212
1 loose + 2 reco	9290	9035	5182
2 loose + 1 reco	8206	7885	4732
2 medium + 1 reco	7755	7504	4527
2 tight + 1 reco	6936	6712	4120
3 loose	4580	4099	2687
1 medium + 2 loose	4578	4099	2686
2 medium + 1 loose	4540	4071	2671
3 medium	3838	3476	2347
2 tight + 1 medium	3713	3381	2295
3 tight	2888	2659	1861

Table 5.2: Numbers of events and acceptance $\times$ efficiency of signal MC for generated mass points for final event selection. The table does not account for the branching fractions from the signal model. The criteria for selection are described in Section 5.1.1

Generated Resonant Mass [GeV]	Number of Events Generated	Number of Selected Events	Acceptance $\times$ Efficiency
200	9997	8206	0.82
225	5457	4572	0.84
250	9996	8358	0.84
275	5565	4732	0.85
300	8500	7160	0.84
320	7998	6743	0.84
340	9000	7548	0.84
360	8500	7115	0.84
380	9799	8162	0.83
400	9500	7885	0.83
420	8499	6974	0.82
450	5541	4611	0.83
500	5373	4476	0.83
550	5289	4560	0.86
600	5355	4732	0.88

Table 5.3: Number of events passing various photon criteria for selected data. The criteria for selection are described in Sec. 5.1.1

Category	number of events
preselection	856966
3 reco	468066
1 loose + 2 reco	83215
2 loose + 1 reco	7399
2 medium + 1 reco	5083
2 tight + 1 reco	3726
3 loose	143
1 medium + 2 loose	143
2 medium + 1 loose	130
3 medium	82
2 tight + 1 medium	73
3 tight	57

Table 5.4: Selection criteria for events to be included in the final sample.

Photon passes conversion safe electron veto
Photon p_{T} >20 GeV
Loose/medium/tight photons must be in ECAL barrel
$\geq$ 3 loose photons or 2 loose + $\geq$ 1 additional RECO-PHOTON

The final selection criteria are summarized in Table 5.4.

5.2 Distributions

The possible selection criteria categories (Table 5.3) rapidly reduce the number of events as the categories become more restrictive and is apparent in the distributions of most variables. For example, the distributions of E_T for photons in the 2 loose and one reco-photon or the 3 loose selection (Fig. 5.1) extends into the 600 GeV range while the same distribution in the 3 loose selection goes to zero by 250 GeV (Fig. 5.2). The distribution of E_T for the highest energy photon in each event in the 2 loose and one reco-photon or the 3 loose selection are shown in Fig. 5.3. The same distribution in the 3 loose selection makes the data discrepancy more apparent (Fig. 5.4).

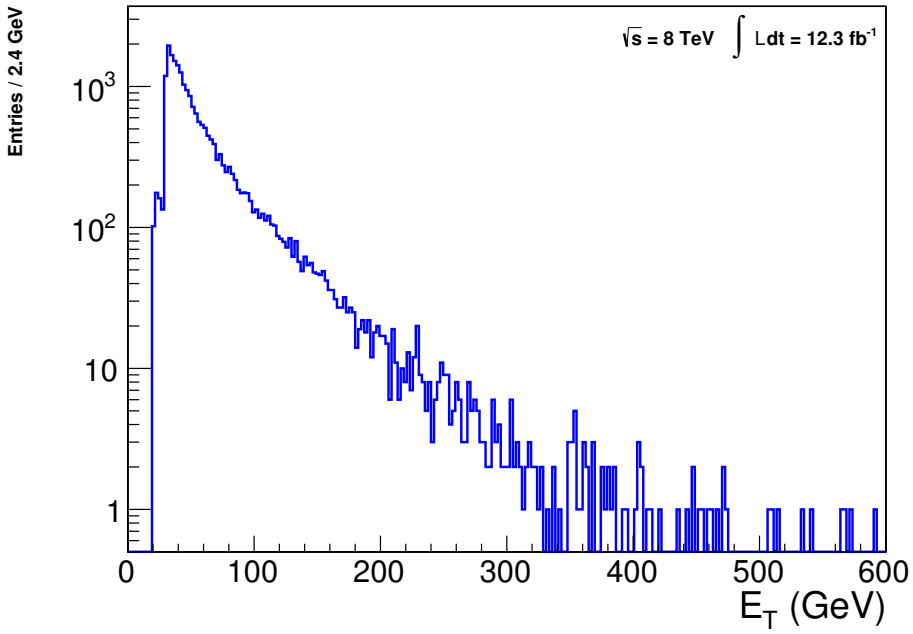

Figure 5.1: Distribution of transverse energy of all photons in data for events passing the two loose and one reco-photon or the three loose selection criteria.

Focusing on the final data selection (2 loose and one reco-photon or 3 loose), the distributions in relevant variables are shown in the following section. Distributions of the number of photons, η, ϕ, R_9, ρ, $\sigma_{i\eta i\eta}$, H/E, and isolation variables for the final data selection are shown in Figs. 5.5-5.12.

The y-axis on Fig. 5.5 is logarithmic, and the number of events with greater than three reconstructed photons drops by almost an order of magnitude with each additional photon. The distributions in η and ϕ (Figs. 5.6 and 5.7) show standard distributions with small statistical fluctuations.

The distribution in R_9 has a sharp drop around $R_9 = 1$ consistent with the variable definition from Eq. 4.1. The distribution in ρ has little change from preselection. The variables $\sigma_{i\eta i\eta}$ and isolation variables show an expected drop around their respective selection conditions.

A better understanding of the the impact of individual selection criteria is obtained by examining the result of applying all selection criteria except the one under consideration. Distributions of a variable shown applying all selection criteria except the plotted variable will be called "exclusion distributions" in this analysis. For example, in Fig. 5.13 the exclusion distribution of $\sigma_{i\eta i\eta}$ is shown after all selection criteria except $\sigma_{i\eta i\eta} < 0.012$ are applied (black) as well as the distribution of $\sigma_{i\eta i\eta}$

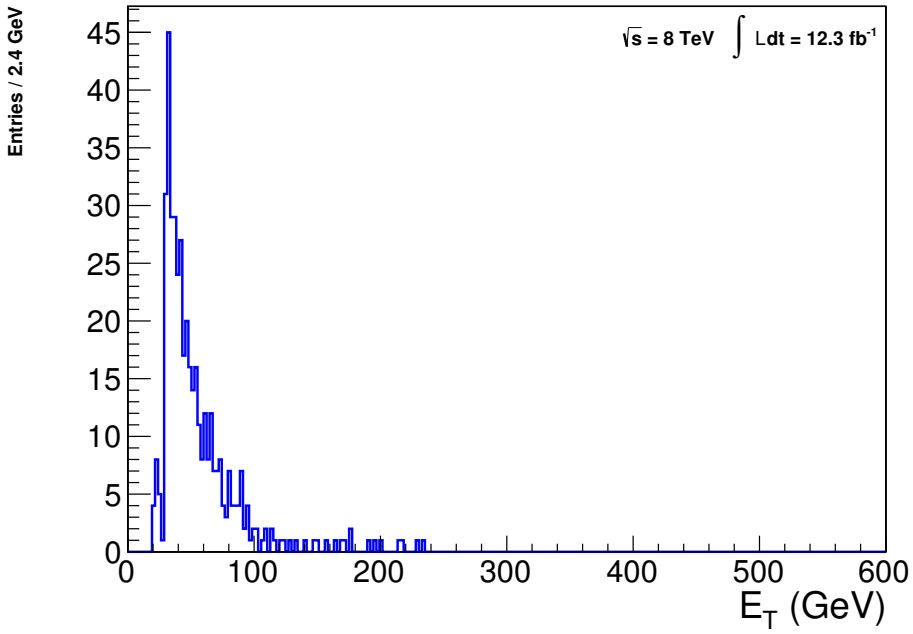

Figure 5.2: Distribution of transverse energy of all photons in data for events passing the three or more loose photon selection criteria.

after all criteria are applied (blue). The effect of selection criteria are considered on the two loose and one reco-photon selection or three loose photon selection that are the focus of this analysis.

Analogous exclusion distributions are shown for H/E (Fig. 5.14), charged hadron isolation (Fig. 5.15), neutral hadron isolation (Fig. 5.16), and photon isolation (Fig. 5.17).

5.3 Invariant mass

For each event, the three candidate photons are chosen as either (1) the three highest p_{T} loose photons or (2) the two loose photons and the highest p_{T} reco-photon that is not a loose photon. The invariant mass is constructed for every two photon combination of these three candidate photons in an event passing the selection criteria (see Section 5.1) for both data and Monte Carlo simulation of signal.

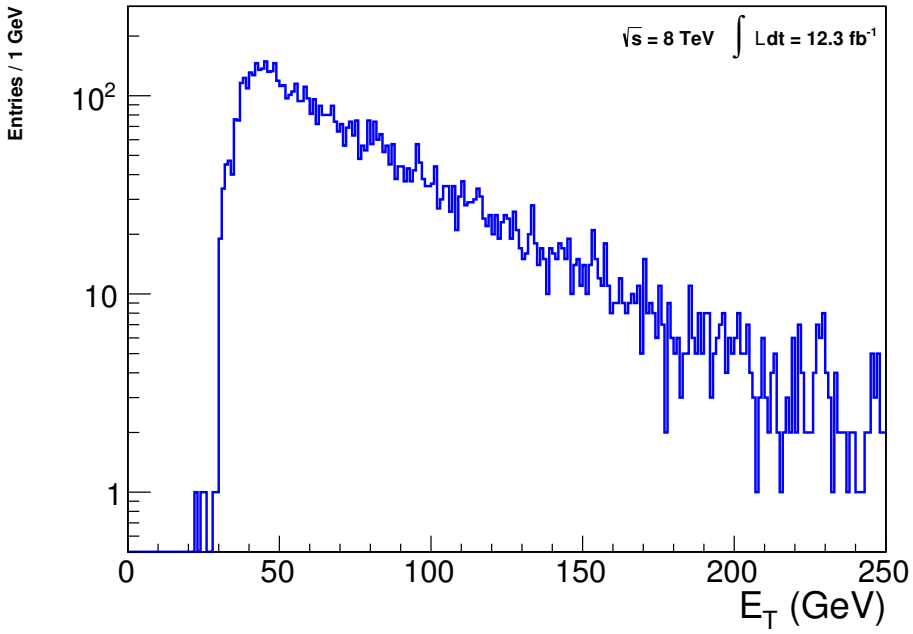

Figure 5.3: Distribution of transverse energy of reconstructed photons in data for the leading (highest energy) photon in events passing the two loose and one reco-photon or the 3 loose selection criteria.

From the reconstructed ϕ, η, and transverse energy E_T of each photon, the momentum in three space (p_x, p_y, p_z) is

$$p_x = E_T \cos(\phi) \tag{5.1}$$

$$p_y = E_T \sin(\phi) \tag{5.2}$$

$$\theta = 2 \arctan\left(e^{-\eta}\right) \tag{5.3}$$

$$p_z = E_T \frac{\cos(\theta)}{\sin(\theta)}. \tag{5.4}$$

For two given photons ,"A" and "B", the pairwise invariant mass (m_{AB}) is found using the typical four vector algebra,

$$m_{AB}^2 = (E_A + E_B)^2 - (\mathbf{p}_A + \mathbf{p}_B)^2 \tag{5.5}$$

$$= m_A^2 + m_B^2 + 2(E_A\, E_B - \mathbf{p}_A \cdot \mathbf{p}_B) \tag{5.6}$$

$$= 2(E_A\, E_B - \mathbf{p}_A \cdot \mathbf{p}_B) \tag{5.7}$$

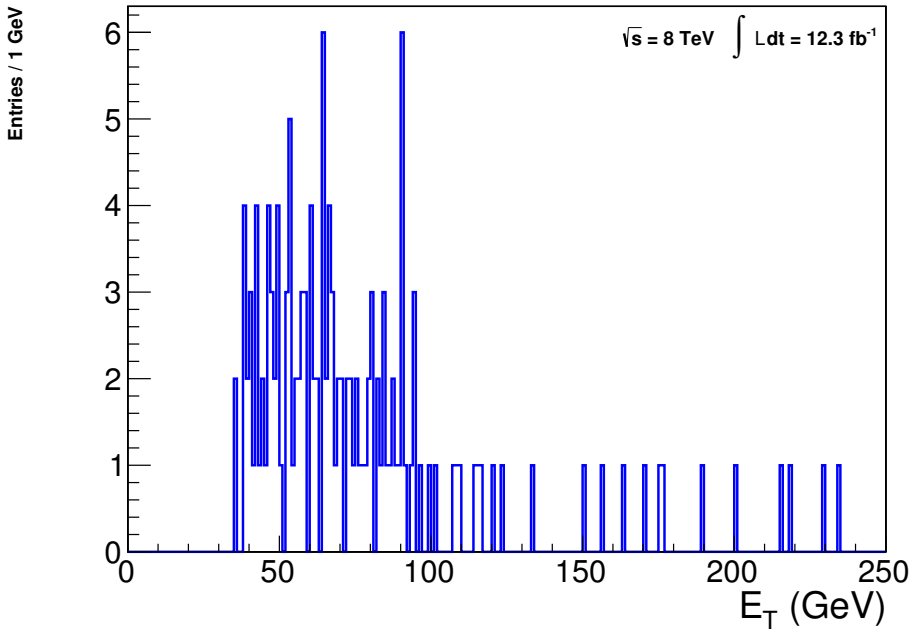

Figure 5.4: Distribution of transverse energy of reconstructed photons in data for the leading (highest energy) photon in events passing the three or more loose photon data selection criteria.

since photons are massless. In addition to the pairwise invariant mass, a second interesting variable is the total three photon invariant mass,

$$m^2_{ABC} = 2\left(E_A\,E_B + E_A\,E_C + E_B\,E_C - \mathbf{p}_A\cdot\mathbf{p}_B - \mathbf{p}_A\cdot\mathbf{p}_C - \mathbf{p}_B\cdot\mathbf{p}_C\right). \tag{5.8}$$

Figures 5.18, 5.19, and 5.20 show the pairwise invariant mass for the three reco-photon, two loose plus one reco-photon, and three loose photon samples respectively. Figure 5.19 will be the primary distribution of interest for the search. In each case, the distribution is generally smooth in the region of interest. The three photon invariant mass for the three reco-photon, two loose plus one reco-photon, and three loose photon samples are shown in Figs. 5.21, 5.22, and 5.23. No significant, narrow structure is observed. While not a signature of this model in particular, such a structure might be a sign of non-SM physics.

5.4 Signal simulation fitting

Monte Carlo simulation of signal processes are done for 15 invariant mass points from $200-600$ GeV. The tree level processes are simulated through the process of hadronization and detector

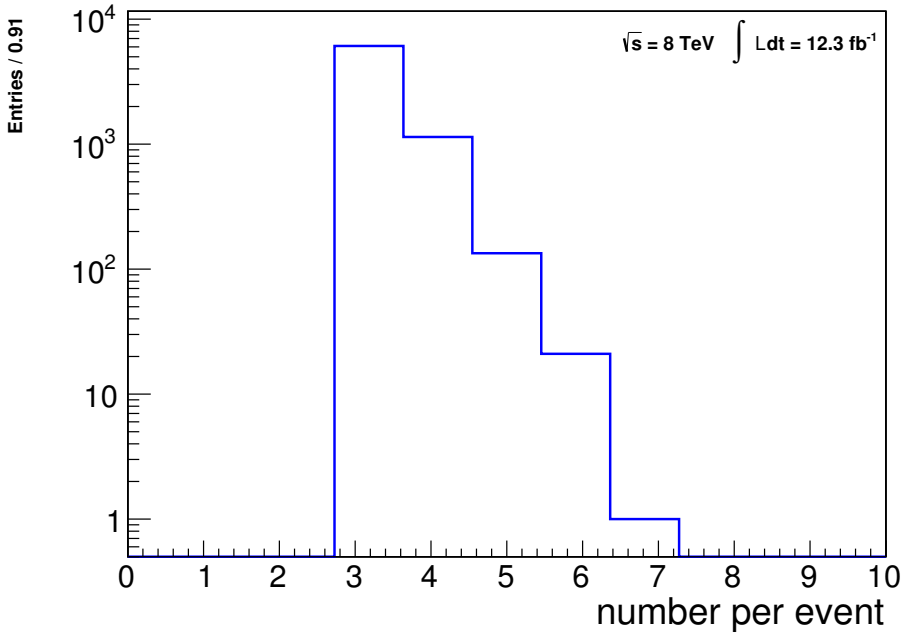

Figure 5.5: Distribution of the number of reconstructed photons for the final data sample.

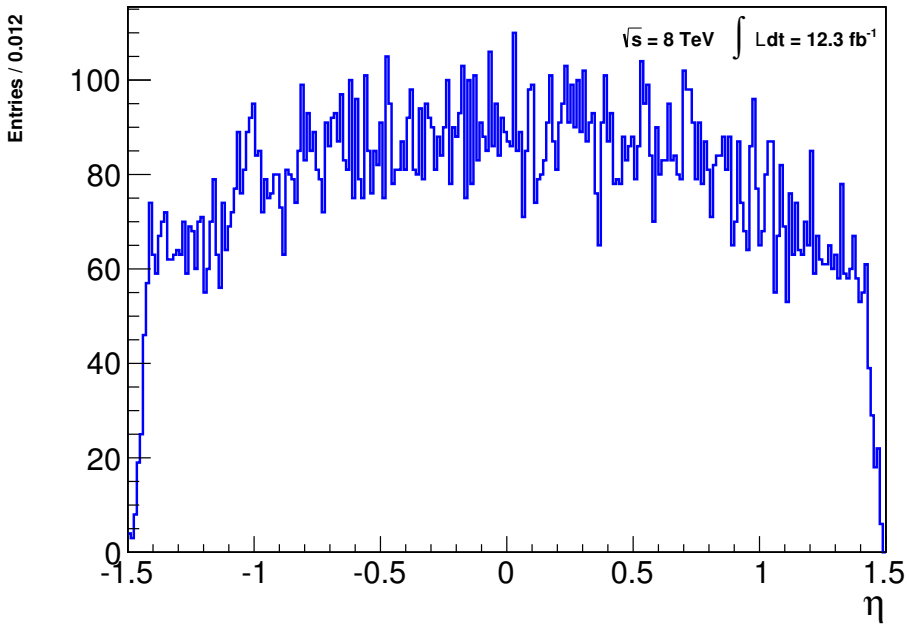

Figure 5.6: Distribution of η of reconstructed photons for the final data sample.

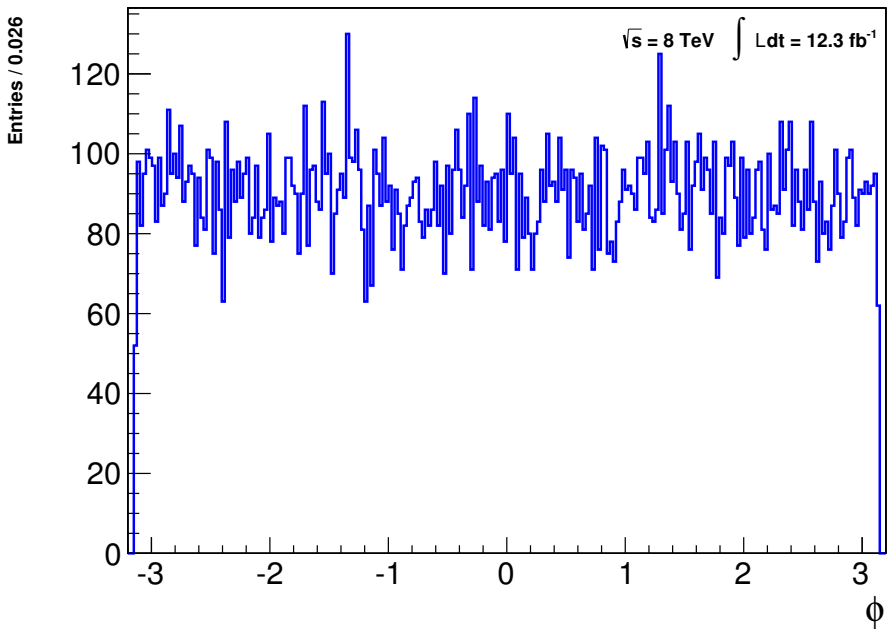

Figure 5.7: Distribution of ϕ of reconstructed photons for the final data sample.

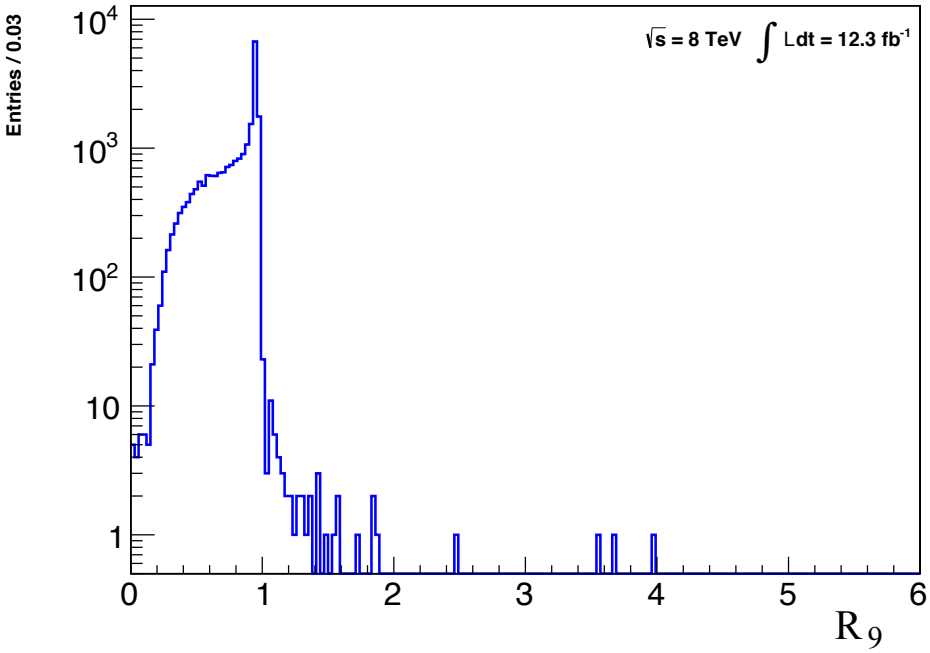

Figure 5.8: Distribution of R_9 for reconstructed photons for the final data sample.

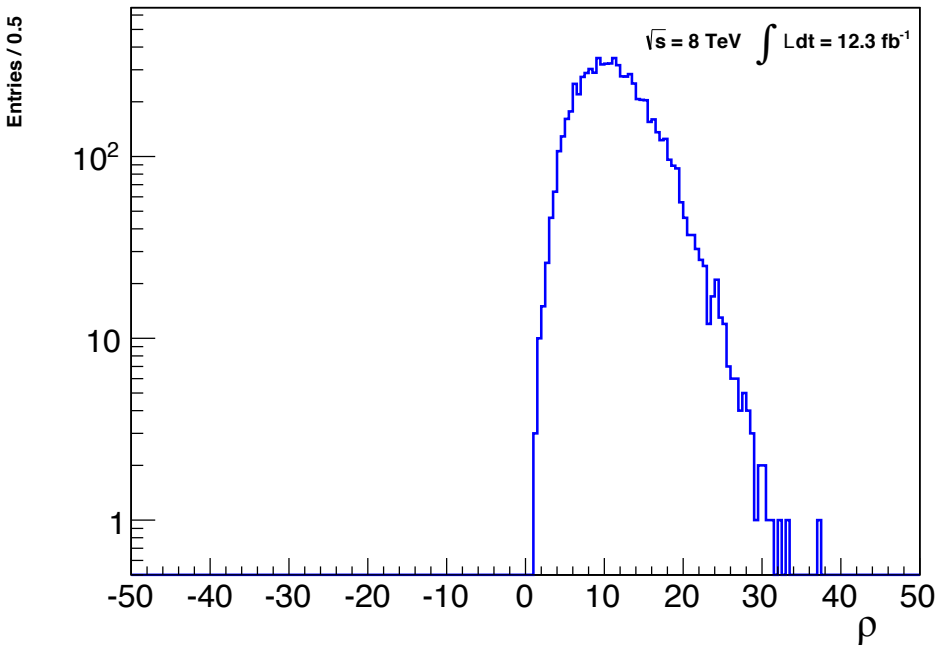

Figure 5.9: Distributions of average event energy density ρ for the final data selection. See Section 4.4.1 for definition.

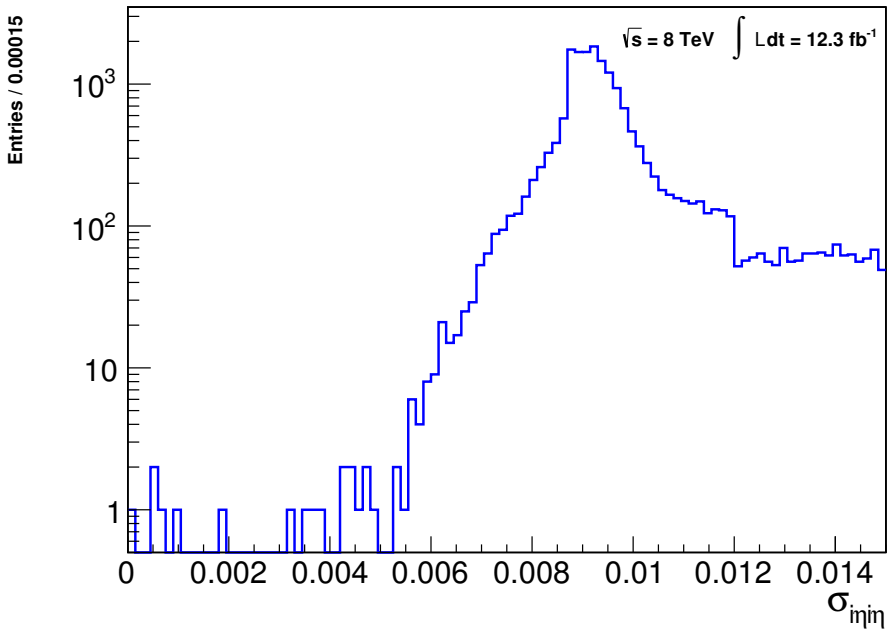

Figure 5.10: Distribution of $\sigma_{i\eta i\eta}$ for photons in the the final data sample. See Section 4.4.1 for definition.

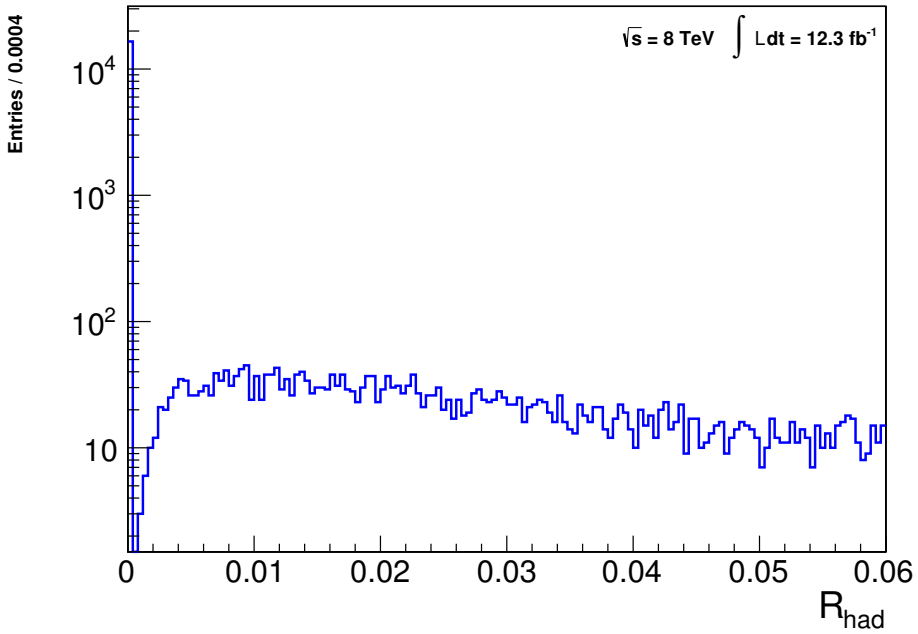

Figure 5.11: Distribution of H/E of the data sample for the final data selection. See Section 4.4.1 for definition.

interaction with CMSSW [57]. The simulated events are processed exactly the same as the collision data.

Figure 5.24 shows the ratio of number of signal entries passing selection criteria to the number generated at each mass point. This ratio is defined as the acceptance × efficiency (ϵ). A 2nd order polynomial fit is used to parameterize the efficiency. Table 5.5 lists the parameters of the fit. This parameterization is used to interpolate the efficiency as a function of the generated hyperpion mass ($200 < m(\gamma\gamma) < 600$ GeV).

Table 5.5: Parameters of the fit to the signal efficiency. The fit function is $p_2 m^2 + p_1 m + p_0$.

Parameter	Value
p_0	0.79 ± 0.03
p_1	-0.00026 ± 0.00014
p_2	$4.4 \times 10^{-7} \pm 1.8 \times 10^{-7}$

The branching ratio (BR) times cross section (σ) is given by

$$BR \cdot \sigma = \frac{N_{\text{sig}}}{\mathcal{L} \cdot \epsilon} \tag{5.9}$$

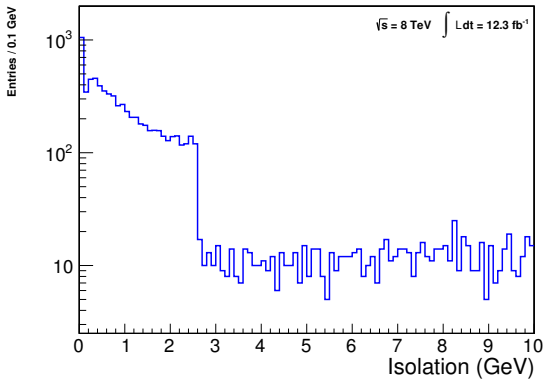

(a) Charged hadron isolation.

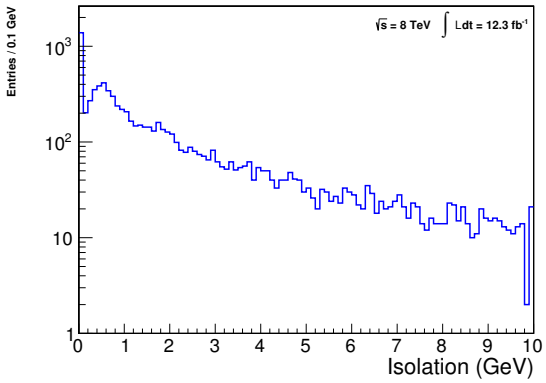

(b) Neutral hadron isolation.

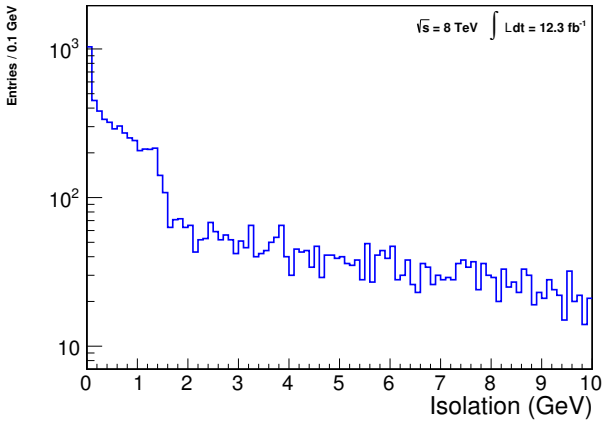

(c) photon isolation.

Figure 5.12: Distributions of isolation variables that quantify the separation of each photon from other particles of the final data selection. Charged hadron isolation (5.12a), neutral hadron isolation (5.12b), and photon isolation (5.12c) of the data sample are shown.

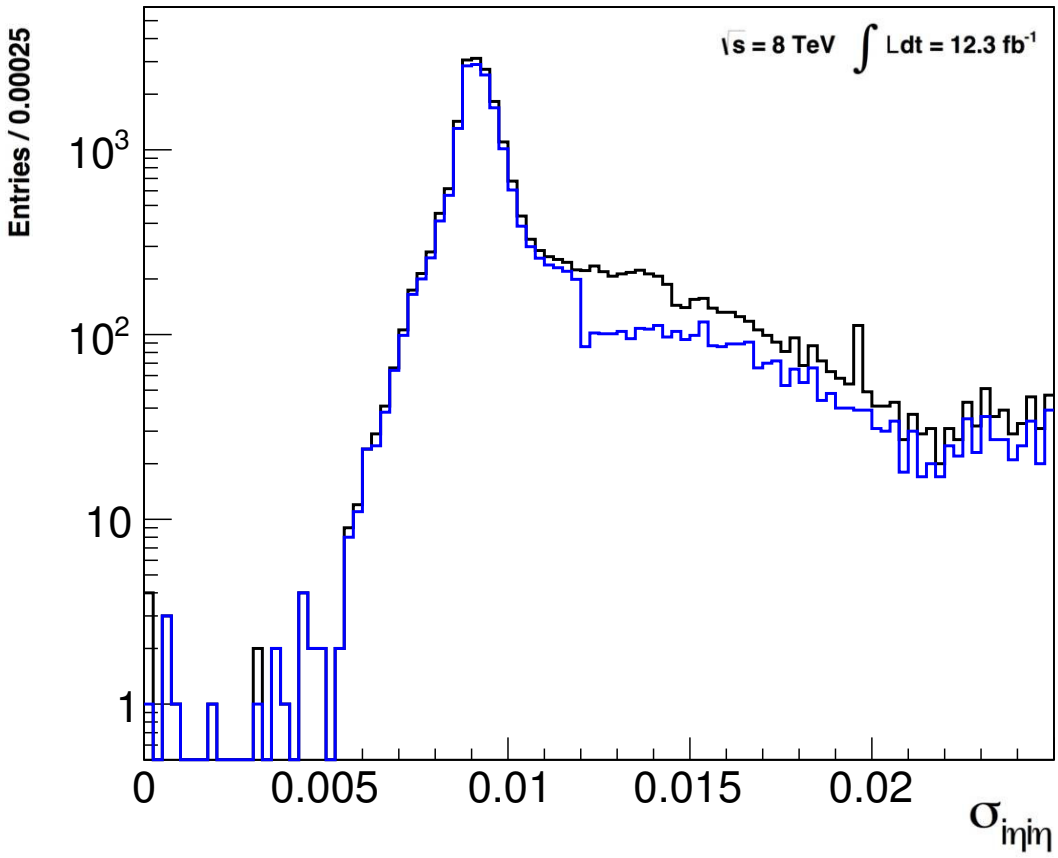

Figure 5.13: Exclusion distribution of $\sigma^2_{i\eta i\eta}$ of candidate events for the final data selection. The distribution of $\sigma^2_{i\eta i\eta}$ is shown after all selection criteria except $\sigma^2_{i\eta i\eta} < 0.012$ are applied (black) as well as the distribution of $\sigma^2_{i\eta i\eta}$ after all criteria are applied (blue).

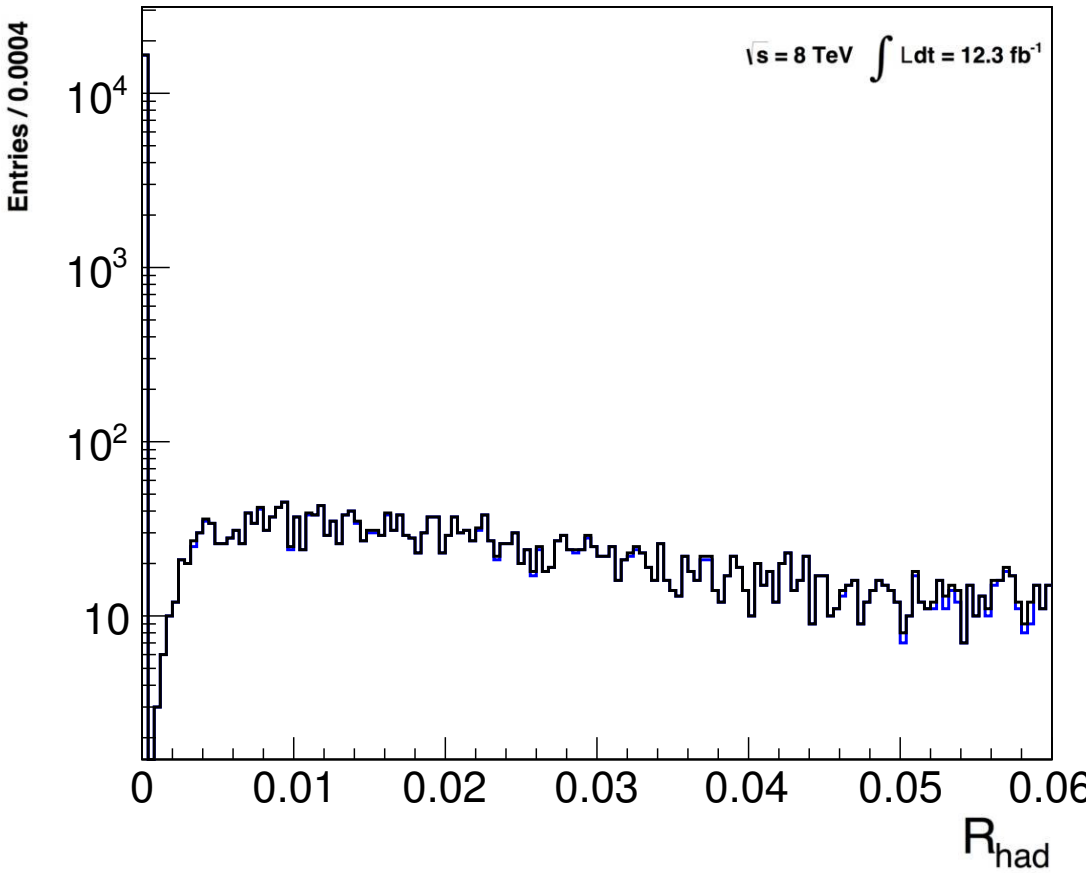

Figure 5.14: Exclusion distribution of H/E of candidate photons for the final data selection. The distribution of H/E is shown after all selection criteria except $H/E < 0.05$ are applied (black) as well as the distribution of H/E after all criteria are applied (blue).

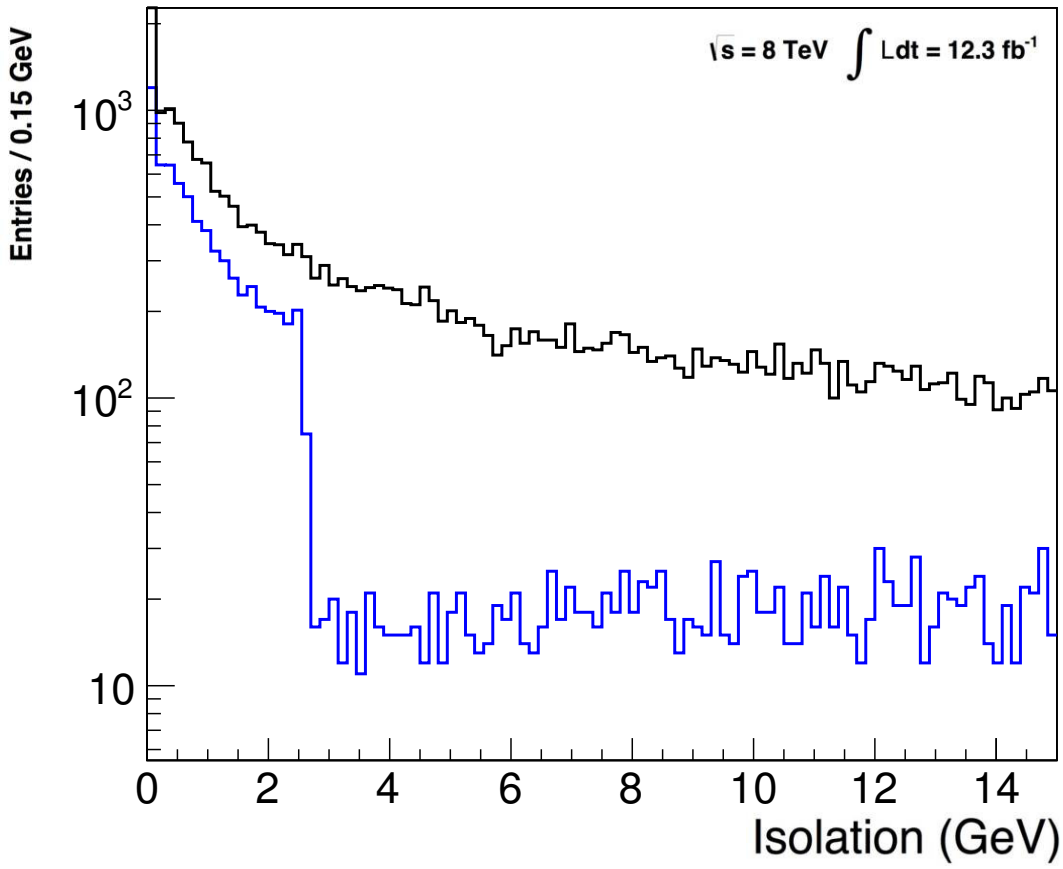

Figure 5.15: Exclusion distribution of charged hadron isolation of candidate photons for the final data selection. The distribution of charged hadron isolation is shown after all selection criteria except PF charged hadron isolation < 2.6 are applied (black) as well as the distribution of charged hadron isolation after all criteria are applied (blue).

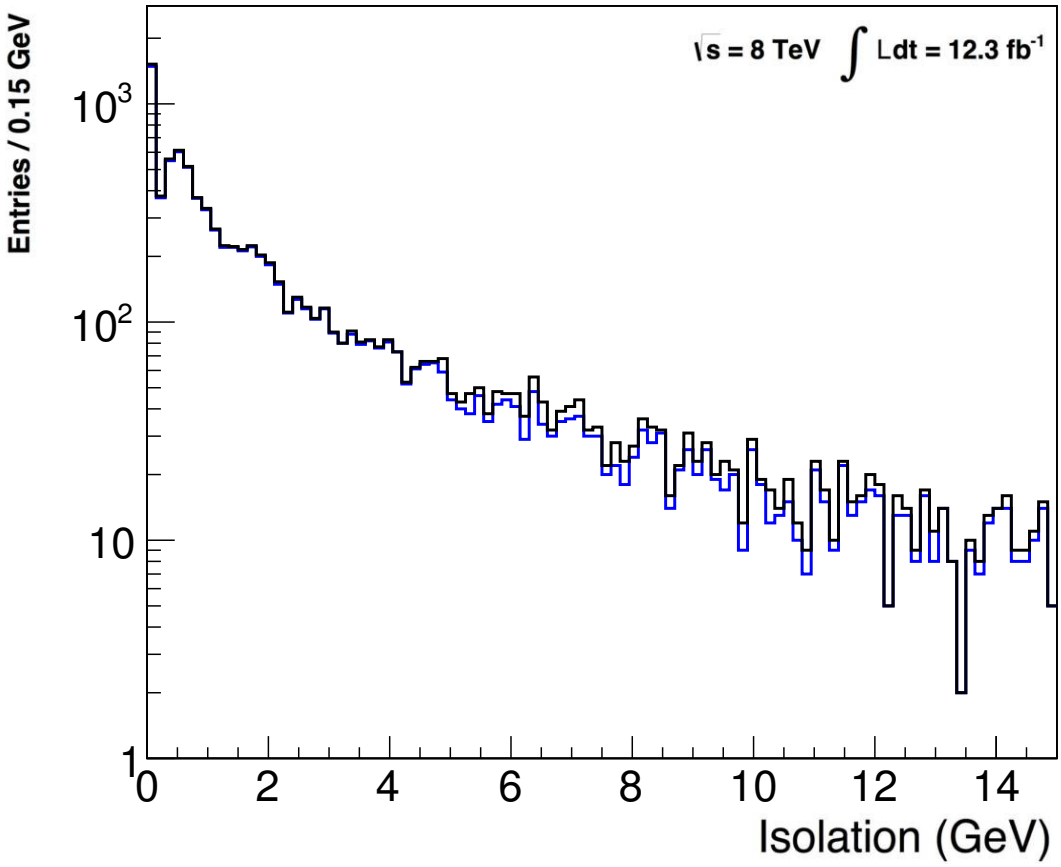

Figure 5.16: Exclusion distribution of neutral hadron isolation of candidate photons for the final data selection. The distribution of neutral hadron isolation is shown after all selection criteria except PF neutral hadron isolation $< 3.5 + 0.04 \cdot P_T^{\gamma}$ are applied (black) as well as the distribution of neutral hadron isolation after all criteria are applied (blue).

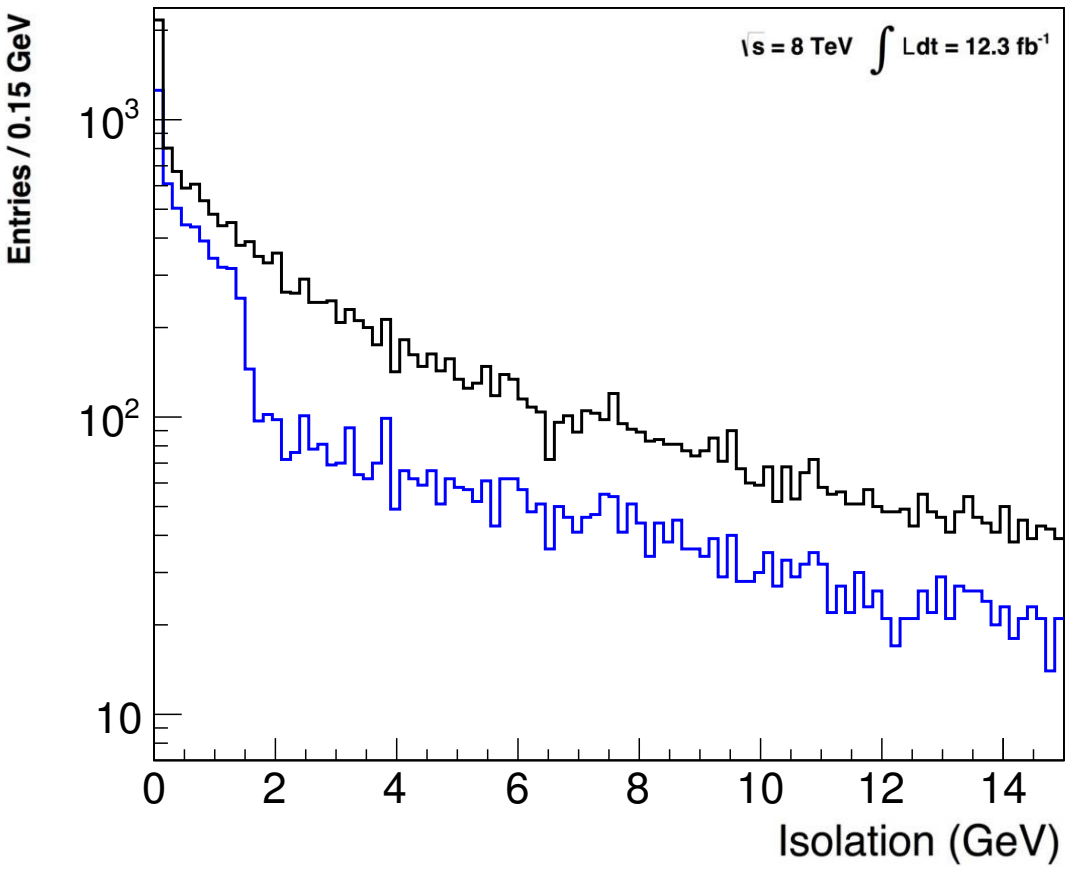

Figure 5.17: Exclusion distribution of photon isolation of candidate photons for the final data selection. The distribution of photon isolation is shown after all selection criteria except PF photon isolation $< 1.3 + 0.005 \cdot P_T^{\gamma}$ are applied (black) as well as the distribution of photon isolation after all criteria are applied (blue).

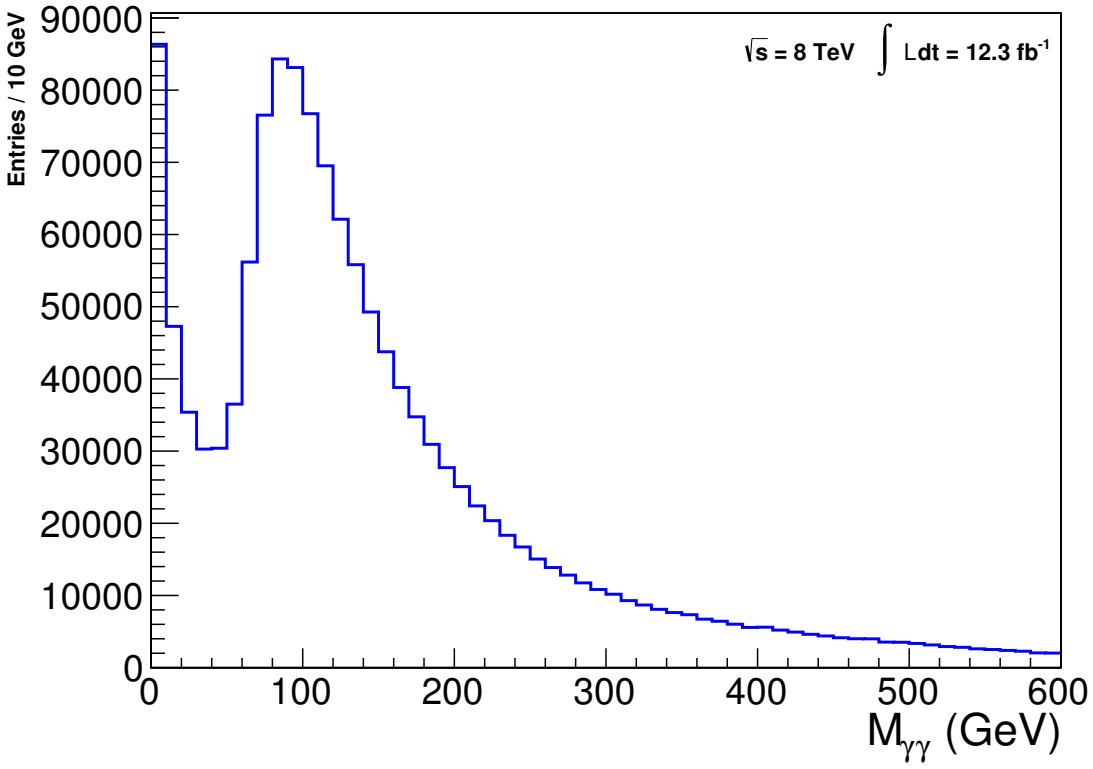

Figure 5.18: The pairwise invariant mass of all three combinations of the three candidate photons for events with three reco-photons.

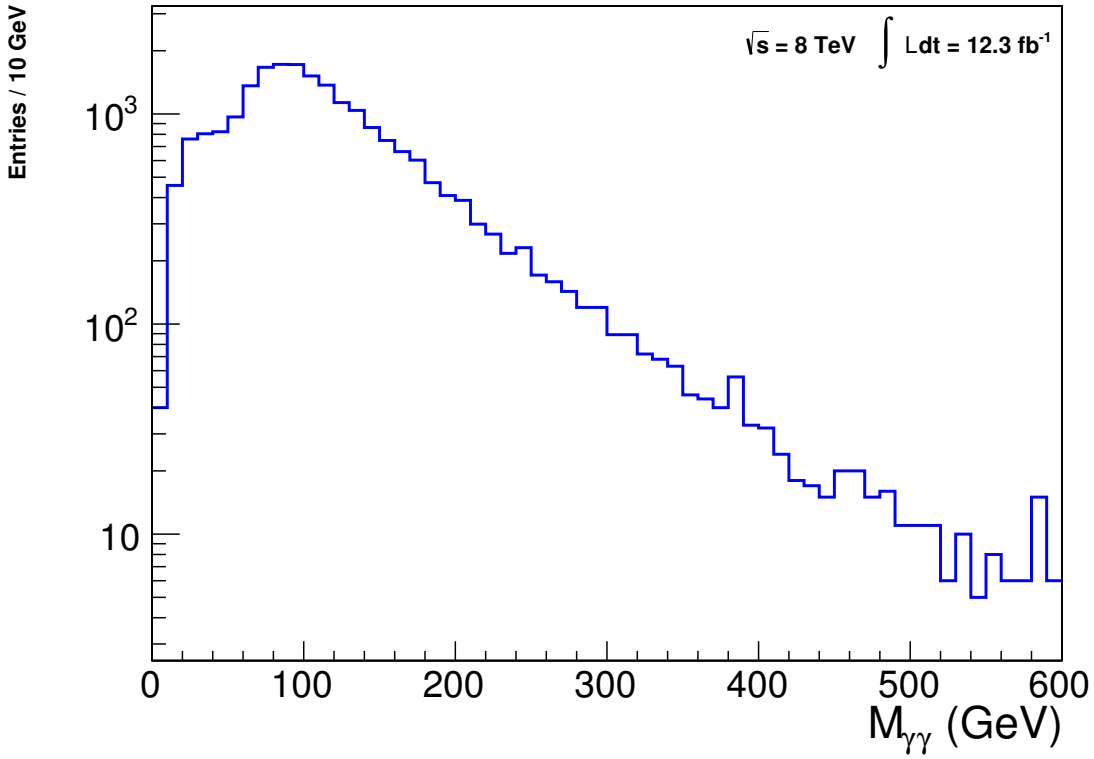

Figure 5.19: The pairwise invariant mass of all three combinations of the three candidate photons for events with two loose plus one reco-photon. This will be the primary distribution of interest for the search.

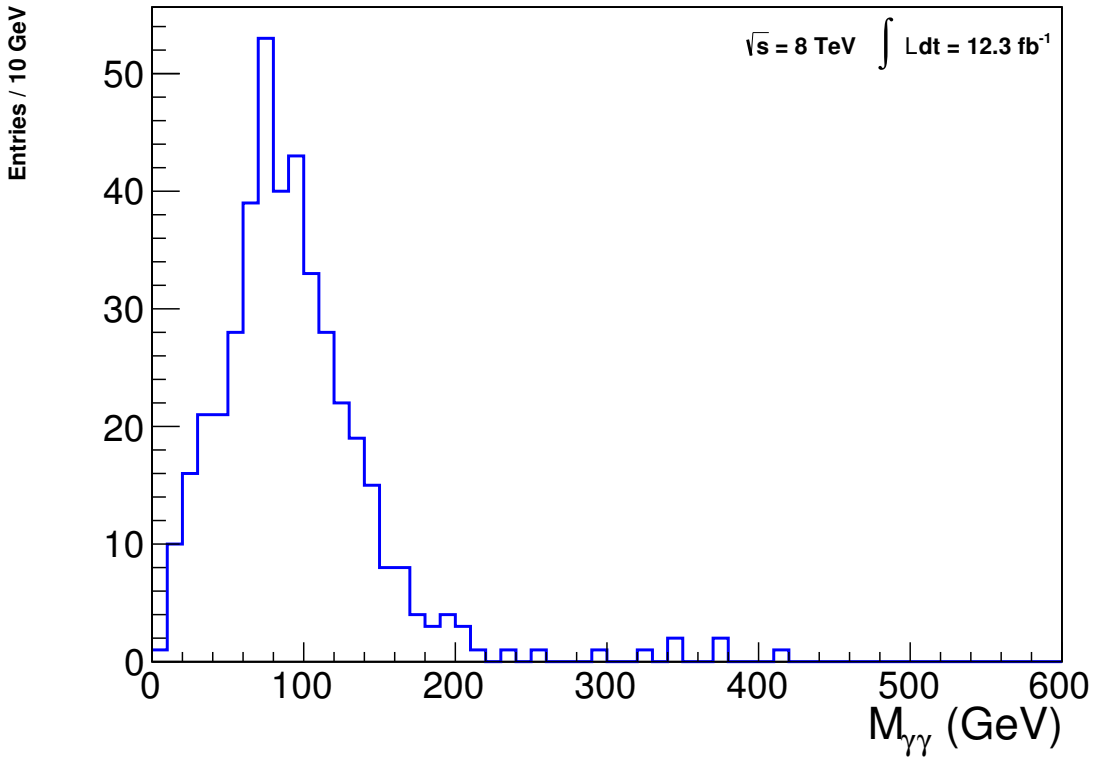

Figure 5.20: The pairwise invariant mass of all three combinations of the three candidate photons for events with three loose photons.

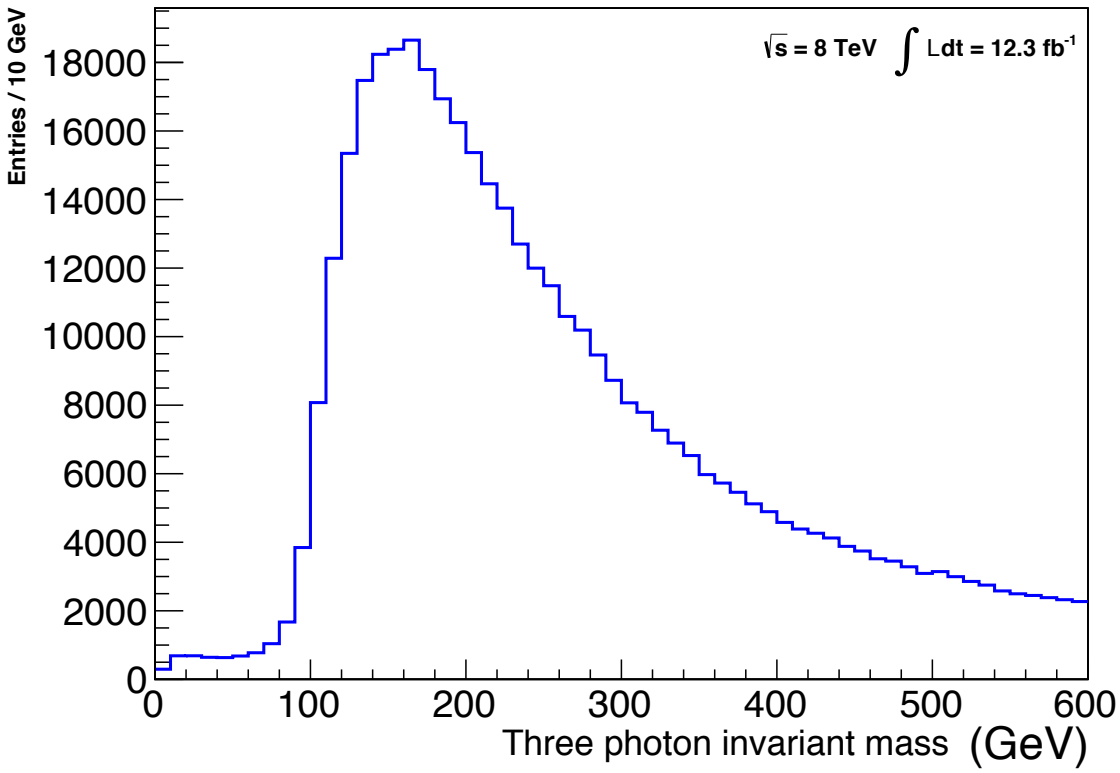

Figure 5.21: Distribution of the three photon invariant mass for events with three reco-photons.

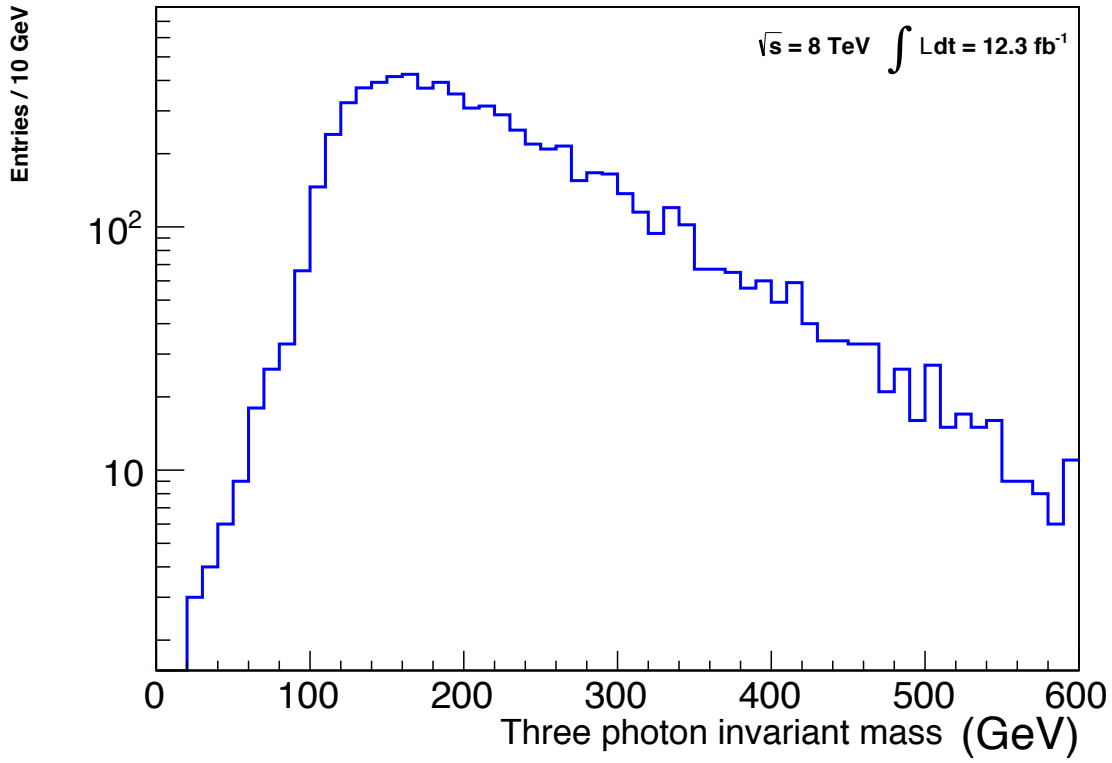

Figure 5.22: Distribution of the three photon invariant mass for events with two loose and one reco-photon.

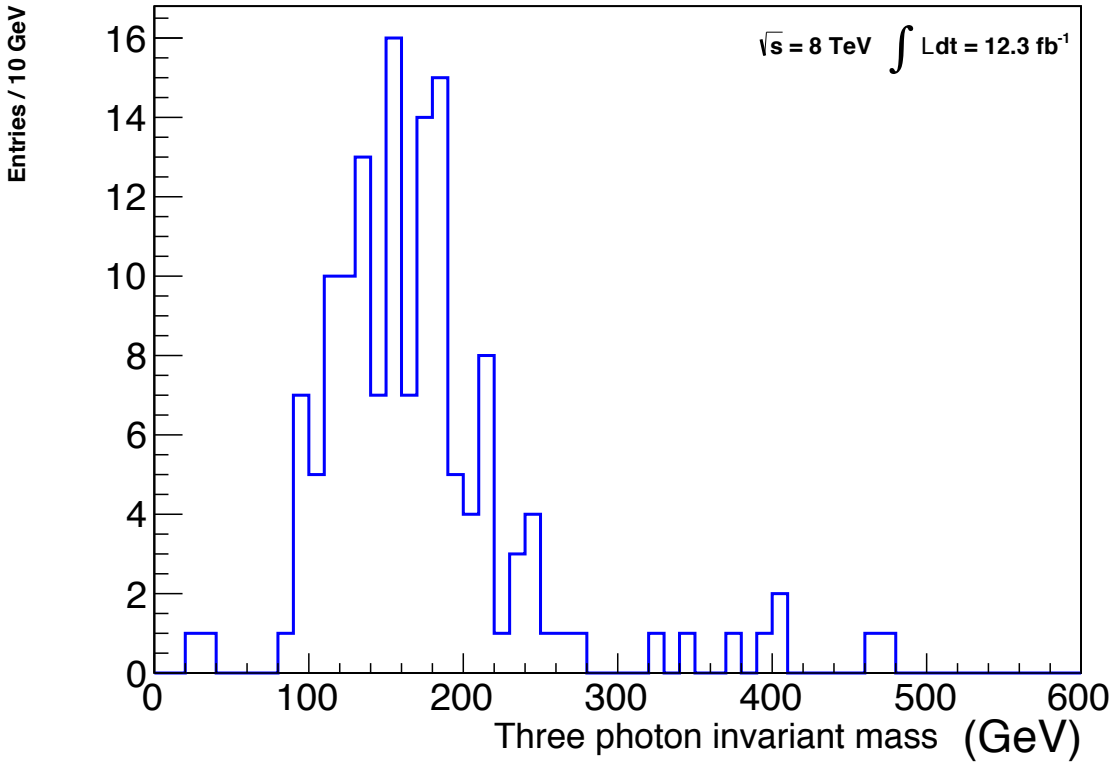

Figure 5.23: Distribution of the three photon invariant mass for events with three or more loose photons.

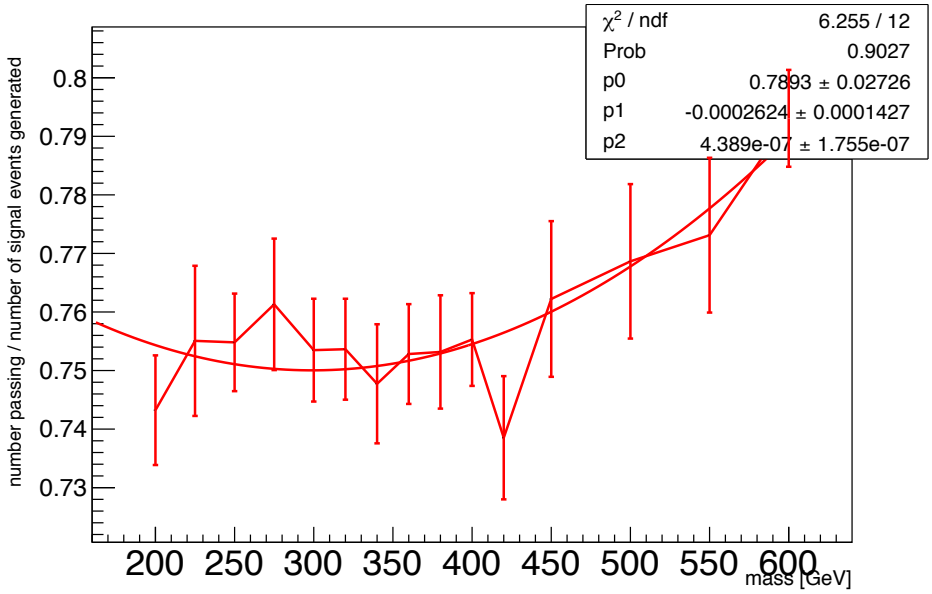

Figure 5.24: Ratio of number of signal entries passing selection criteria to the number generated at each mass point. A quadratic fit is used to interpolate to the mass points used to set the experimental limit of cross section times branching fraction.

where $\mathcal{L}$ is integrated luminosity and $N_{\rm sig}$ is the number of signal events observed.

The simulated invariant mass distributions of $\tilde{\pi}$ decay are fit with a polynomial plus Crystal Ball line shape:

$$N_{bkg}\left(a_2 m^2 + a_1 m + 1\right) + N_{sig} C(m; m_0, \sigma, \alpha, n), \tag{5.10}$$

where m is the diphoton invariant mass and a_1, and a_2 are the parameters of the 2nd order polynomial. The polynomial distribution accounts for mass combinations that arise from constructing the invariant mass with every pair of photons. The normalization parameters N_{bkg} and N_{sig} are free for each mass point. The Crystal Ball shape, which describes the signal peak, is a Gaussian combined with a low-side power law tail distribution,

$$C(m; m_0, \sigma, \alpha, n) = \frac{1}{N} \cdot \begin{cases} \exp\left(-(m-m_0)^2/(2\sigma^2)\right), & \text{if } m \geq m_0 - \alpha\sigma \\ \dfrac{(n/\alpha)^n \exp(-\alpha^2/2)}{((m_0 - m)/\sigma + n/\alpha - \alpha)^n}, & \text{if } m < m_0 - \alpha\sigma, \end{cases} \tag{5.11}$$

where m_0, α, σ, n, are fit parameters. The Crystal Ball normalization in Eq. 5.11, N, is absorbed into the signal normalization N_{sig} in Eq. 5.10. The Gaussian part is determined by the center of the reconstructed mass peak m_0, and the peak width σ. The variable α determines the switching

Table 5.6: Signal MC fit for α and n parameters.

mass	α	$\Delta\alpha$	n	Δn
200	1.21	0.08	3.50	0.75
250	1.22	0.08	3.13	0.89
300	13.75	22.69	22.74	21.49
320	1.17	0.04	3.44	0.42
340	1.29	0.09	2.93	0.76
360	1.19	0.08	3.26	0.74
380	1.37	0.09	2.33	0.42
400	1.23	0.10	2.92	0.75
420	1.18	0.10	3.02	0.79

point between the Gaussian and power law tail in terms of σ. The variable n determines the shape of the power law, and N determines the normalization. An example fit at $m = 320$ GeV is shown in Fig. 5.27. In Fig. 5.27 the parameters shown in the legend (mass, width, a, n, A, and B) correspond directly with the variables in Eq. 5.10 and Eq. 5.11 (m_0, σ, α, n, a_1, and a_2). The "background" and "signal" parameters in Fig. 5.27 relate to the normalization parameters of background and signal shape (N_{bkg}, N_{sig}, and N). Table 5.7 shows the peak position and peak width from all fits to the MC simulation. All of the MC simulation invariant mass distributions can be found in Appendix B.

To test for a narrow resonance, a functional form of the invariant reconstructed mass peak (m_0) is needed for any value of invariant mass. The parameters of the signal resonance were found by plotting the fit parameters as a function of mass and finding an appropriate function for each parameter as the signal mass increased. As expected, the parameters m_0 and σ were found to be linear with mass. Figs. 5.25 and 5.26 show the relation of σ and m_0 parameters to the generated mass point (m). From the small variations in n and α with respect to the generated signal mass (Table 5.6), the values were fixed at $\alpha = 1.2$ and $n = 3.25$ for fitting to data to improve fit convergence.

5.5 Data fitting

The pairwise invariant mass from the two loose and one reco-photon data is scanned in steps of 5 GeV from 220-600 GeV fitting a background with two variables plus a Crystal Ball function (Eq. 5.11) with fixed shape (but variable normalization) for signal at each point. A 5 GeV step is

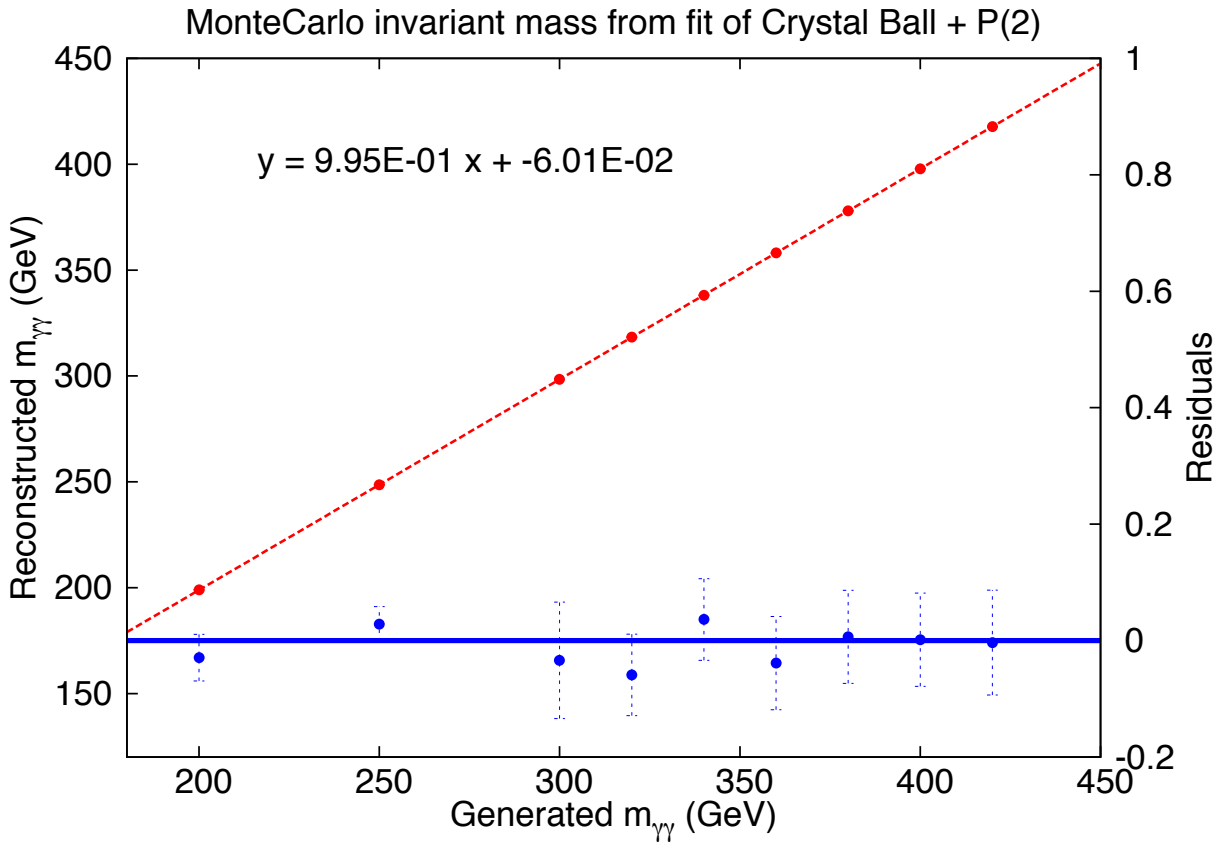

Figure 5.25: The results of the mass parameter from the fit to the Monte Carlo signal simulation versus the generated mass value. The data (red points) were fit with a straight line (red line). The blue points show the residuals between the fit and the data.

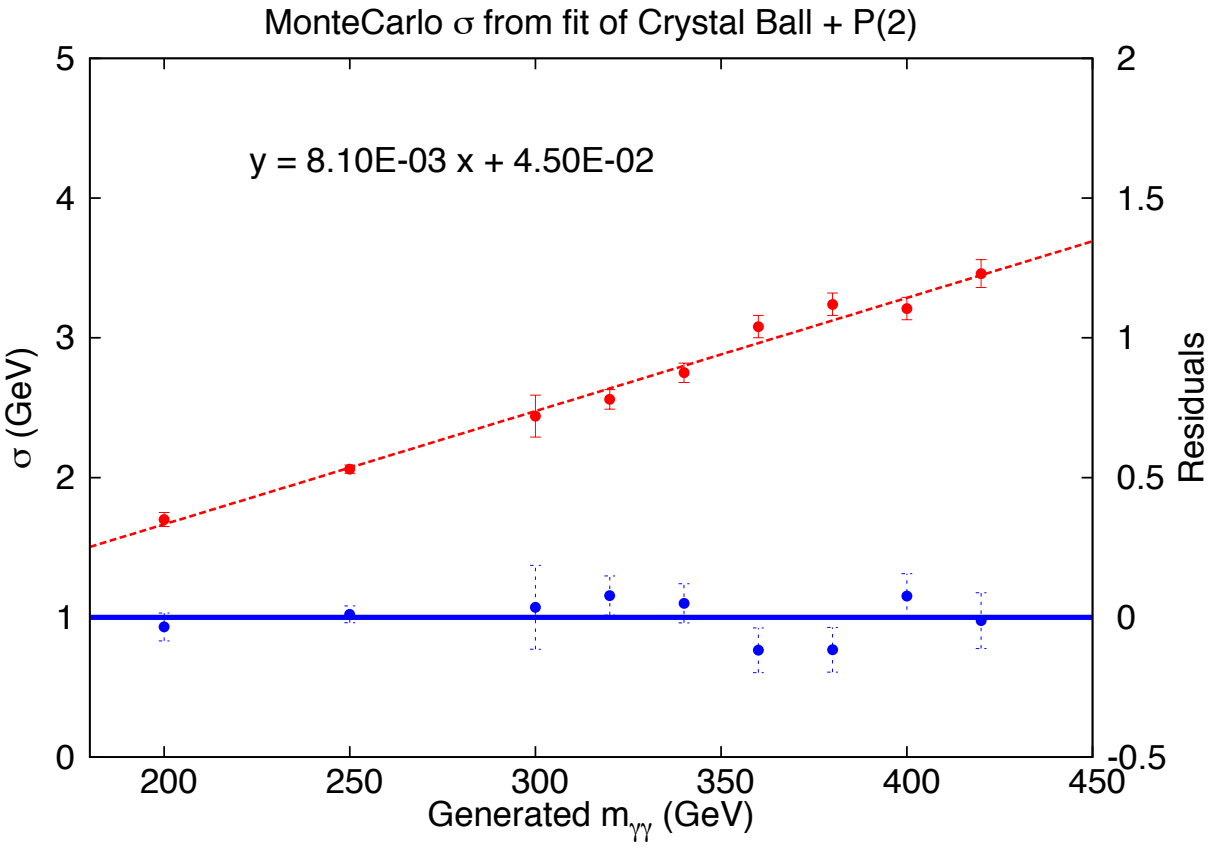

Figure 5.26: The results of the width parameter from the fit to the Monte Carlo signal simulation versus the generated mass value. The data (red points) were fit with a straight line (red line). The blue points show the residuals between the fit and the data.

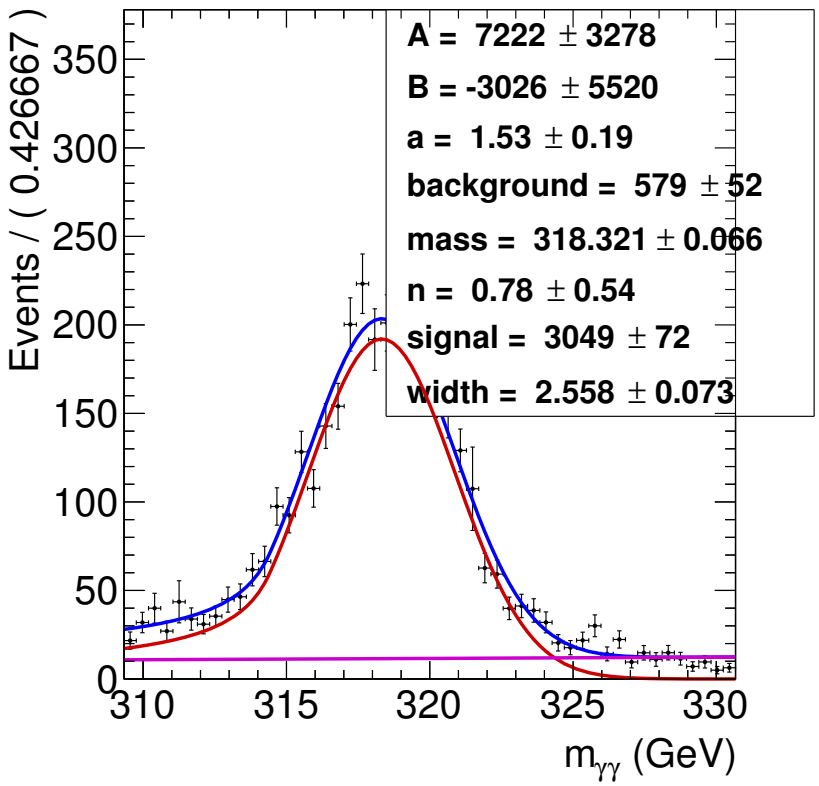

Figure 5.27: Fitting Monte Carlo signal simulation with a Crystal Ball plus polynomial.

Table 5.7: Results of the fit to the diphoton invariant mass for each signal MC sample.

Mass (GeV)	Peak position (GeV)	Peak width (GeV)
200	198.9	2.3
225	223.7	2.4
250	248.6	2.6
275	273.1	3.3
300	298.1	3.5
320	318.0	3.6
340	338.2	3.3
360	358.0	3.5
380	377.9	3.6
400	397.8	3.9
420	417.7	3.9
450	447.3	4.2
500	496.4	4.7
600	595.7	5.0

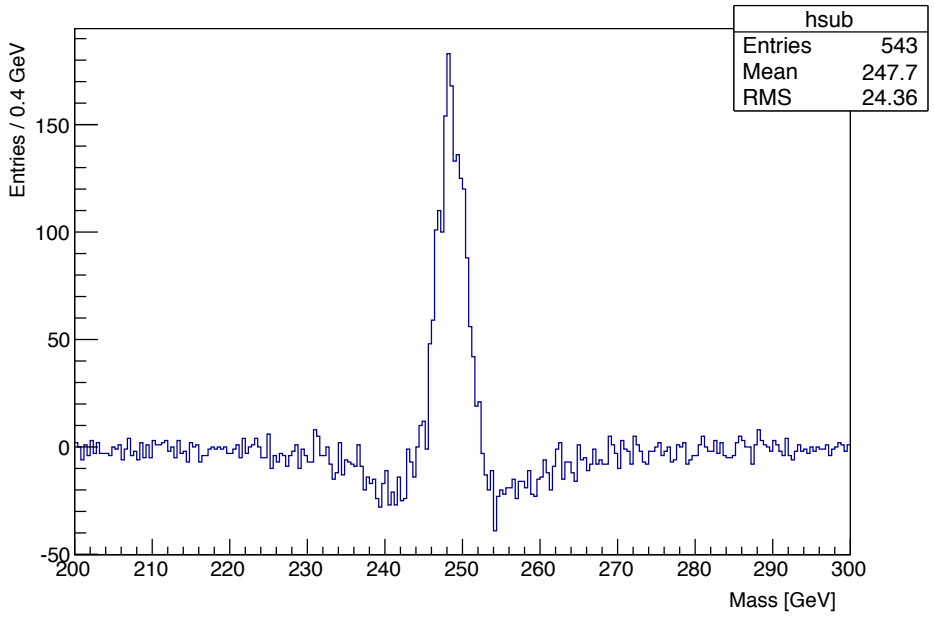

Figure 5.28: Distribution of the difference in the pairwise two photon invariant mass between the nominal reconstruction and one using a randomly chosen vertex as the primary vertex. The resulting distribution shows the generated peak at m=250 GeV is broadened by several GeV.

selected to ensure any narrow resonance is not overlooked but a much lower step is not required due to inherent resolution of the detector or inaccurate vertex identification. An overestimate of the effect of the vertex selection on the pairwise two photon invariant mass distribution for $m_{\tilde{\pi}} = 250\,\text{GeV}$ is shown in Fig. 5.28 by selecting a random vertex as the primary vertex for each event shows a broadening of the peak by several GeV.

The shape of the background is fit with the following functional form from $m = 180.0$ GeV to $m = 700.0$ GeV:

$$F_{bkg}(m) = \exp\left(\frac{C_1 m}{8000} + \frac{C_2 m^2}{8000}\right). \tag{5.12}$$

The function is fit using an unbinned maximum likelihood fit with the parameter C_1 limits set to $[-300, 0]$ and the parameter C_2 limits set to $[-6, 6]$. The function of Eq. 5.12 has better convergence than other possible background functions tested. Alternative backgrounds tested include a second-order polynomial and a power law ratio.

The background function, Eq. 5.12 (F_{bkg}), is added to a luminosity scaled signal shape, Eq. 5.11 (F_{sig}), to form the probability distribution function (PDF) $F_{SB}(m)$ in Eq. 5.13. The background normalization (B_{norm}), signal normalization (S_{norm}), and F_{bkg} coefficients are fit parameters while

Table 5.8: Initialization of parameters from Eq. 5.13.

Parameter	fixed value or (init., min., max.)
C_1	$(0.8, -300, 0)$
C_2	$(0.8, -6, 6)$
p_0	0.789
p_1	-0.000262
p_2	4.39×10^{-7}
α	1.2
n	3.25
B_{norm}	$(60.0, 50.0, 10^6)$
S_{norm}	$(0.1, 10^{-25}, 10^6)$

other variables are set based on the shape of MC signal simulation. Table 5.13 shows the initialization of the parameters of the $F_{SB}(m)$ probability distribution function. The data is fit to $F_{SB}(m)$ using standard profile likelihood tools available in RooStats [65].

$$F_{SB}(m) = B_{norm} \cdot F_{bkg}(m; C_1, C_2) + S_{norm} \cdot (\mathcal{L} \cdot \epsilon(m; p_0, p_1, p_2))^{-1} \cdot F_{sig}(m; m_0, \sigma, \alpha, n) \quad (5.13)$$

The scan over the invariant mass range $200 - 600\,\text{GeV}$ using the background plus signal hypothesis showed no significant signal excess. The region near $m_{\gamma\gamma} = 385\,\text{GeV}$ showed the largest excess from a smooth background in the 5 GeV step mass scan. Figure 5.29) shows the fit to data of a hyperpion mass of 385 GeV with an excess slightly above 2σ.

Limits on cross section times branching ratio are calculated using a profile likelihood calculator with signal events modeled from Monte Carlo simulation [66, 67]. The acceptance $\times$ efficiency function given by Table 5.5 is used in the limit interpretation, but the $\tilde{\rho}$ and $\tilde{\pi}$ branching fractions are not included. The invariant mass is fit using standard statistical tools available through the RooStats package in ROOT [65, 68].

The experimental limit on cross section times branching fraction as a function of the pairwise two photon mass for a three photon final state is shown in Fig. 5.30. The one and two σ bands are shown calculated with approximately 100 toy models at each mass point, and a table of these values are in Appendix A. The largest deviation from the background only hypothesis in Fig. 5.30 is near $m_{\gamma\gamma} = 385\,\text{GeV}$, that constitutes a 2σ deviation from the expected limit. Given the size of the search region, 2σ is not an unexpected excess.

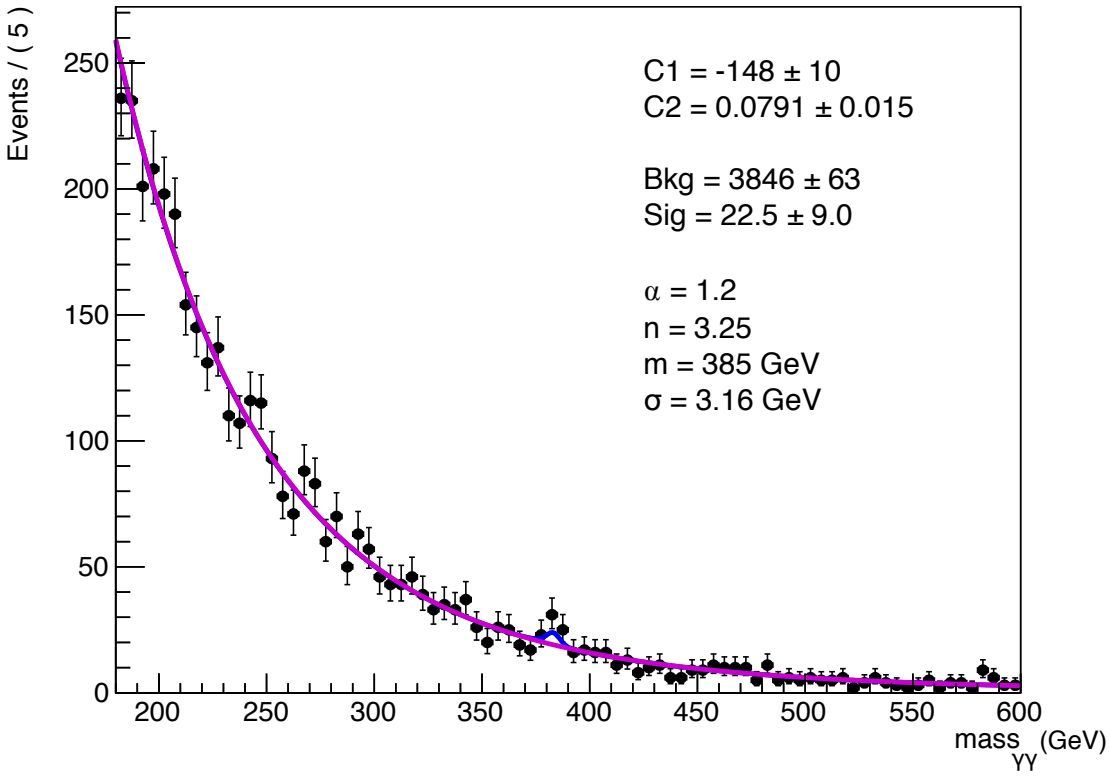

Figure 5.29: Three photon candidate pairwise invariant mass with signal and background fit. The fit is a second order polynomial background (magenta) with Crystal Ball function with $m = 385\,\text{GeV}$ (blue).

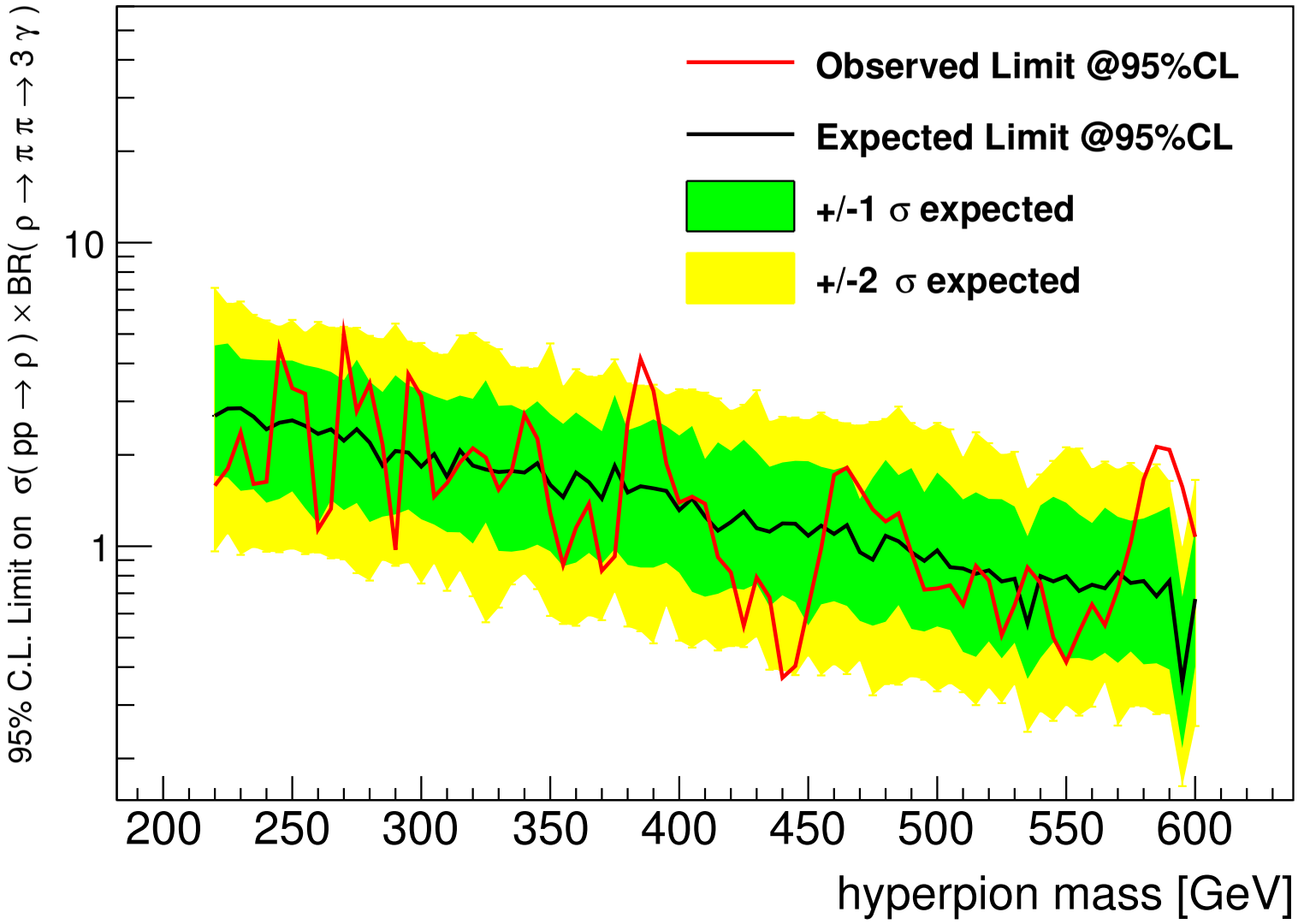

Figure 5.30: Expected and observed limit of pairwise invariant mass. 100 toy simulations were computed for mass points every five GeV in the range of 220-600 GeV. a table of these values are in Appendix A.

CHAPTER 6

CONCLUSION

A search is completed for a narrow resonance in the diphoton spectrum using CMS data by fitting the data to a smooth background function plus a narrow resonance in 12.3 fb^{-1} of data using proton-proton collisions at the CMS detector with center-of-mass energy of 8 TeV. The final data selection requires events that have either three loose photons or two loose photons plus an additional reco-photon.

The signal shape is determined with events simulated using the Monte Carlo technique through the Madgraph software based on a vectorlike confinement model that yields a three photon final state. Simulated events with hyperpion masses between 200-600 GeV are processed with CMSSW software modeling the interaction of particles with the detector. The acceptance $\times$ efficiency is modeled with a quadratic function determined from simulated signal events. The final diphoton invariant mass spectrum is modeled with a background that has an exponential function with a quadratic exponent (Eq. 5.12), and the signal was modeled with a Crystal Ball function (Eq. 5.11).

Different selection criteria and fitting functions were investigated. No significant narrow resonance in the diphoton spectrum is observed in the final sample for the mass range of $220 - 600$ GeV. The profile likelihood ratio is used as a test statistic to construct a likelihood interval. The 95% confidence level limits on the cross section times branching ratio are found that constrain the mass of the hyperpion (See Fig. 5.30 and Appendix A).

6.1 Future work

With the second run of the LHC already in progress, subsequent investigations similar to this analysis are expected. The hyperrho mass in this analysis is 1 TeV however it would be beneficial to simulate the full effects of allowing different values. Systematic uncertainty studies should be conducted to account for uncertainty in luminosity, energy resolution, photon identification efficiency, trigger efficiency, vertex identification, background shape, and signal shape. The analysis

would benefit from using the remainder of the 2012 data. The 2015 data with center-of-mass energy of 13 TeV with higher luminosity could explore more restrictive HLT and selection requirements.

APPENDIX A

LIMIT TABLE

Table A.1: Table of the 95% C.L. limit values for the hyperpion mass from 220 GeV-600 GeV. The graphical version is in the main text as Fig. 5.30.

mass	observed	expected	2σ low	1σ low	1σ high	2σ high
GeV	GeV	GeV	GeV	GeV	GeV	GeV
220	1.58318	2.68892	0.962118	1.70851	4.58632	7.09485
225	1.80432	2.84066	1.1022	1.68399	4.654	6.29098
230	2.3726	2.84893	0.936844	1.52287	4.15341	6.39781
235	1.60336	2.67207	0.99416	1.53993	4.11191	5.78345
240	1.63024	2.42751	0.959345	1.39146	4.09351	5.54275
245	4.50362	2.55173	0.955768	1.43211	4.0893	5.29189
250	3.31451	2.59702	0.982331	1.51645	4.08809	5.56562
255	3.17921	2.49269	0.942123	1.33447	3.94752	5.05975
260	1.13662	2.34407	0.953724	1.18666	3.86856	5.47882
265	1.32889	2.42783	0.912604	1.42282	3.75279	5.24894
270	5.00817	2.22687	0.905765	1.31539	3.52331	5.28218
275	2.78709	2.42898	0.815528	1.38899	4.11593	5.24213
280	3.43744	2.19566	0.770977	1.20217	3.48641	4.92948
285	2.16206	1.84311	0.901683	1.25226	3.22113	4.81034
290	0.973176	2.05953	0.862247	1.27338	3.65776	5.41029
295	3.68463	2.03498	0.885338	1.3219	3.3824	4.71945
300	3.12292	1.82928	0.754007	1.22713	3.26387	4.67135
305	1.45572	2.01086	0.878448	1.17914	3.12264	4.32586
310	1.61529	1.69045	0.713396	1.11356	3.01994	4.27873
315	1.88685	2.06904	0.833255	1.11125	3.13459	4.95077
320	2.10249	1.84423	0.684362	1.02106	3.05996	5.03915
325	1.96056	1.78993	0.561867	1.19775	3.52052	4.68906
330	1.53661	1.75578	0.627867	0.965456	2.89982	4.45674
335	1.76608	1.77001	0.748872	0.959902	2.91658	3.89465
340	2.71433	1.74907	0.81206	0.972816	2.78628	3.87576
345	2.26179	1.87723	0.722715	1.0123	3.00203	3.85554
350	1.28704	1.59381	0.589574	0.962376	2.72652	4.65538
355	0.867136	1.45109	0.554853	0.860058	2.52931	3.36353
360	1.15181	1.7484	0.547246	0.884096	2.75766	3.82931
365	1.3808	1.6251	0.591863	0.950731	2.57021	3.62118
370	0.830646	1.43412	0.570803	0.876958	2.39361	3.6416
375	0.925856	1.83911	0.707646	0.979694	3.15009	4.12588

Table A.1: Table of the 95% C.L. limit values for the hyperpion mass from 220 GeV-600 GeV. The graphical version is in the main text as Fig. 5.30.

mass	observed	expected	2σ low	1σ low	1σ high	2σ high
GeV	GeV	GeV	GeV	GeV	GeV	GeV
380	2.55791	1.50347	0.544111	0.868518	2.4103	3.4374
385	4.13919	1.57593	0.525103	0.851158	2.49495	3.38226
390	3.24971	1.55114	0.478816	0.850913	2.61798	3.40421
395	1.87047	1.52156	0.637944	0.883552	2.48333	3.14467
400	1.3933	1.31467	0.488938	0.81848	2.31562	3.29068
405	1.45645	1.43628	0.464026	0.707857	2.48992	3.28498
410	1.38067	1.25248	0.496189	0.682338	1.93787	3.20532
415	0.919987	1.12606	0.453824	0.697528	2.1989	3.06806
420	0.820315	1.20087	0.469164	0.728778	2.06151	2.79752
425	0.547131	1.29974	0.465513	0.719723	2.24117	2.92381
430	0.790181	1.1471	0.503853	0.752244	2.04065	3.26559
435	0.678858	1.11704	0.39211	0.634222	1.82728	2.57312
440	0.368841	1.18878	0.391329	0.689718	1.88777	2.66753
445	0.403229	1.18622	0.37635	0.653688	1.91153	2.65519
450	0.630761	1.08325	0.436255	0.548905	1.90579	2.60405
455	0.981985	1.16891	0.375428	0.643612	1.8267	2.75564
460	1.71657	1.09774	0.408474	0.659215	1.78416	2.60403
465	1.81516	1.17334	0.379314	0.636141	1.83595	2.54173
470	1.55445	0.956002	0.42068	0.567835	1.43031	2.49899
475	1.32218	0.903511	0.322951	0.54764	1.6812	2.56612
480	1.20689	1.08231	0.351613	0.564303	1.92477	2.6245
485	1.28352	1.03831	0.350093	0.640241	1.71596	2.88315
490	0.951107	0.956016	0.372909	0.534352	1.80891	2.54642
495	0.719413	0.895093	0.36342	0.524028	1.50616	2.40579
500	0.726483	0.968994	0.332772	0.544511	1.74826	2.54789
505	0.743775	0.853022	0.353951	0.529565	1.59386	2.42658
510	0.641144	0.844693	0.330563	0.448889	1.42608	1.96349
515	0.861787	0.811777	0.299712	0.432324	1.50527	2.37277
520	0.770928	0.833244	0.342835	0.486091	1.43187	2.18483
525	0.509188	0.765791	0.304292	0.427618	1.42844	2.00014
530	0.640323	0.781488	0.351012	0.481311	1.35126	2.04684
535	0.851523	0.555621	0.244819	0.365659	1.07851	1.54403
540	0.757203	0.797749	0.285991	0.428245	1.36344	1.72277
545	0.500176	0.76622	0.266068	0.483045	1.45545	1.91034
550	0.415447	0.796634	0.299881	0.427389	1.39085	2.11817
555	0.522153	0.712552	0.276856	0.428469	1.2735	2.09891
560	0.642756	0.746764	0.296223	0.419713	1.19277	1.79656
565	0.549419	0.727113	0.35729	0.445807	1.3395	1.90097
570	0.720511	0.820816	0.25669	0.413047	1.25026	1.79043

Table A.1: Table of the 95% C.L. limit values for the hyperpion mass from 220 GeV-600 GeV. The graphical version is in the main text as Fig. 5.30.

mass	observed	expected	2σ low	1σ low	1σ high	2σ high
GeV	GeV	GeV	GeV	GeV	GeV	GeV
575	1.02826	0.756929	0.296725	0.450307	1.21412	1.88085
580	1.65961	0.768322	0.29727	0.408592	1.2344	1.73499
585	2.12624	0.684654	0.280005	0.41175	1.28698	1.86102
590	2.07913	0.768771	0.281474	0.392636	1.34942	1.64164
595	1.56901	0.35628	0.162122	0.216324	0.681389	0.992287
600	1.07385	0.67039	0.255861	0.401762	1.13469	1.65391

APPENDIX B

MC FITTING

The following figures show the results of MC fitting of pairwise invariant mass of reconstructed photons for signal samples normalized to 10,000 generated events as described in Section 5.4.

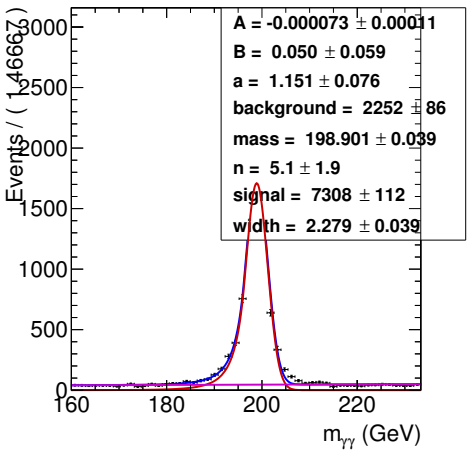

(a) 200 GeV

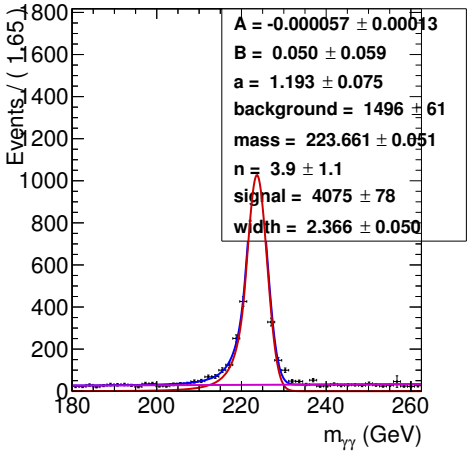

(b) 225 GeV

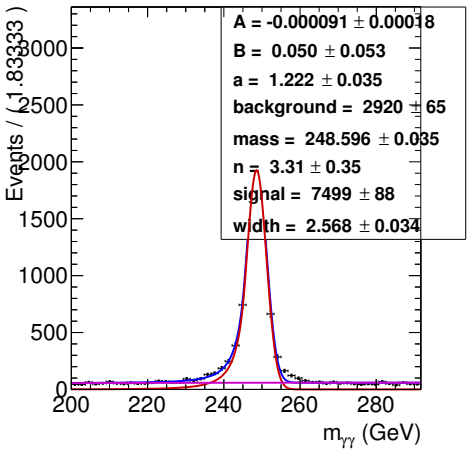

(c) 250 GeV

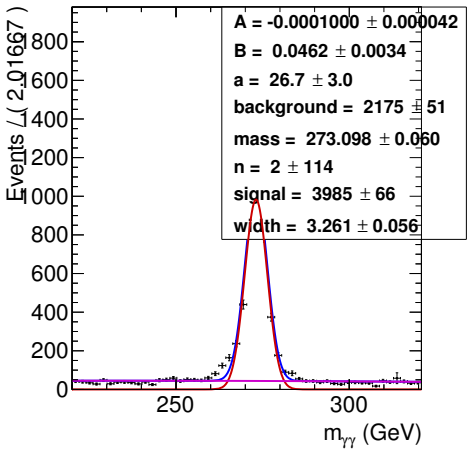

(d) 275 GeV

Figure B.1: Fitting to invariant mass distributions from 200 - 275 GeV.

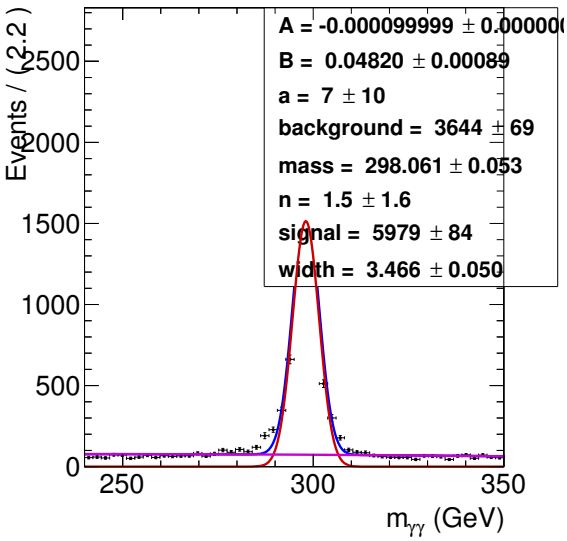

(a) 300 GeV

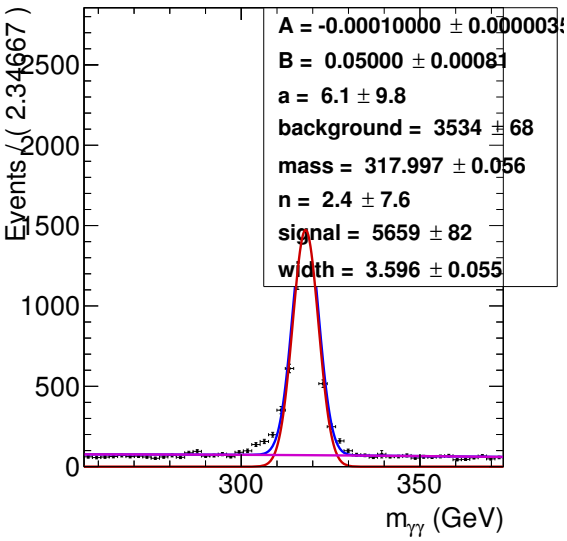

(b) 320 GeV

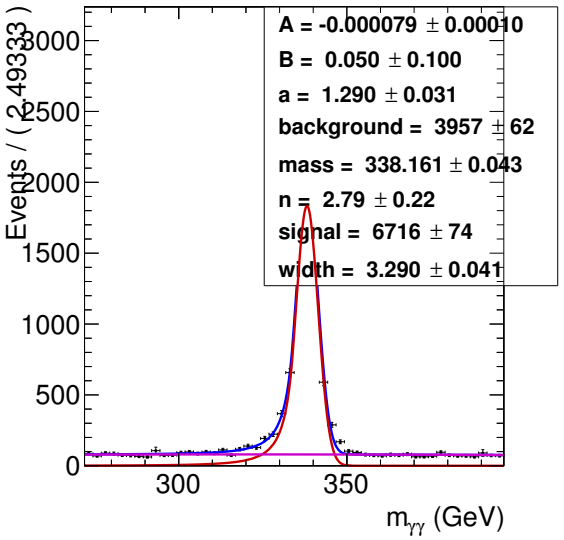

(c) 340 GeV

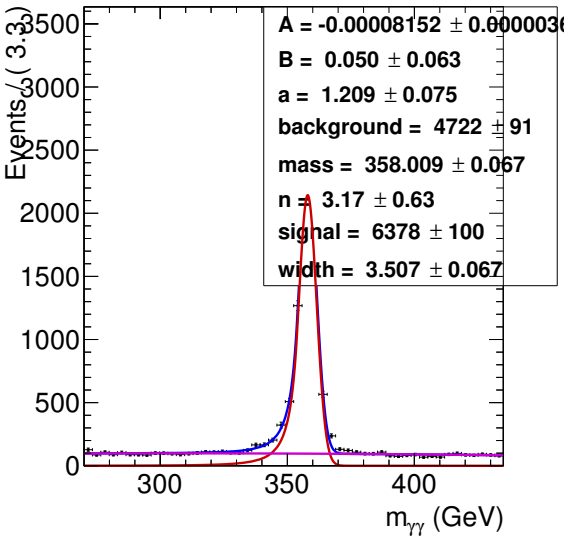

(d) 360 GeV

Figure B.2: Fitting to invariant mass distributions from 300 - 360 GeV.

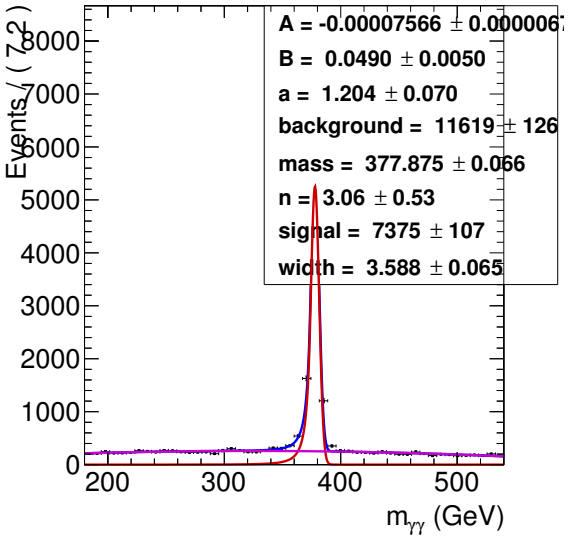

(a) 380 GeV

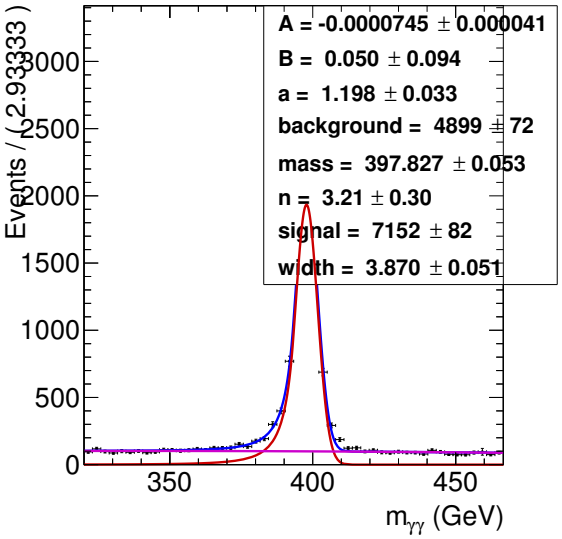

(b) 400 GeV

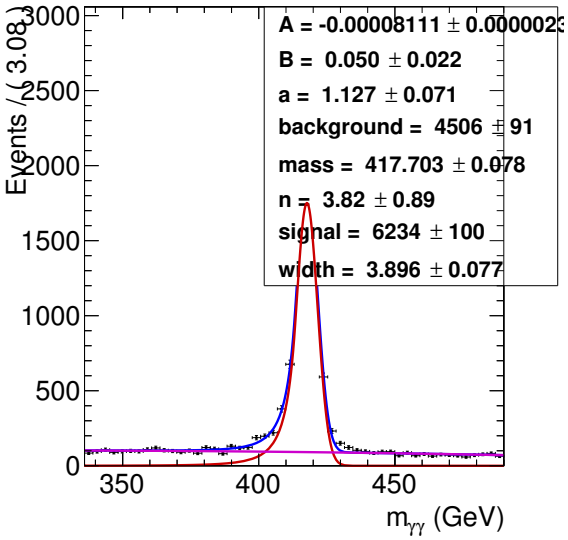

(c) 420 GeV

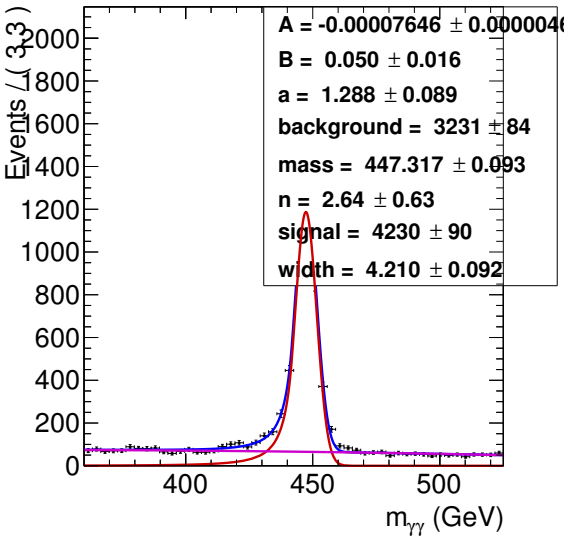

(d) 450 GeV

Figure B.3: Fitting to invariant mass distributions from 380 - 450 GeV.

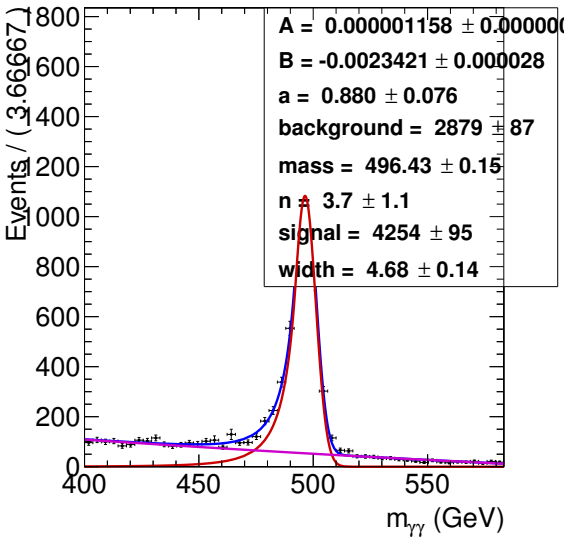

(a) 500 GeV

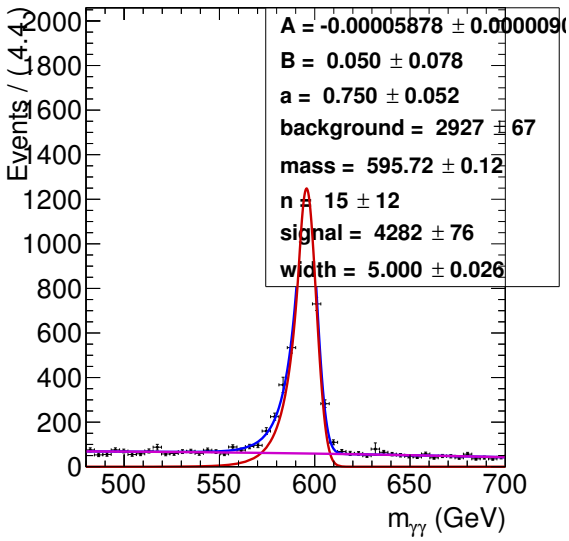

(b) 600 GeV

Figure B.4: Fitting to invariant mass distributions from 500 - 600 GeV.

BIBLIOGRAPHY

[1] Can Kilic, Takemichi Okui, and Raman Sundrum. Vectorlike Confinement at the LHC. *JHEP*, 1002:018, 2010. arXiv:0906.0577, doi:10.1007/JHEP02(2010)018.

[2] A. Zee. Quantum field theory in a nutshell. 2003.

[3] Alessandro Bettini. Introduction to elementary particle physics. 2008.

[4] S.L. Glashow. Partial Symmetries of Weak Interactions. *Nucl.Phys.*, 22:579–588, 1961. doi:10.1016/0029-5582(61)90469-2.

[5] Abdus Salam. Weak and Electromagnetic Interactions. *Conf.Proc.*, C680519:367–377, 1968.

[6] Steven Weinberg. A Model of Leptons. *Phys.Rev.Lett.*, 19:1264–1266, 1967. doi:10.1103/PhysRevLett.19.1264.

[7] G. Zweig. An SU(3) model for strong interaction symmetry and its breaking. Version 1. 1964.

[8] G. Zweig. An SU(3) model for strong interaction symmetry and its breaking. Version 2. pages 22–101, 1964.

[9] Murray Gell-Mann. A Schematic Model of Baryons and Mesons. *Phys.Lett.*, 8:214–215, 1964. doi:10.1016/S0031-9163(64)92001-3.

[10] Donald Perkins. *Introduction to High Energy Physics*. Cambridge University Press, Cambridge, UK, 4th edition, 2000.

[11] Francis Halzen and Alan Martin. *Quarks and Leptons: An Introductory Course in Modern Particle Physics*. Wiley, Hoboken, USA, 1st edition, 1984.

[12] David Griffiths. *Introduction to Elementary Particles*. Wiley, Hoboken, USA, 2nd edition, 2008.

[13] Serguei Chatrchyan et al. Observation of a new boson at a mass of 125 GeV with the CMS experiment at the LHC. *Phys. Lett.*, B716:30–61, 2012. arXiv:1207.7235, doi:10.1016/j.physletb.2012.08.021.

[14] Stephen P. Martin. A Supersymmetry primer. 1997. arXiv:hep-ph/9709356.

[15] Standard model of elementary particles [online]. 2014. URL: http://commons.wikimedia.org/wiki/File:Standard_Model_of_Elementary_Particles.svg [cited 09/20/14].

[16] Serguei Chatrchyan et al. Search for the standard model Higgs boson decaying into two photons in pp collisions at $\sqrt{s} = 7$ TeV. *Phys.Lett.*, B710:403–425, 2012. arXiv:1202.1487, doi:10.1016/j.physletb.2012.03.003.

[17] Serguei Chatrchyan et al. A New Boson with a Mass of 125 GeV Observed with the CMS Experiment at the Large Hadron Collider. *Science*, 338:1569–1575, 2012. doi:10.1126/science.1230816.

[18] Vardan Khachatryan et al. Observation of the diphoton decay of the Higgs boson and measurement of its properties. *Eur.Phys.J.*, C74(10):3076, 2014. arXiv:1407.0558, doi:10.1140/epjc/s10052-014-3076-z.

[19] Georges Aad et al. Combined Measurement of the Higgs Boson Mass in pp Collisions at $\sqrt{s} = 7$ and 8 TeV with the ATLAS and CMS Experiments. *Phys.Rev.Lett.*, 114:191803, 2015. arXiv:1503.07589, doi:10.1103/PhysRevLett.114.191803.

[20] Gregorio Bernardi and Matthew Herndon. Standard model Higgs boson searches through the 125 GeV boson discovery. *Rev.Mod.Phys.*, 86(2):479, 2014. arXiv:1210.0021, doi:10.1103/RevModPhys.86.479.

[21] Serguei Chatrchyan et al. Search for a standard-model-like Higgs boson with a mass in the range 145 to 1000 GeV at the LHC. *Eur.Phys.J.*, C73:2469, 2013. arXiv:1304.0213, doi:10.1140/epjc/s10052-013-2469-8.

[22] G.L. Bayatian et al. CMS technical design report, volume II: Physics performance. *J. Phys.*, G34:995–1579, 2007. doi:10.1088/0954-3899/34/6/S01.

[23] Georges Aad et al. Observation of a new particle in the search for the Standard Model Higgs boson with the ATLAS detector at the LHC. *Phys. Lett.*, B716:1–29, 2012. arXiv:1207.7214, doi:10.1016/j.physletb.2012.08.020.

[24] Serguei Chatrchyan et al. Search for top squark and higgsino production using diphoton Higgs boson decays. *Phys.Rev.Lett.*, 112:161802, 2014. arXiv:1312.3310, doi:10.1103/PhysRevLett.112.161802.

[25] Serguei Chatrchyan et al. Search for Large Extra Dimensions in the Diphoton Final State at the Large Hadron Collider. *JHEP*, 1105:085, 2011. arXiv:1103.4279, doi:10.1007/JHEP05(2011)085.

[26] Serguei Chatrchyan et al. Search for signatures of extra dimensions in the diphoton mass spectrum at the Large Hadron Collider. *Phys.Rev.Lett.*, 108:111801, 2012. arXiv:1112.0688, doi:10.1103/PhysRevLett.108.111801.

[27] Duong Nguyen. Search for Supersymmetry with Photon at CMS. 2011. arXiv:1110.2552.

[28] CMS Collaboration. Measurement of the differential isolated diphoton production cross section in pp collisions at sqrt(s) = 7 tev with the cms detector. Technical Report CMS-PAS-SMP-13-001, CERN, Geneva, 2013.

[29] CMS Collaboration. Search for multi-charged Heavy Stable Charged Particles. 2012.

[30] Serguei Chatrchyan et al. Search for heavy long-lived charged particles in *pp* collisions at $\sqrt{s} = 7$ TeV. *Phys. Lett.*, B713:408–433, 2012. arXiv:1205.0272, doi:10.1016/j.physletb.2012.06.023.

[31] Serguei Chatrchyan et al. Searches for long-lived charged particles in pp collisions at $\sqrt{s}$=7 and 8 TeV. *JHEP*, 1307:122, 2013. arXiv:1305.0491, doi:10.1007/JHEP07(2013)122.

[32] Serguei Chatrchyan et al. Search for Resonances in the Dilepton Mass Distribution in *pp* Collisions at $\sqrt{(s)} = 7$ TeV. *JHEP*, 1105:093, 2011. arXiv:1103.0981, doi:10.1007/JHEP05(2011)093.

[33] Serguei Chatrchyan et al. Search for Resonances in the Dijet Mass Spectrum from 7 TeV pp Collisions at CMS. *Phys. Lett.*, B704:123–142, 2011. arXiv:1107.4771, doi:10.1016/j.physletb.2011.09.015.

[34] Lyndon Evans and Philip Bryant. LHC Machine. *JINST*, 3:S08001, 2008. doi:10.1088/1748-0221/3/08/S08001.

[35] Fabienne Marcastel. CERN's Accelerator Complex. La chaîne des accélérateurs du CERN. Oct 2013. General Photo. URL: https://cds.cern.ch/record/1621583.

[36] G.L. Bayatian et al. CMS physics: Technical design report. 2006.

[37] CMS Collaboration. CMS Luminosity Based on Pixel Cluster Counting - Summer 2013 Update. 2013.

[38] Valeriane Duvivier. Cross section of LHC dipole.. Dipole LHC: Coupe transversale. AC Collection. Legacy of AC. Pictures from 1992 to 2002., 2001. URL: http://cds.cern.ch/record/843195.

[39] Measurement of CMS Luminosity. 2010.

[40] S. Chatrchyan et al. The CMS experiment at the CERN LHC. *JINST*, 3:S08004, 2008. doi:10.1088/1748-0221/3/08/S08004.

[41] Vardan Khachatryan et al. Performance of the CMS missing transverse momentum reconstruction in pp data at $\sqrt{s} = 8$ TeV. *JINST*, 10(02):P02006, 2015. arXiv:1411.0511, doi:10.1088/1748-0221/10/02/P02006.

[42] Serguei Chatrchyan et al. Performance of CMS muon reconstruction in *pp* collision events at $\sqrt{s} = 7$ TeV. *JINST*, 7:P10002, 2012. arXiv:1206.4071, doi:10.1088/1748-0221/7/10/P10002.

[43] Addendum to the CMS tracker TDR. 2000.

[44] Vardan Khachatryan et al. CMS Tracking Performance Results from early LHC Operation. *Eur. Phys. J.*, C70:1165–1192, 2010. arXiv:1007.1988, doi:10.1140/epjc/s10052-010-1491-3.

[45] CMS: The electromagnetic calorimeter. Technical design report. 1997.

[46] Serguei Chatrchyan et al. Energy calibration and resolution of the CMS electromagnetic calorimeter in pp collisions at $\sqrt{s} = 7$ TeV. *JINST*, 8:P09009, 2013. arXiv:1306.2016, doi:10.1088/1748-0221/8/09/P09009.

[47] David A. Petyt. Anomalous APD signals in the CMS Electromagnetic Calorimeter. *Nucl. Instrum. Meth.*, A695:293–295, 2012. doi:10.1016/j.nima.2011.10.025.

[48] Vardan Khachatryan et al. Performance of photon reconstruction and identification with the CMS detector in proton-proton collisions at $\sqrt{s} = 8$ TeV. 2015. arXiv:1502.02702.

[49] CMS: The hadron calorimeter technical design report. 1997.

[50] CMS, the Compact Muon Solenoid. Muon technical design report. 1997.

[51] S. Dasu et al. CMS. The TriDAS project. Technical design report, vol. 1: The trigger systems. 2000.

[52] Prerit Jaiswal, Karoline Kopp, and Takemichi Okui. Higgs Production Amidst the LHC Detector. *Phys. Rev.*, D87(11):115017, 2013. arXiv:1303.1181, doi:10.1103/PhysRevD.87.115017.

[53] Can Kilic and Takemichi Okui. The LHC Phenomenology of Vectorlike Confinement. *JHEP*, 1004:128, 2010. arXiv:1001.4526, doi:10.1007/JHEP04(2010)128.

[54] Neil D. Christensen and Claude Duhr. FeynRules - Feynman rules made easy. *Comput. Phys. Commun.*, 180:1614–1641, 2009. arXiv:0806.4194, doi:10.1016/j.cpc.2009.02.018.

[55] Johan Alwall, Michel Herquet, Fabio Maltoni, Olivier Mattelaer, and Tim Stelzer. MadGraph 5 : Going Beyond. *JHEP*, 1106:128, 2011. arXiv:1106.0522, doi:10.1007/JHEP06(2011)128.

[56] Torbjorn Sjostrand, Stephen Mrenna, and Peter Z. Skands. PYTHIA 6.4 Physics and Manual. *JHEP*, 0605:026, 2006. arXiv:hep-ph/0603175, doi:10.1088/1126-6708/2006/05/026.

[57] Gabriele Benelli, Balazs Bozsogi, Andreas Pfeiffer, Danilo Piparo, and Vidmantas Zemleris. Measuring CMS software performance in the first years of LHC collisions. *IEEE Nucl.Sci.Symp.Conf.Rec.*, 2011:108–112, 2011. doi:10.1109/NSSMIC.2011.6154461.

[58] CMS: The computing project. Technical design report. 2005.

[59] Emilio Meschi, T. Monteiro, Christopher Seez, and Pratibha Vikas. Electron Reconstruction in the CMS Electromagnetic Calorimeter. 2001.

[60] CMS Collaboration. Particle–flow event reconstruction in CMS and performance for jets, taus, and $E_{\mathrm{T}}^{\mathrm{miss}}$. CMS Physics Analysis Summary CMS-PAS-PFT-09-001, 2009. URL: http://cdsweb.cern.ch/record/1194487.

[61] CMS Collaboration. Commissioning of the particle-flow event reconstruction with the first LHC collisions recorded in the CMS detector. CMS Physics Analysis Summary CMS-PAS-PFT-10-001, 2010. URL: http://cdsweb.cern.ch/record/1247373.

[62] CMS Collaboration. Determination of the jet energy scale in CMS with pp collisions at $\sqrt{s} = 7$ TeV. CMS Physics Analysis Summary CMS-PAS-JME-10-010, 2010. URL: http://cdsweb.cern.ch/record/1308178.

[63] Matteo Cacciari, Gavin P. Salam, and Gregory Soyez. FastJet User Manual. *Eur.Phys.J.*, C72:1896, 2012. arXiv:1111.6097, doi:10.1140/epjc/s10052-012-1896-2.

[64] W. Adam, R. Fruhwirth, A. Strandlie, and T. Todorov. Reconstruction of electrons with the Gaussian sum filter in the CMS tracker at LHC. *eConf*, C0303241:TULT009, 2003. arXiv:physics/0306087, doi:10.1088/0954-3899/31/9/N01.

[65] Lorenzo Moneta, Kevin Belasco, Kyle S. Cranmer, S. Kreiss, Alfio Lazzaro, et al. The RooStats Project. *PoS*, ACAT2010:057, 2010. arXiv:1009.1003.

[66] A L Read. Presentation of search results: the cl s technique. *Journal of Physics G: Nuclear and Particle Physics*, 28(10):2693, 2002. URL: http://stacks.iop.org/0954-3899/28/i=10/a=313.

[67] G. J. Feldman and R. D. Cousins. Unified approach to the classical statistical analysis of small signals. Phys. Rev. D, 57:3873–3889, April 1998. arXiv:physics/9711021, doi:10.1103/PhysRevD.57.3873.

[68] I. Antcheva, M. Ballintijn, B. Bellenot, M. Biskup, R. Brun, et al. ROOT: A C++ framework for petabyte data storage, statistical analysis and visualization. *Comput. Phys. Commun.*, 180:2499–2512, 2009. doi:10.1016/j.cpc.2009.08.005.

BIOGRAPHICAL SKETCH

Brendan Diamond earned a B.S. in Physics from California State University Chico and an M.S. in Physics from Florida State University. He joined the FSU high energy physics group just before the Compact Muon Solenoid experiment at CERN became fully operational. He spent seven years as a docent with the Chico Community Observatory and has a passion for science education.

During his time in physics at FSU additional work/education completed include the following:

- investigations of a SO10 supersymmetry signal
- participated in the CMS Data Analysis School
- participated in the CTEQ - MCnet Summer School
- CMS service work in the ECAL Prompt Feedback Group
- CMS service work as ECAL shifter
- CMS service work as ECAL Detector Guru (DG)
- CMS service work as ECAL Detector Guru Lieutenant (DGL)
- explored photon misidentification rates with Anthony Barker
- identified inconsistent particle ID between PDG, CMSSW, and generators.